NORTHWESTERN UNIVERSITY

Multiscale Modeling of Failure in Granular Media: From Continuum Scales to Granular Scale

A DISSERTATION

SUBMITTED TO THE GRADUATE SCHOOL

IN PARTIAL FULFILLMENT OF THE REQUIREMENTS

for the degree

DOCTOR OF PHILOSOPHY

Field of Theoretical and Applied Mechanics

By

Qiushi Chen

EVANSTON, ILLINOIS

June 2011

ABSTRACT

Multiscale Modeling of Failure in Granular Media:

From Continuum Scales to Granular Scale

Qiushi Chen

Granular media, such as sand, are multiscale in nature. It is well known that the mechanical behavior of such materials is essentially encoded at the granular scale. Therefore, methods for upscaling information across relevant scales of interest – from granular scale ($\sim$ 1 mm) to field scale ($>$ 1 m) – are needed to attain a more accurate modeling and prediction of material behavior. In particular, multiscale analysis is important for conditions involving failure of granular materials, such as penetration, strain localization, or state transition, where the classical constitutive descriptions may no longer apply.

The main objective of this dissertation is to accurately model failure phenomena in granular media by providing enhanced and more accurate material descriptions through multiscale framework, where information at finer scales will be extracted and classical phenomenological constitutive models can by bypassed. Three studies are presented: footing/penetration caused soil failure, strain localization, and state transition from solid-like to fluid-like state.

In the first study, an internally consistent probabilistic model for material properties is developed at multiple scales. The probabilistic simulation approach is coupled with the finite element method, where finer scale is pursued only as necessary. The constitutive response at the coarse scale is provided by fine scale computations.

In the second study, strain localization problem is analyzed using a multiscale strong discontinuity approach, where evolutions of key material parameters will be obtained from granular scale computations or local measurements from physical experiments. The information is passed between scales through a hierarchical multiscale computational framework.

The last study presents an enhanced continuum scale constitutive model for dry dilative granular media, aiming to bridge solid-like and fluid-like state. The material strength is composed of a dilation part and a rate-dependent residual strength. The dilatancy strength plays a key role during solid-like behavior but vanishes in the fluid-like regime. The residual strength is postulated to evolve with strain rate.

The multiscale approaches proposed in this dissertation provide missing linkage between continuum scale material descriptions and the underlying fine scale information, which eventually lead to more accurate and realistic modeling of failure in granular media.

Acknowledgements

First and foremost, I would like to express my sincere thanks to my academic advisor, Professor José Andrade, for his guidance and support throughout my Ph.D. studies. I have learned a lot, much more than just academic wise, through my four years working with José. His insights into problems and passion in research and life will be an inspiration to me throughout my career.

I want to thank Professor Richard Finno and Professor John Rudnicki for serving on my Ph.D. committee. Both of them are great teachers and are willing to offer their generous help whenever I asked. I enjoyed their classes very much, though many times I had to get up really early during Chicago winters.

I also want to acknowledge all my colleagues and friends at Northwestern University, especially those in geotechnical engineering and geomechanics groups, with whom I shared office or went to classes, seminars and gyms together. They made the time spent in school much more rewarding and enjoyable.

I am also grateful for the financial supports I received from Walter P. Murphy fellowships from Northwestern University, Richter Funds Scholarship from Richter Foundation, grant number CMMI 0726908 from National Science Foundation and grant number FA9550-08-1-1092 from Air Force Office of Scientific Research, without which I would not have been able to complete this work.

Finally, and most importantly, I owe many thanks to my family: my wife Xiaowan, she gives up so many things for my graduate studies, and she is always supportive and patient with me; my lovely boy Siyuan, he brings many joys, and sometimes tears, to the family; my parents, they made me who I am and are always there to support me.

To Xiaowan and Siyuan

Table of Contents

List of Tables

List of Figures

CHAPTER 1

Introduction

1.1. Objective and statement of the problem

The main objective of this dissertation is to accurately model failure phenomena in granular media by providing enhanced and more accurate material descriptions through multiscale framework. The term 'multiscale' refers to the fact that the classical constitutive models used to describe material behavior at the continuum scales are enhanced by extracting information from finer scales, which can be continuum or granular scales. Figure 1.1 shows the relevant scales of interest for granular media and applicability of continuum description or discrete description to different scales in this dissertation. Within

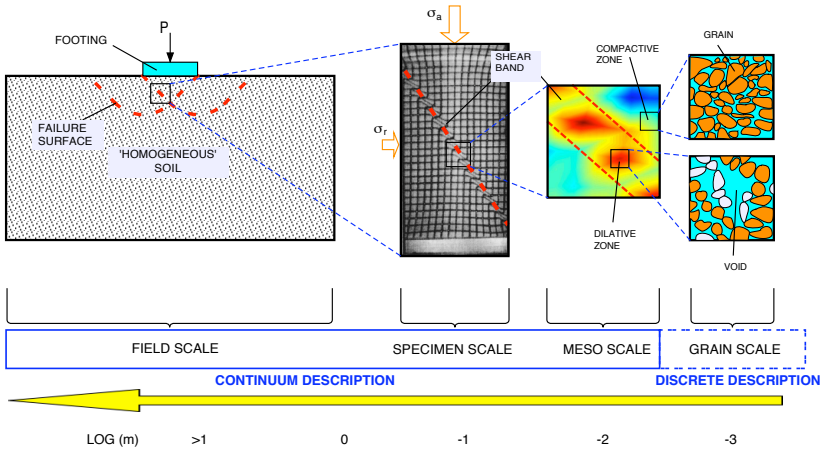

Figure 1.1. Relevant scales of interest for granular media: from field scale to granular scale, as well as applicability of continuum description and discrete description. Adopted from [1]

the context of this dissertation, the definition of failure not only includes the classical

localized failure, such as shear band, which usually leads to significant reduction of load-bearing capacity, but it also refers to state transition in granular media, i.e., transition from a solid-like state to fluid-like state, as seen in granular avalanches.

Given the complexity and diversity of the failure forms in granular media, in this dissertation we restrict our attention to some typical and representative problems. Three studies are presented focusing on: (1) a field scale footing failure problem, where the scale of interest is within the continuum regime; (2) a specimen scale strain localization problem, where continuum scale is linked to grain scale information; (3) a state transition problem, where the continuum scale model is enhanced to capture solid-like to fluid-like state transition in granular media.

Together, these three studies aim to answer two important questions: for granular media, what is the appropriate information to pass at a specific scale? how to enhance the constitutive model at continuum scales given the knowledge at finer scales? Numerical examples will illustrate how the performance of the enhanced models is improved compared to classical models.

1.2. Motivation

The term granular media embraces a wide variety of materials both in nature and in engineering applications. Examples of granular media include sand, sandstones, pharmaceutical pills, and so on. Because of the abundant appearance, understanding and modeling the failure phenomena in granular materials can be of great practical importance. For instance, the design of a foundation/footing resting on granular soils requires

the knowledge of the bearing capacity of the underlying media; handling of granular powder in pharmaceutical industries usually requires understanding the transition of granular media from stable solid-like state to fluid-like state.

One of the major challenges in modeling failure in granular media is the constitutive description. Classical approaches consider phenomenology, which means they formulate the observed phenomena directly in an appropriate but oftentimes sophisticated mathematical formalism. There is abundant work in the literature on phenomenological approach, for instance, [3, 4, 5, 6, 7, 8, 9], just to name a few. However, classical phenomenological constitutive laws face significant challenges in extreme conditions, such as localization or penetration, and these constitutive laws are not yet able to faithfully capture state transition in granular media. There are efforts in predicting onset of extreme conditions, such as localization, using bifurcation theory, e.g., [10, 11]. But the prediction of bifurcation is sensitive to the constitutive model used and it is not clear how material behaves after the onset of localization [12]. Therefore, new approaches beyond phenomenology are needed to accurately model failure phenomena in granular materials. To this end, it is important to recognize that granular materials are multiscale in nature (cf. Figure 1.1). The mechanical behavior of such materials is essentially encoded at the grain level and methods for upscaling such information across relevant scales of interest are needed for accurate material description.

1.3. Methodology

In this dissertation, we propose multiscale approaches where material descriptions at continuum scales are enhanced by information from finer scales. In particular, classical

elasto-plasticity models are used to describe material behavior at the continuum scales and are cast within non-linear finite element programs through computational plasticity procedures [13]. At the granular scale, discrete element method (DEM) [14] and high-fidelity local measurement data from physical experiments [15] are used as micromechanical model to provide material response.

Enhancements to constitutive response at the coarse scale are obtained through two different approaches. In the first approach, the coarse scale constitutive responses (stress response and constitutive tangent) are directly given by homogenized stresses and constitutive tangents from finer scales. A concurrent information passing scheme is implemented (following taxonomy by [16]), in which the coarse scale and fine scale are coupled directly and the coarse constitutive responses are obtained from fine scales 'on the fly'. This approach is utilized in the multiscale random field study in Chapter 3. In the second approach, the coarse scale and fine scale are not directly coupled. Instead, evolutions of key material parameters (e.g., plastic internal variables) are extracted from granular scale first, and then used as input into the coarse scale elasto-plastic models. This is termed as hierarchical approach by [16]. The second approach is applied in Chapters 5 and 6 (the strain localization problem). The stress integration scheme used in the hierarchical approach is based on the semi-implicit return mapping algorithm proposed in Chapter 4.

1.4. Structure of the Dissertation

This dissertation is organized in much the same chronological order as my research work at Northwestern University. It covers all relevant scales of granular media, from field scale all the way to granular scale. It starts from continuum descriptions of granular

media at the field and specimen scales (Chapter 3), and then links continuum descriptions with granular scale information (Chapters 4 and 5), and finally comes back to continuum descriptions (Chapter 6). Regarding the failure phenomena, the localized failure is studied in Chapters 3 and 5 and the state transition problem is studied in Chapter 6.

It should be noted that each of the main chapters (3, 4, 5 and 6) is a self-contained study and has been or will be published in technical journals. The outline for each chapter is listed as following:

Chapter 2 covers some fundamental research background that are important to the rest of the dissertation. In particular, the classical elasto-plastic framework, governing equations and finite element implementations with the presence of discontinuous kinematic fields are discussed.

Chapter 3 presents a study on continuum scale footing failure problem where the material properties are generated through internally-consistent probabilistic models developed at multiple scales. The probabilistic models are incorporated into a simulation framework where refinement of material description to finer scales is pursued only as necessary. Finite element method is coupled with the probabilistic simulation approach, where the constitutive response at coarse scales will be provided by finer scale computations. Numerical examples are presented to show how the performance of the footing is influenced by multiscale random fields.

Chapter 4 proposes a semi-implicit return mapping algorithm for plasticity models with nonsmooth evolution laws. The key idea is to 'freeze' the plastic internal variables at their previous state, followed by implicitly integrating stresses and plastic multiplier. Once convergence is achieved, the plastic internal variables will be updated. The algorithm is

able to handle nonsmooth evolution laws, which will be particularly useful in multiscale computations when nonsmooth constitutive relationships are extracted from underlying micromechanics. This algorithm is used as the backbone of the multiscale framework utilized in Chapters 5 and 6.

Chapter 5 presents a study on specimen scale localization problem. The discontinuities in the kinematic fields are accommodated through a finite element enhancement technique called the assumed enhanced strain (AES) method. The underlying granular scale information is extracted and used to enhance continuum scale constitutive descriptions for materials both inside and outside the localization band. Both granular scale computation and local measurement data from physical experiments are used to provide evolutions of key plastic internal variables, such as friction and dilatancy. Numerical examples are presented to show the applicability of the method.

Chapter 6 presents a rate-dependent plasticity model for dilative granular media aiming to capture the transition from solid-like to fluid-like state. In the model, the material strength is composed of a dilation part and a rate-dependent residual part. The dilation strength plays an important role in the solid-like state but vanishes in the fluid-like state. The proposed model is implemented into a finite difference program applied to granular flow problem, and results from the model are compared with granular particle simulations. Then, through the multiscale framework (as in Chapter 5), the proposed model is implemented into a finite element program to simulate a specimen scale localization problem. With the enhanced rate-dependent residual strength, it is shown that the model is able to accurately capture experiment results.

In conclusion, **Chapter 7** summarizes some key findings of this dissertation. Limitations for the current work are also discussed. And finally, possible future lines of research are outlined.

CHAPTER 2

Research background

Each of the following chapters, from Chapter 3 to Chapter 6, has in its introduction a detailed literature review on related research topics: Chapter 3 on random fields and multiscale analysis; Chapter 4 on integration algorithms and nonsmooth evolution laws; Chapter 5 on localization modeling and multiscale analysis; Chapter 6 on granular flow. It would be tedious and trivial to repeat those reviews in this chapter. Instead, this chapter will cover research background contents that are important to this dissertation, but not discussed in details in the following chapters. In particular, the general elastoplastic framework for continuum description of granular materials, governing equations and finite element implementations with the presence of strong discontinuities will be presented.

2.1. Elastoplastic framework for continuum description of granular materials

Elastoplasticity is perhaps the most widely utilized framework for describing material nonlinearities and inelastic behavior. Throughout this dissertation, elastoplasticity will be utilized for the continuum scale description of granular materials. In this section, the main ingredients of classical elastoplastic framework for infinitesimal deformations will be presented. Then, the Drucker-Prager plasticity model particular suitable for describing granular materials will be discussed.

2.1.1. Classical elastoplastic framework

Many materials, such as granular materials and metals, when loaded, typically exhibit elastic behavior up to a stress called the yield strength. Once loaded beyond the yield strength, materials develop plastic strains or irrecoverable deformations. The main ingredients of a framework describing such elasto-plastic behavior consist of the following:

- *Elastic domain and the yield function*

We first define a function $F : \mathbb{S} \times \mathbb{R}^{ndim}$, such that the admissible states $\{\boldsymbol{\sigma}, \boldsymbol{\alpha}\}$ are constrained to lie in the set $\mathbb{E}$ defined as

$$\mathbb{E} := \{(\boldsymbol{\sigma}, \boldsymbol{\alpha}) \in \mathbb{S} \times \mathbb{R}^{ndim} | F(\boldsymbol{\sigma}, \boldsymbol{\alpha}) \leq 0\} \tag{2.1}$$

where $\mathbb{S}$ is the space of symmetric second-order tensors and $\mathbb{R}^{ndim}$ is the set of real numbers in n-dimension. $\boldsymbol{\sigma}$ is the stress tensor and $\boldsymbol{\alpha}$ is the internal variables. The interior of $\mathbb{E}$, denoted by int($\mathbb{E}$), is given as the elastic domain

$$\text{int}(\mathbb{E}) := \{(\boldsymbol{\sigma}, \boldsymbol{\alpha}) \in \mathbb{S} \times \mathbb{R}^{ndim} | F(\boldsymbol{\sigma}, \boldsymbol{\alpha}) \leq 0\} \tag{2.2}$$

the boundary of $\mathbb{E}$, denoted by $\partial\mathbb{E}$, defines the yield surface

$$\partial\mathbb{E} := \{(\boldsymbol{\sigma}, \boldsymbol{\alpha}) \in \mathbb{S} \times \mathbb{R}^{ndim} | F(\boldsymbol{\sigma}, \boldsymbol{\alpha}) = 0\} \tag{2.3}$$

In classical elastoplasticity, only states $\{\boldsymbol{\sigma}, \boldsymbol{\alpha}\}$ within or on the boundary of $\mathbb{E}$ are considered to be admissible.

- *Additive decomposition of the strain tensor*

Within the regime of infinitesimal deformations, it can be assumed that the total strain rate tensor $\dot{\boldsymbol{\epsilon}}$ can be decomposed into an elastic part $\dot{\boldsymbol{\epsilon}}^e$, and a plastic part $\dot{\boldsymbol{\epsilon}}^p$ such that

$$\dot{\boldsymbol{\epsilon}} = \dot{\boldsymbol{\epsilon}}^e + \dot{\boldsymbol{\epsilon}}^p \tag{2.4}$$

It should be pointed out that $\dot{\boldsymbol{\epsilon}}$ can be viewed as an independent variable, and the plastic strain rate will be given by the flow rule shown later. Then, the above decomposition can be seen as a definition for the elastic strain rate tensors as

$$\dot{\boldsymbol{\epsilon}}^e = \dot{\boldsymbol{\epsilon}} - \dot{\boldsymbol{\epsilon}}^p \tag{2.5}$$

- *Generalized Hooke's law giving the stress response*

The stress rate tensor $\dot{\boldsymbol{\sigma}}$ is related to the elastic strain rate tensor through fourth-order elastic moduli $\boldsymbol{c}^e$

$$\dot{\boldsymbol{\sigma}} = \boldsymbol{c}^e : \dot{\boldsymbol{\epsilon}}^e \tag{2.6}$$

where, for isotropic linear elasticity, the elastic moduli tensor is given as

$$\boldsymbol{c}^e = K\mathbf{1} \otimes \mathbf{1} + 2\mu_s(\boldsymbol{I} - \frac{1}{3}\mathbf{1} \otimes \mathbf{1}) \tag{2.7}$$

where K and μ_s are the elastic bulk and shear modulus, respectively. $\mathbf{1}$ is the second-order identity tensor. $\boldsymbol{I}$ is the fourth-order symmetric identity tensor with components defined through second-order identity tensor as

$$I_{ijkl} = \frac{1}{2}(\delta_{ik}\delta_{jl} + \delta_{il}\delta_{jk}) \tag{2.8}$$

Alternatively, by substituting equations (2.5) into (2.6), making use of flow rule (2.11) and consistency condition (2.13), the stress rate tensor can also be related to the total strain rate tensor through

$$\dot{\boldsymbol{\sigma}} = \boldsymbol{c}^{ep} : \dot{\boldsymbol{\epsilon}} \tag{2.9}$$

$\boldsymbol{c}^{ep}$ is the fourth-order elasto-plastic moduli

$$\boldsymbol{c}^{ep} = \boldsymbol{c}^{e} - \frac{1}{\chi}\boldsymbol{c}^{e} : \boldsymbol{g} \otimes \boldsymbol{f} : \boldsymbol{c}^{e};\ \chi = H - \boldsymbol{g} : \boldsymbol{c}^{e} : \boldsymbol{f} \tag{2.10}$$

where $\boldsymbol{f} := \partial F/\partial \boldsymbol{\sigma}$, and $\boldsymbol{g} := \partial G/\partial \boldsymbol{\sigma}$, with F being the yield function and G being the plastic potential function. H is the hardening modulus defined in (2.15).

- *Flow rule and the Kuhn-Tucker conditions*

The flow rule governs the evolution of plastic strain tensor, via some plastic potential function $G(\boldsymbol{\sigma}, \boldsymbol{\alpha})$

$$\dot{\boldsymbol{\epsilon}}^{p} = \dot{\lambda}\boldsymbol{g},\ \boldsymbol{g} := \frac{\partial G(\boldsymbol{\sigma}, \boldsymbol{\alpha})}{\partial \boldsymbol{\sigma}} \tag{2.11}$$

where $\dot{\lambda} \geq 0$ is called the plastic multiplier or consistency parameter. For the case when $G = F$, the plastic strain rate will be normal to the yield surface F, the flow rule is said to be associative. The associative flow rule is commonly used in metal plasticity. However, in many other materials, such as granular materials, experimental evidence oftentimes suggests a non-associative flow rule, i.e., the plastic strain rate not normal to the yield surface. In this case, $G \neq F$.

Furthermore, the consistency parameter $\dot{\lambda} \geq 0$ is assumed to obey the Kuhn-Tucker optimality conditions

$$\dot{\lambda} \geq 0,\ F(\boldsymbol{\sigma}, \boldsymbol{\alpha}) \leq 0,\ \text{and},\ \dot{\lambda} F(\boldsymbol{\sigma}, \boldsymbol{\alpha}) = 0 \tag{2.12}$$

In addition to the Kuhn-Tucker conditions, $\dot{\lambda} \geq 0$ satisfies the consistency requirement

$$\dot{\lambda} \dot{F}(\boldsymbol{\sigma}, \boldsymbol{\alpha}) = 0 \tag{2.13}$$

- *Evolution laws for internal variables*

Evolution laws for internal variables $\boldsymbol{\alpha}$ are given as

$$\dot{\boldsymbol{\alpha}} = \dot{\lambda} \hat{\boldsymbol{\alpha}}(\boldsymbol{\sigma}, \boldsymbol{\alpha}) \tag{2.14}$$

The evolution of the yield surface due to the plastic flow takes the form

$$\frac{\partial F}{\partial \boldsymbol{\alpha}} \cdot \dot{\boldsymbol{\alpha}} = -\dot{\lambda} H \tag{2.15}$$

where H is called the hardening modulus. It should be pointed out that most evolution laws of internal variables are based on phenomenology, involving calibrating a large set of parameters. Oftentimes, the selection of parameters are quite arbitrary.

2.1.2. Drucker-Prager plasticity model for granular materials

For granular materials, frictional and dilatational effects are significant. The plastic behavior depends on pressure, and in general, obeys non-associative flow rule. Within the general elastoplastic framework, this subsection presents the Drucker-Prager (D-P) model

[4], which takes into account all these features and is widely used for describing behavior of dilate frictional materials. This model will be utilized to describe granular material behavior at the continuum scale, throughout this dissertation.

First, we define two stress invariants, pressure p and deviatoric stress invariant q as

$$p = \frac{1}{3}\mathrm{tr}\boldsymbol{\sigma};\ q = \sqrt{\frac{3}{2}}\|\boldsymbol{s}\| \tag{2.16}$$

with $\mathrm{tr}\,\square = \square : \boldsymbol{\delta}$ as the trace operator, $\boldsymbol{s} = \boldsymbol{\sigma} - p\boldsymbol{\delta}$ as the deviatoric component of the stress tensor. $||\square||$ denotes the L_2 norm of $\square$. Similarly, two invariants of the strain rate tensor are defined as

$$\dot{\epsilon}_v = \mathrm{tr}\,\dot{\boldsymbol{\epsilon}};\ \dot{\epsilon}_s = \sqrt{\frac{2}{3}}\|\dot{\boldsymbol{e}}\| \tag{2.17}$$

where $\dot{\boldsymbol{e}} = \dot{\boldsymbol{\epsilon}} - 1/3\dot{\epsilon}_v\boldsymbol{\delta}$ is the deviatoric component of the strain rate tensor. Using the aforementioned invariants of the stress tensor, the yield function F and the plastic potential function G for the D-P model can be defined as

$$F(p, q, \mu) = q + \mu p - c_f = 0 \tag{2.18}$$

$$G(p, q, \beta) = q + \beta p - c_q \tag{2.19}$$

where c_f is a cohesion parameter, and $c_f = 0$ for cohesionless granular materials; c_q is a cohesion-like parameter that ensures the plastic potential surface G is always attached to the current stress point. μ and β are two internal variables. On p versus q plot, the above yield surface represents a straight line. Further more, the gradient of the function can be

computed as

$$\boldsymbol{f} : = \frac{\partial F}{\partial \boldsymbol{\sigma}} = \frac{1}{3}\mu \mathbf{1} + \sqrt{\frac{3}{2}}\hat{\boldsymbol{n}} \tag{2.20}$$

$$\boldsymbol{g} : = \frac{\partial G}{\partial \boldsymbol{\sigma}} = \frac{1}{3}\beta \mathbf{1} + \sqrt{\frac{3}{2}}\hat{\boldsymbol{n}} \tag{2.21}$$

where $\hat{\boldsymbol{n}} := \boldsymbol{s}/||\boldsymbol{s}||$ is the unit direction vector for the deviatoric stress tensor $\boldsymbol{s}$.

There are two plastic internal variables involved in the D-P model: frictional parameter μ and dilatancy parameter β. The physical significance of μ is that it relates the allowable increase (or decrease) in shear stress for a given increase in pressure. On the other hand, β represents the the corresponding increase (or decrease) in plastic shear strain to a given change in plastic volumetric strain. At yielding ($F = 0$), μ and β can be obtained as

$$\mu = -\frac{q}{p};\ \beta = \frac{\dot{\epsilon}_v^p}{\dot{\epsilon}_s^p} \tag{2.22}$$

These physical interpretations afford the model a clear linkage to micromechanics, as will be presented Chapter 4 – 6 of this dissertation.

2.2. Governing equations and finite element implementations with the presence of strong discontinuities

This section will cover governing equations (strong form, weak form), as well as finite element implementations, for boundary value problems with the presence of strong discontinuity. As termed in [17], 'strong discontinuity' refers to discontinuity in the displacement field, while 'weak discontinuity' involves discontinuity in the deformation gradient.

2.2.1. Governing equations

The domain of interest here is a body Ω split into two parts, Ω_+ and Ω_-, by a surface of discontinuity $\mathcal{S}$. Γ_u and Γ_t are the boundaries subjected to the usual essential and natural boundary conditions, respectively. $\boldsymbol{v}$ is the outward norm of the boundary Γ. $\boldsymbol{n}$ is the unit norm of the discontinuity surface $\mathcal{S}$, pointing to Ω_+. An additional subdomain $\Omega^h \subset \Omega$ is defined by two arbitrary boundaries *ahead* ($\mathcal{S}^h_+$) and *behind* ($\mathcal{S}^h_-$) the discontinuity surface, and split by $\mathcal{S}$ into the subdomains Ω^h_+ and Ω^h_-. This sub-domain defines the local support of the discontinuity surface. Also, it is assumed that Γ_u is outside Ω^h ($\Gamma_u \cap \Omega^h = \emptyset$).

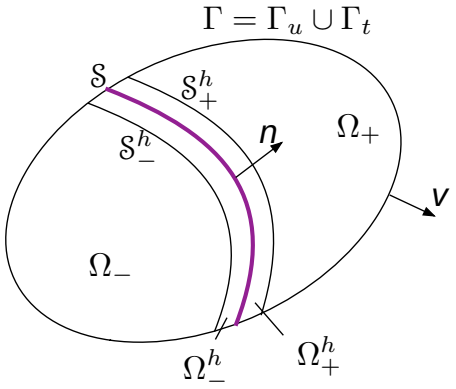

Figure 2.1. Domain Ω with the surface of discontinuity $\mathcal{S}$.

The total displacement field can be decomposed into a continuous part and a discontinuous part as

$$\boldsymbol{u}(\boldsymbol{x}) = \underbrace{\bar{\boldsymbol{u}}(\boldsymbol{x})}_{\text{continuous}} + \underbrace{M_{\mathcal{S}}(\boldsymbol{x})[\![\boldsymbol{u}]\!](\boldsymbol{x})}_{\text{discontinuous}} \tag{2.23}$$

where $[\![\boldsymbol{u}]\!](\boldsymbol{x})$ is the displacement jump. The scalar function $M_{\mathcal{S}}(\boldsymbol{x})$ generates discontinuity on the surface and is given by

$$M_{\mathcal{S}}(\boldsymbol{x}) = H_{\mathcal{S}}(\boldsymbol{x}) - f^h(\boldsymbol{x}), \text{ with supp}\,[\mathrm{M}_{\mathcal{S}}] = \Omega_+^{\mathrm{h}} \cup \Omega_-^{\mathrm{h}} \tag{2.24}$$

where "supp" means the support of a function. $H_{\mathcal{S}}(\boldsymbol{x})$ is the Heaviside function on $\mathcal{S}$ defined by

$$H_{\mathcal{S}}(\boldsymbol{x}) = \begin{cases} 1 & \boldsymbol{x} \in \Omega_+ \\ 0 & \boldsymbol{x} \in \Omega_- \end{cases} \tag{2.25}$$

and $f^h(\boldsymbol{x})$ is any arbitrary smooth function that satisfies the following requirements

$$f^h(\boldsymbol{x}) = \begin{cases} 1 & \boldsymbol{x} \in \Omega_+ \backslash \Omega_+^h \\ 0 & \boldsymbol{x} \in \Omega_- \backslash \Omega_-^h \end{cases} \tag{2.26}$$

The local (strong) form of the quasi-static equilibrium equations with the presence of discontinuity surface may be expressed as [18, 19]: Given $\boldsymbol{b} : \Omega \to \mathbb{R}^{ndim}$, $\boldsymbol{t}^* : \Gamma_t \to \mathbb{R}^{ndim}$ and $\boldsymbol{u}^* : \Gamma_u \to \mathbb{R}^{ndim}$, find $\boldsymbol{u} : \Omega \times [0, T] \to \mathbb{R}^{ndim}$ ($[0, T]$ is the time interval of interest), such that

$$\nabla \cdot \boldsymbol{\sigma} + \boldsymbol{b} = \mathbf{0} \text{ in } \Omega \backslash \mathcal{S} \tag{2.27}$$

$$\boldsymbol{u} = \boldsymbol{u}^* \text{ on } \Gamma_{\mathrm{u}} \tag{2.28}$$

$$\boldsymbol{\sigma} \cdot \boldsymbol{v} = \boldsymbol{t}^* \text{ on } \Gamma_{\mathrm{t}} \tag{2.29}$$

$$\boldsymbol{\sigma}_+ \cdot \boldsymbol{n} = \boldsymbol{\sigma}_- \cdot \boldsymbol{n} \text{ on } \mathcal{S} \tag{2.30}$$

$$\boldsymbol{\sigma}_{\mathcal{S}} \cdot \boldsymbol{n} = \boldsymbol{\sigma}_+ \cdot \boldsymbol{n} (= \boldsymbol{\sigma}_- \cdot \boldsymbol{n}) \text{ on } \mathcal{S} \tag{2.31}$$

where $\boldsymbol{b}$ is the body force, $\boldsymbol{u}^*$ and $\boldsymbol{t}^*$ are prescribed displacement and traction vectors, respectively. Equations (2.27), (2.28) and (2.29) are the classical strong form for quasi-static problems with continuous displacement fields. In equations (2.30) and (2.31), $\sigma_{\mathcal{S}}$ is the stress field on the surface $\mathcal{S}$. $\boldsymbol{\sigma}_+$ and $\boldsymbol{\sigma}_-$ are the stress fields in Ω_+ and Ω_-, respectively. Equations (2.30) and (2.31) state the traction vector continuity condition across the band and provide additional set of equations to solve for the displacement jump.

The variational (weak) form of the quasi-static equilibrium equations may be expressed as [18, 19]: Given $\boldsymbol{b} : \Omega \to \mathbb{R}^{ndim}$, $\boldsymbol{t}^* : \Gamma_t \to \mathbb{R}^{ndim}$ and $\boldsymbol{u}^* : \Gamma_u \to \mathbb{R}^{ndim}$, find $\boldsymbol{u} \in \mathcal{U}$, such that for all $\boldsymbol{\eta} \in \mathcal{V}$

$$\int_\Omega \nabla^s \boldsymbol{\eta} : \boldsymbol{\sigma} \mathrm{d}\Omega = \int_\Omega \boldsymbol{\eta} \cdot \boldsymbol{b} \mathrm{d}\Omega + \int_{\Gamma_t} \boldsymbol{\eta} \cdot \boldsymbol{t} \mathrm{d}\Omega + \int_{\mathcal{S}} \boldsymbol{\eta} \cdot (\llbracket \boldsymbol{\sigma} \rrbracket \cdot \boldsymbol{n}) \mathrm{d}\Gamma \tag{2.32}$$

where $\boldsymbol{\eta}$ is the test functions. $\mathcal{V}$ is the space of admissible test functions

$$\mathcal{V} = \{\boldsymbol{\eta} : \Omega \to \mathbb{R}^{ndim} | \boldsymbol{\eta} = \boldsymbol{0} \text{ on } \Gamma_u\} \tag{2.33}$$

and $\mathcal{U}$ is the space of admissible trial solutions

$$\mathcal{U} = \{\boldsymbol{u} : \Omega \to \mathbb{R}^{ndim} | \boldsymbol{u} = \boldsymbol{u}^* \text{ on } \Gamma_u\} \tag{2.34}$$

It is shown in [18] that the weak form (2.32) together with admissible test function $\boldsymbol{\eta} \in \mathcal{V}$ yield the the governing equations (the strong form) given by (2.27) $--$ (2.31). Therefore, the boundary value problem can be solved equivalently by considering the

weak form (2.32) with admissible trial solutions, test functions and necessary constitutive equations.

2.2.2. Finite element implementations: Petrov-Galerkin formulation

Consistent with the displacement field (2.23), the admissible test function may be defined as

$$\boldsymbol{\eta} = \bar{\boldsymbol{\eta}} + M_{\mathcal{S}}\boldsymbol{\beta} \tag{2.35}$$

where $\bar{\boldsymbol{\eta}}$ is the regular part of the test function that satisfies $\bar{\boldsymbol{\eta}} = 0$ on the essential boundary Γ_u, $M_{\mathcal{S}}\boldsymbol{\beta}$ is the variation jump on $\mathcal{S}$ for any $\boldsymbol{\beta} \in \mathbb{R}^{ndim}$.

Then, the gradient of the test function consists of a regular part and an enhanced part

$$\nabla^s \boldsymbol{\eta}^h = \underbrace{\nabla^{\mathrm{s}} \bar{\boldsymbol{\eta}}^h}_{\text{regular}} + \underbrace{\tilde{\boldsymbol{\gamma}}^h}_{\text{enhanced}} \tag{2.36}$$

The field of test functions for enhanced strain is derived by construction so that the stability and convergence condition set forth in [20] and [21] are satisfied. A specific field of test functions satisfying such requirement is given as

$$\tilde{\boldsymbol{\mathcal{E}}}_{\gamma}^{h} = \left\{ \tilde{\boldsymbol{\gamma}}^h \in \left(H^0\right)^{ndim} \mid \tilde{\boldsymbol{\gamma}}^h = \left(-\frac{l_{\mathcal{S}}}{A^e} + \delta_{\mathcal{S}} \right) \boldsymbol{\psi} \right\} \tag{2.37}$$

where in two dimensions, $l_{\mathcal{S}}$ is the length of the discontinuity line and A^e is the area of the localized element.

As for the trial solutions, the discontinuous displacement fields (2.23) result in strain fields with delta functions. The conventional finite element methods cannot meet such

conditions and therefore, special treatment is needed. One common method is the assumed enhanced strain method [21], where the character of the discontinuity is captured by local enrichment of the strain fields at the element level. The total strain field consists of a regular part and an enhanced part

$$\boldsymbol{\epsilon}^h = \underbrace{\nabla^{\mathrm{s}} \bar{\boldsymbol{u}}^h}_{\text{regular}} + \underbrace{\tilde{\boldsymbol{\epsilon}}^h}_{\text{enhanced}}, \ \tilde{\boldsymbol{\epsilon}}^h = (\llbracket \boldsymbol{u} \rrbracket \otimes \nabla M_{\mathrm{S}}^h)^{\mathrm{s}} \tag{2.38}$$

The space of trial functions for the enhanced strain is then given as

$$\tilde{\boldsymbol{\mathcal{E}}}_{\epsilon}^h = \left\{ \tilde{\boldsymbol{\epsilon}}^h \in \left(H^0\right)^{ndim} \mid \tilde{\boldsymbol{\epsilon}}^h = (\llbracket \boldsymbol{u} \rrbracket \otimes \nabla M_{\mathrm{S}}^h)^{\mathrm{s}} \right\} \tag{2.39}$$

In general, we may have $\tilde{\boldsymbol{\mathcal{E}}}_{\epsilon}^h \neq \tilde{\boldsymbol{\mathcal{E}}}_{\gamma}^h$, which is a situation of the so-called Petrov-Galerkin formulation. Within this context, the standard variational formulation of the discretized finite element problem is given by the following equations

$$\int_{\Omega^e} \nabla^s \bar{\boldsymbol{\eta}}^h : \dot{\boldsymbol{\sigma}} \mathrm{d}\Omega = \int_{\Omega^e} \nabla^s \bar{\boldsymbol{\eta}}^h : \dot{\boldsymbol{b}} \mathrm{d}\Omega + \int_{\Gamma^e} \nabla^s \bar{\boldsymbol{\eta}}^h : \dot{\boldsymbol{t}} \mathrm{d}\Gamma \tag{2.40}$$

$$\int_{\Omega^e} \tilde{\boldsymbol{\gamma}}^h : \dot{\boldsymbol{\sigma}} \mathrm{d}\Omega = 0 \tag{2.41}$$

Equation (2.40) is the standard weak form of equilibrium. Equation (2.41) implies the traction continuity condition across the discontinuity surface $\mathcal{S}$, and can be shown to recover the consistency condition on the band [22].

To obtain the matrix form, we make the substitutions

$$\bar{\boldsymbol{\eta}}^h \rightarrow \boldsymbol{N}\boldsymbol{p}^e, \ \nabla^s \bar{\boldsymbol{\eta}}^h \rightarrow \boldsymbol{B}\boldsymbol{p}^e, \ \boldsymbol{\psi} \rightarrow \boldsymbol{\alpha}^e, \ (\boldsymbol{m} \otimes \nabla f^h)^s \rightarrow \boldsymbol{\beta}^e \tag{2.42}$$

where $\boldsymbol{p}^e$ is an arbitrary vector of nodal displacements, $\boldsymbol{\psi} := \partial F/\partial \boldsymbol{\sigma}$. Making use of the constitutive equations (e.g., equation (5.11)), the matrix form is then written as

$$\begin{bmatrix} \boldsymbol{K}^e_{dd} & \boldsymbol{K}^e_{d\xi} \\ \boldsymbol{K}^e_{\xi d} & \boldsymbol{K}^e_{\xi\xi} \end{bmatrix} \begin{Bmatrix} \dot{\boldsymbol{d}}^e \\ \dot{\xi}^e \end{Bmatrix} = \begin{Bmatrix} \dot{\boldsymbol{F}}^e_{\text{ext}} \\ 0 \end{Bmatrix} \tag{2.43}$$

where $\dot{\boldsymbol{d}}^e$ is the nodal displacement rate vector, the components of stiffness matrix $\boldsymbol{K}^e$ are

$$\boldsymbol{K}^e_{dd} = \int_{\Omega^e} \boldsymbol{B}^T \boldsymbol{D}^E \boldsymbol{B} \mathrm{d}\Omega^e, \ \boldsymbol{K}^e_{d\xi} = \int_{\Omega^e} \boldsymbol{B}^T \boldsymbol{D}^E \boldsymbol{\beta}^e \mathrm{d}\Omega^e,$$

$$\boldsymbol{K}^e_{\xi d} = \int_{\Omega^e} \boldsymbol{\alpha}^{eT} \boldsymbol{D}^E \boldsymbol{B} \mathrm{d}\Omega^e, \ \boldsymbol{K}^e_{\xi\xi} = -\int_{\Omega^e} \left(\boldsymbol{\alpha}^{eT} \boldsymbol{D}^E \boldsymbol{\beta}^e + H \right) \mathrm{d}\Omega^e \tag{2.44}$$

where $\boldsymbol{D}^E$ is the matrix counterpart of the elastic moduli $\boldsymbol{c}^e$. The external force $\dot{\boldsymbol{F}}^e_{\text{ext}}$ is written as

$$\dot{\boldsymbol{F}}^e_{\text{ext}} = \int_{\Omega^e} \boldsymbol{N}^T \dot{\boldsymbol{b}} \mathrm{d}\Omega^e + \int_{\Gamma^e} \boldsymbol{N}^T \dot{\boldsymbol{t}} \mathrm{d}\Gamma^e \tag{2.45}$$

Element level condensation is then performed to eliminate $\dot{\xi}^e$, which is assumed to be piecewise constant in the assumed enhanced strain method.

2.2.3. Finite element implementations: standard Galerkin formulation

An alternative way for matrix formulation, as recently proposed by [22, 23, 24, 25], eliminates $\dot{\xi}^e$ at the material point level and utilizes the standard Garlerkin approximation. This is a great advantage from an implementation point of view, since the modification to an existing FE code is restricted to material subroutine. The idea is to consider the

following form of weighting function that belongs to the test space $\tilde{\boldsymbol{\mathcal{E}}}^h_\gamma$ in equation (2.37)

$$\tilde{\boldsymbol{\gamma}}^h = \left(-\frac{l_{\mathrm{S}}}{A^e} + \delta_{\mathrm{S}}\right)\boldsymbol{\psi},\ \boldsymbol{\psi} = \frac{\partial F}{\partial \boldsymbol{\sigma}} \tag{2.46}$$

Substitute equation (2.46) into the auxiliary weak equation (2.41) and assume that $\boldsymbol{\psi} : \dot{\boldsymbol{\sigma}}$ is constant along the discontinuity surface

$$\frac{l^e_{\mathrm{S}}}{A^e}\int_{\Omega^e} \boldsymbol{\psi} : \dot{\boldsymbol{\sigma}}\mathrm{d}\Omega = l^e_{\mathrm{S}}\boldsymbol{\psi} : \dot{\boldsymbol{\sigma}} \tag{2.47}$$

Then, take into consideration that $\dot{\xi}^e$ is piece-wise constant for each localized element, the consistency condition on the band for the localized element is

$$\int_{\Omega^e} \boldsymbol{\psi} : \dot{\boldsymbol{\sigma}}\mathrm{d}\Omega - \int_{\Omega^e} \dot{\xi}^e \tilde{H}_\delta \mathrm{d}\Omega = 0 \tag{2.48}$$

Then, the Cauchy stress tensor is given

$$\dot{\boldsymbol{\sigma}} = \boldsymbol{c}^{ep} : \nabla^s \dot{\tilde{\boldsymbol{u}}} \tag{2.49}$$

where $\boldsymbol{c}^{ep}$ is the elastoplastic tangent. Then, the matrix form for the weak equation (2.40) is written as

$$\boldsymbol{K}^e \dot{\boldsymbol{d}}^e = \dot{\boldsymbol{F}}^e_{\mathrm{ext}} \tag{2.50}$$

$\dot{\boldsymbol{F}}^e_{\mathrm{ext}}$ is given in equation (2.45), stiffness matrix $\boldsymbol{K}^e$ is

$$\boldsymbol{K}^e = \int_{\Omega^e} \boldsymbol{B}^T \boldsymbol{D}^{EP} \boldsymbol{B}\mathrm{d}\Omega^e \tag{2.51}$$

where $\boldsymbol{D}^{EP}$ is the matrix form of $\boldsymbol{c}^{ep}$. The above mentioned formulation was used in constant strain elements, as in [22, 23], and generalized to non-constant strain interpolated elements such as the 4-node quadrilateral elements or the 8-node brick elements, for small deformation [24] as well as finite strains [25]. It is shown to be equivalent to the Petrov-Galerkin formulation.

CHAPTER 3

Bridging continuum scales: multiscale random fields in geomechanics

This Chapter is published in: Q. Chen, A. Seifried, J.E. Andrade and J.W. Baker. Characterization of random fields and their impact on the mechanics of geosystems at multiple scales. *International Journal for Numerical and Analytical Methods in Geomechanics*, doi:10.1002/nag.999, 2010.

Abstract

The behavior of particulate media, such as sands, is encoded at the granular-scale and hence methods for up-scaling such behavior across relevant scales of interest—from granular-scale ($\sim$1mm) to field-scale (>1m)—are needed to attain a more accurate prediction of soil behavior. Multi-scale analysis is especially important under extreme conditions such as strain localization, penetration or liquefaction, where the classical constitutive description may no longer apply. In this paper, internally-consistent probabilistic models for undrained shear strength and Young's modulus are developed at multiple scales, and incorporated into a simulation framework where refinement of the material description to finer scales is pursued only as necessary. This probabilistic simulation approach is then coupled with the finite element method. Numerical examples are presented to show how the performance of the geosystem is influenced by taking into account multi-scale random fields.

3.1. Introduction

It is well known that material inhomogeneities exist at different length-scales in geomechanical problems. Two types of inhomogeneities can be identified: (1) inherent inhomogeneities, which are those resulting from fluctuations in material properties such as permeability or strength; (2) induced inhomogeneities, which are those imposed by a physical phenomenon (e.g., deformation) that alters the characteristics of the medium. Figure 3.1 shows typical scales relevant to granular materials. All the information pertaining to granular systems, including inhomogeneities, is encoded at the granular scale and propagated or upscaled through all the way to the field scale. It should be pointed out that the spatial randomness at the macro-scale might be of a different stochastic nature than that of the grain-scale, e.g., randomness in macroscopic Young's modulus vs. randomness in particle elasticity. Even though the scale of interest in this paper is still within the continuum domain, properties within this domain of interest may be fundamentally influenced by grain scale properties.

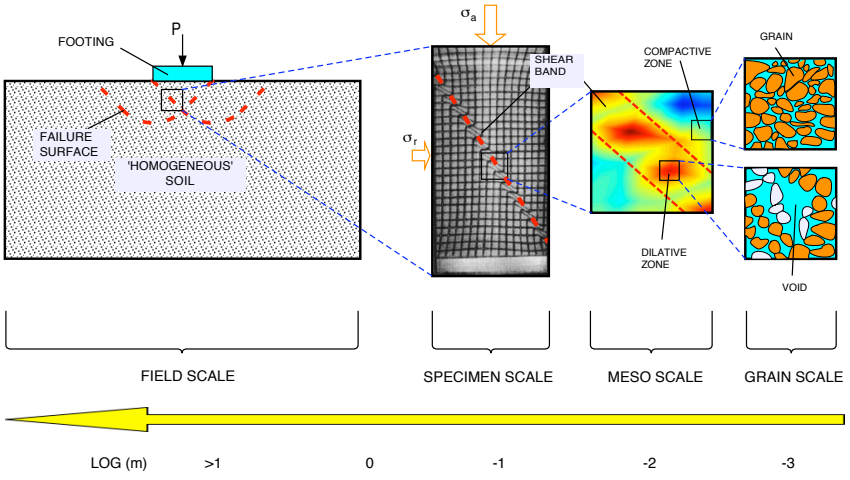

Figure 3.1. Multi-scale nature of granular materials. After [1].

Inherent inhomogeneities are commonly modeled through the use of random field theory and the finite element method (FEM). The effect of inhomogeneities on mechanical behavior of engineering problems have been studied by many researchers at a single scale. For instance, at the site scale, Griffiths and Fenton [26], Griffiths et al. [27] and Popescu et al. [28] have simulated shallow foundation resting on soils with spatially varying properties. It has been shown that inherent inhomogeneities of soil strength can greatly modify the basic form of failure mechanism of the foundation. More recently, Andrade et al. [1] have coupled advanced elastoplastic models with geostatistical tools to simulate the mechanical behavior of anisotropic samples of sands and showed that meso-scale inhomogeneities in the porosity trigger global instabilities that are responsible for a significant reduction in the load-carrying capacity of the samples. They have also observed that the upscaling of porosity fields delays the predicted onset of localization due to local averaging over mesh elements. In dealing with material inhomogeneities and their effects on geosystems across scales, the conventional methods need to be extended. Along this line, a multi-scale stochastic FEM has been recently developed ([29, 30, 31]). In this approach, the original boundary value problem of random heterogeneous materials is decomposed into a slow (coarse) scale deterministic BVP and a fast (fine) scale stochastic BVP. The slow scale problem is solved first using standard FEM and the solution is used as input for fast scale BVP. In this paper, we propose methods to characterize random fields and to couple them with finite elements (FEs) at both coarse and fine scales.

Parallel to the development of modeling material inhomogeneities utilizing random field theory and the FEM, multi-scale methods have become the subject of intensive research during the past decade, especially for modeling heterogeneous materials. According to the taxonomy introduced in [16], multi-scale methods can be classified into four types, i.e., hierarchical, concurrent (strong coupling), semi-concurrent (weak coupling) and hybrid hierarchical-semiconcurrent. One of the motivations for these methods is to bypass the prohibitive computational cost of modeling macroscopic structures using more accurate micro-scale constitutive models. One such example is the FE^2 approach (e.g., [32, 33]) for modeling composite materials. In the FE^2 method, macroscopic constitutive equations at a material point are replaced by FE simulations of periodic microstructures. A strongly-coupled multi-scale method was proposed ([34, 35, 36]) for analyzing nonlinear inelastic behavior for heterogeneous structures, where the macroscopic constitutive law is replaced by micro-scale FE computation at element level rather than at the material point. The above mentioned methods deal with material behavior that is generally described by continuum constitutive laws at different scales. More recently, Andrade and Tu [12] and Tu et al. [2] proposed a framework coupling discrete element method with the FEM for behavior prediction in granular media, where the phenomenological hardening laws at the macro-scale are bypassed and the key material parameters are extracted from granular structures directly. While our paper focuses on material behavior described by continuum constitutive models, it is possible to extend it to couple with discrete models given the work done by Andrade and Tu [12] and Tu et al. [2].

In multi-scale models, the micro-macro relation is a key component. Various algorithms have been proposed in establishing micro-macro relations based on different assumptions dealing with either weakly coupled (e.g., [**37, 38**]) or strongly coupled (e.g., [**34**], [**39**]) scales. In the weakly coupled case, the micro- and macro-scales can be fully separated and a representative volume element (RVE) or unit cell is typically used to represent the micro-structure. In the strongly coupled case, the characteristic length of micro-scale is finitely smaller—rather than infinitely smaller—than that of macro-scale. In this paper, we consider the case where different scales are strongly coupled and propose the use of a concurrent multi-scale scheme [**16**], where displacements from the macro-scale are passed onto micro-scale as boundary conditions and the averaged stresses are passed back to macro-scale. The assumptions here are that the strain and stress, at an arbitrary material point in the macroscopic domain, are the volume average of the strain and stress fields over the microscopic domain, respectively.

A corresponding consideration in multi-scale modeling is the description of the underlying material properties at multiple scales. In this work, material properties (e.g., undrained shear strength and Young's modulus) are assumed to be random but varying spatially in a somewhat smooth manner. Mathematically, this means that these properties can be quantified as random variables at a particular location, and that the value of these variables at multiple locations can be described by joint probability distributions characterized using random fields modeling. Spatial dependence for the non-Gaussian fields is introduced by first transforming the variables of interest to have marginal Gaussian distributions, and then introducing dependence among these transformed variables

through linear correlation coefficients—a procedure commonly used in the field of Geostatistics (e.g., [40]). Material properties at the coarse scale are defined by averaging values at the corresponding fine-scale locations; using this assumption, means, variances and spatial correlations at the coarse scale are then derived to be internally consistent with the fine scale. A second important piece of multi-scale random fields is Monte Carlo simulation of realizations of the field at multiple scales. Thus, an iterative simulation procedure is adopted where simulated values are obtained at individual locations conditional on all previous simulations. This procedure is beneficial here because it allows one to first simulate the field at only the coarse scale, then add simulation points at the fine scale probabilistically consistent with the previous coarse-scale realizations. Further, these conditional fine-scale simulations need not be performed immediately after the coarse-scale simulation, allowing one to start with a coarse-scale simulation, perform initial analysis on the system (either mechanics analysis, or some other analysis of the soil properties), and then refine the scale of that simulation without having to start over or generate a new simulation of the field. This adaptive refinement is expected to have important practical advantages in some situations.

The paper is organized as follows. Section 3.2 provides a description of the random material properties of interest at the fine scale, including probability distributions and spatial dependence. The conditional simulation procedure described in the previous paragraph is also introduced. In Section 3.3, a multi-scale description of the random field is introduced, and the probability distributions and correlations at that scale are derived under the assumption that coarse scale values are averages of corresponding fine scale

values. Strategies for multi-scale simulation are then discussed, including the feasibility of simulating entire fields at the coarse scale, and then refining that simulation by adding conditional simulations at the fine scale as desired. In Section 3.4, a multi-scale framework for coupling random fields and the FEM is proposed. Two main ingredients of the framework, e.g., element-splitting technique and concurrent information-passing scheme, are discussed in detail. In Section 3.5, numerical examples are presented where FE simulations of a strip footing utilizing the proposed framework are carried out. The undrained shear strength is treated as the random variable for bearing capacity analysis; the Young's modulus is treated as random for settlement analysis. Of particular interest is the impact of different degrees of fine scale discretization on the overall performance of the geosystem.

3.2. Characterization of material properties

The adopted approach for parameter simulation relies on classical random field models and Monte-Carlo methods modified to account for various scales of resolution throughout the sample. One of the challenges of this work is maintaining the appropriate spatial variability across scales. Characterization of both the distribution and spatial correlation of undrained shear strength, S_u, and Young's modulus, E, at the finest considered scale—the meso-scale—are detailed in this section.

3.2.1. Distribution of the soil properties

Beta, gamma, and lognormal distributions are all commonly used in literature to model soil properties. While no sufficient data exists supporting one type over another, Popescu

et al. [28] have observed that the values of soil strength in shallow layers are positively skewed. Based on these findings the lognormal distribution is used to describe each parameter, which can be represented by the following probability density function (PDF)

$$f_Y(y) = \frac{1}{y\sigma_{\ln Y}\sqrt{2\pi}} \exp\left(-\frac{1}{2}\left[\frac{\ln y - \mu_{\ln Y}}{\sigma_{\ln Y}}\right]^2\right) \tag{3.1}$$

where $f_Y(y)$ is used to denote the PDF and the values of $\mu_{\ln Y}$ and $\sigma_{\ln Y}$ are the mean and standard deviation of the natural log of the parameter Y, and are chosen depending on the parameter to be modeled. In this paper, the parameters (μ, σ) used for undrained shear strength and Young's modulus are (100, 50) kPa and (100, 50) MPa, respectively. Selection of these values is discussed in section 5. Note that an upper-case Y is used to denote the random variable and a lower-case y is used to describe a specific numerical value of that variable.

The random variable can also be described in the form of a cumulative distribution function (CDF)

$$F_Y(y) = \Phi\left(\frac{\ln y - \mu_{\ln Y}}{\sigma_{\ln Y}}\right) \tag{3.2}$$

where $F_Y(y)$ denotes the CDF of Y and $\Phi()$ denotes the CDF for the standard normal distribution. A PDF from equation (3.1) is plotted in Figure 3.2 alongside a histogram of simulated values. The histogram has the same general shape, but some variation is expected due to the finite number of realizations shown here.

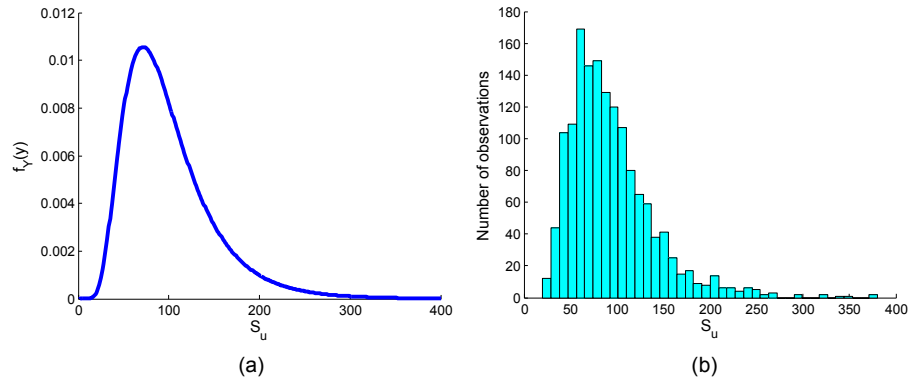

Figure 3.2. (a) Probability density function for undrained shear strength, and (b) histogram of simulated values of undrained shear strength.

3.2.2. Normal-score mapping

Realizations of the random variable at each point within the sample are dependent upon the values of the surrounding points (spatial relationships are considered in detail in the following section). For variables having Gaussian distributions, this joint dependence is fully described by pairwise linear correlation coefficients and the associated analytical equations are quite tractable. This is generally not true for non-Gaussian distributions where the associated model is not fully defined by a linear correlation coefficient, and thus a so-called normal-score mapping may be used to take advantage of the desirable Gaussian properties. In the next section, when working with fields of dependent variables, the computations will all be done using correlated Gaussian fields having a mean of zero and

variance of unity. Each value in those standard Gaussian fields will then be transformed to have the target distribution of equation (3.1) using the relationship

$$y = F_Y^{-1}\left(\Phi\left(z\right)\right) \tag{3.3}$$

where F^{-1} is the inverse CDF of the target distribution given in equation (3.2), $\Phi\left(\right)$ again denotes the CDF for the standard normal distribution, z represents a simulated value from the standard Gaussian distribution, and y is the transformed value coming from the target distribution. Figure 3.2b was created by simulating standard Gaussian samples (z) and transforming them using equation (3.3), illustrating the validity of this transform. Note that in the particular application considered here, because Y is lognormally distributed, the transformation of between Gaussian Z and lognormal Y can be performed by simply taking logarithms and exponentials, but this formulation is provided for generality.

It is assumed here that the spatial dependence introduced using this Gaussian correlation model and mapping technique is appropriate for describing the dependence of the variable being studied. Practical experience with this approach suggests that it is often a reasonable approximation [40], and because the distributions used here are not strongly non-Gaussian it is expected that dependence structure will not be significantly affected. When this transformation dramatically alters the distribution shape, the approximation may be less appropriate, although its practical advantages still make it a popular technique in those cases despite the approximation.

3.2.3. Spatial correlation

The probabilistic model of the previous section describes the distribution of a parameter value at a single location. To consider multiple locations in a specimen where the values at each location vary somewhat, spatial dependence must be taken into account. In this section, we will develop the mathematical tools for characterizing that dependence and simulating realizations of these random fields.

Spatial correlation is described here at the finest considered scale—the meso-scale—using a form of covariance known as a semivariogram, $\gamma(\mathbf{h})$, which is equal to half the variance of the difference of two random variables separated by distance $\mathbf{h}$

$$\gamma(\mathbf{h}) = \frac{1}{2}\,\mathrm{Var}\left[Z(\mathbf{u}) - Z(\mathbf{u}+\mathbf{h})\right] \tag{3.4}$$

where $Z(\mathbf{u})$ is the distribution of the Gaussian random variable at location $\mathbf{u}$. The vector distance $\mathbf{h}$ accounts for both separation distance and orientation and may be defined by a scalar measure. To simplify the relationship between distance and semicovariance, we define a scalar distance measure

$$h = \sqrt{\left(\frac{h_1}{a}\right)^2 + \left(\frac{h_2}{b}\right)^2} \tag{3.5}$$

where h_1 and h_2 are the centroidal separation distances along the field's major and minor axes, respectively, corresponding to vector distance $\mathbf{h}$, and a and b specify how quickly spatial dependence decreases along those axes. When the 'a/b' ratio equals unity the

sample is isotropic, meaning correlation decreases with distance equally in all directions. Skewing this ratio will result in banding of the sample.

The semivariogram is often used in geostatistics instead of covariance because it requires second-order stationarity of only the increments and not the underlying process. Here the two may be used interchangeably because both requirements are assumed to be satisfied, but semicovariance is used for the simulations because we are building on previous work that uses this formulation [40].

To generate samples consistent with a given semicovariance structure, we must specify a function that provides the semicovariance in equation (3.4) for a given h. The samples above are generated according to the exponential semivariogram

$$\gamma(h) = 1 - \exp(-h) \tag{3.6}$$

Correlation, ρ, at a distance h is determined directly from the value of the semivariogram

$$\rho(h) = 1 - \gamma(h) \tag{3.7}$$

Note that the above equations describe spatial dependence of the Gaussian distributed variables (Z) rather than the transformed variables having the final target distribution (Y). It is therefore necessary to verify that the desired spatial dependence relationship is upheld after the transformation of equation (3.3) is performed. Figure 3.3 compares the specified model to the empirically calculated correlation of a simulated isotropic sample pre- and post-transformation (the procedure used to generate these data will be described in the following section). The slight difference between the specified correlation and the empirical correlation of the Gaussian data is due to the finite sample size. The difference

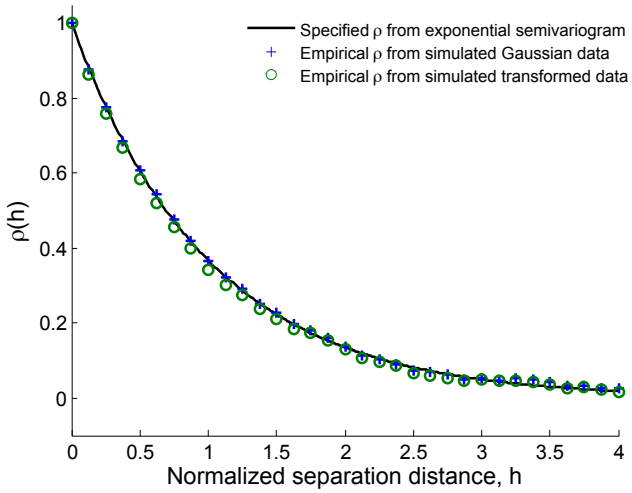

Figure 3.3. Empirical and specified correlation versus distance for a given realization of undrained shear strength.

between empirical correlation for the transformed data and the Gaussian data is due to the transformation. In this particular case the characteristics of the semivariogram are upheld well through the transformation from the Gaussian distribution to the lognormal distribution, but it is known that this correspondence will not always hold true for other marginal distributions [41].

3.2.4. Simulation

Given the specified correlation model from the previous section, we would now like to simulate sample data having that correlation structure. A sequential approach is taken here for the simulation procedure consisting of simulating each value individually, conditional upon all previously simulated values. While spectral-based simulation approaches are often preferable for random field simulation due to their stability and computational

tractability, here a sequential correlation-based approach is utilized. It is believed that this approach will be particularly valuable if one desires to do adaptive refinement at fine scales; because it is not necessary to specify *a priori* the locations requiring fine-scale resolution, one can simply add additional fine scale data, conditional upon all previously simulated data, as the need arises. An additional advantage of this approach is that it allows real data points to be incorporated. No such measurements are included here, but may be used in future work to "anchor" the simulated samples more closely to actual data. This would be accomplished by beginning the simulation with the field data included as previously generated variables, as outlined below, so that all simulated points are conditional upon them.

The first step in the sequential simulation process is to generate a single realization of a standard normal variable. All subsequent realizations are then conditional upon all previous realizations, represented by the joint distribution

$$\begin{bmatrix} Z_{\mathrm{n}} \\ \mathbf{Z}_{\mathrm{p}} \end{bmatrix} \sim N\left(\begin{bmatrix} 0 \\ \mathbf{0} \end{bmatrix}, \begin{bmatrix} \sigma_{\mathrm{n}}^2 & \mathbf{\Sigma}_{\mathrm{np}} \\ \mathbf{\Sigma}_{\mathrm{pn}} & \mathbf{\Sigma}_{\mathrm{pp}} \end{bmatrix} \right) \tag{3.8}$$

where $\sim N(\mu, \mathbf{\Sigma})$ denotes that the vector of random variables has a joint normal distribution with mean vector μ and covariance matrix $\mathbf{\Sigma}$, Z_n is the next realization to be simulated, and $\mathbf{Z}_{\mathrm{p}}$ is a vector of all previously defined or simulated points. The mean vector and covariance matrix have been partitioned to clarify several equations below. The subscripts n and p in the partitions represent "next" (as in next point to be simulated) and "previous" (as in all previously simulated points), respectively.

Individual terms inside the covariance matrix are defined by

$$COV\left[Z_i, Z_j\right] = \rho_{Z_i,Z_j} \cdot \sigma_{Z_i} \cdot \sigma_{Z_j} \tag{3.9}$$

where Z_i and Z_j refer to two locations within the random field at any scale with standard deviations σ_{Z_i} and σ_{Z_j}, respectively, and ρ_{Z_i,Z_j} is the correlation coefficient between them.

Given the above model, the conditional distribution of next realization to be simulated is given by a univariate normal distribution with updated mean and variance

$$\left(Z_{\mathrm{n}} | \mathbf{Z}_{\mathrm{p}} = \mathbf{z}\right) \sim N\left(\boldsymbol{\Sigma}_{\mathrm{np}} \cdot \boldsymbol{\Sigma}_{\mathrm{pp}}^{-\mathbf{1}} \cdot \mathbf{z}, \sigma^{\mathbf{2}} - \boldsymbol{\Sigma}_{\mathrm{np}} \cdot \ \boldsymbol{\Sigma}_{\mathrm{pp}}^{-\mathbf{1}} \cdot \boldsymbol{\Sigma}_{\mathrm{pn}}\right) \tag{3.10}$$

Once simulated, Z_{n} becomes a fixed data point in the vector $\mathbf{Z}_{\mathrm{p}}$ to be conditioned upon by all subsequent realizations. This process is repeated until all values in the field have been simulated.

3.3. Multi-scale considerations

One of the challenges of this work is maintaining appropriate spatial variability across several scales. This paper describes two scales of interest. The finer scale is denoted as scale 2, while the coarser scale is denoted as scale 1, and is defined as the average of all fine-scale points within its area. This relationship is visually represented in Figure 3.4 and is mathematically written

$$Z_{1,a} = \frac{1}{\mathrm{n}} \Sigma_{i=1}^{\mathrm{n}} Z_{2,ai} \tag{3.11}$$

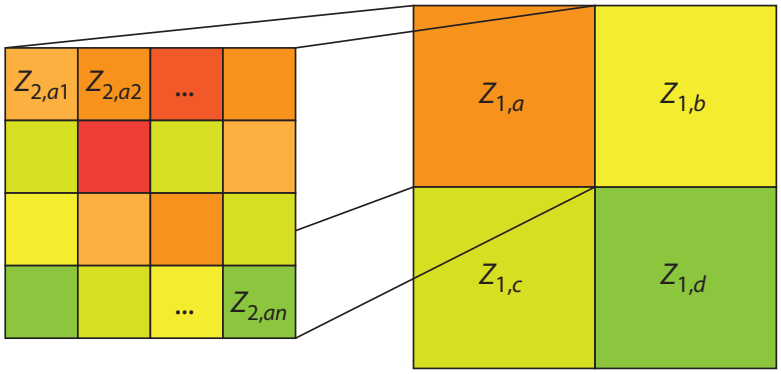

Figure 3.4. Graphical representation of material properties at 2 scales.

where the subscript a refers to the area in Figure 3.4 denoted as 'a.' All variables in the previous section were described at the fine scale. The effect of this relationship on moments of the random variables and their spatial relationships is described below.

Equation (3.11) implies that the (transformed) material properties at the coarse scale are the average values of the properties over corresponding areas at the fine scale. This relationship allows for explicit derivation of variances and spatial correlations of coarse-scale material properties, and the same averaging model will be used in the FE formulation. The optimal number of fine-scale elements to include in a coarse-scale element is likely to be problem dependent, as it balances benefits of computational efficiency with potential loss of fine scale resolution. There are also considerations to be made with respect to the transformation between the target and normal distributions at the coarse scale, which is discussed in section 3.3.2. Implications of the degree of resolution from a mechanics standpoint are explored in section 3.5.3.

3.3.1. Moments and correlation for multiple scales

At only the fine scale, simulation of random fields is relatively straightforward. As discussed above, individual values in the field follow the standard Gaussian distribution with zero mean ($\mu_{Z_2} = 0$), unit standard deviation ($\sigma_{Z_2} = 1$) and correlation coefficients specified by equation (3.7). These values are inserted into equation (3.10) to perform sequential simulation of correlated fields.

Inclusion of a coarser scale requires more careful consideration. Means, standard deviations and correlations are computed for coarse-scale z_1 values using the fine-scale information along with the definition of $Z_{1,a}$ (equation (3.11)). Taking the expectation of this definition yields the mean of $Z_{1,a}$

$$\mu_1 = E\left[Z_{1,a}\right] = \frac{1}{n}\sum_{i=1}^{n}\mu_{2,i} = 0 \tag{3.12}$$

Accordingly, if the variance of fine-scale z_2 values is unity and the mean of coarse-scale z_1 values is zero as shown above, then the coarse-scale variance $\sigma_{Z_{1,a}}$ can be computed as the expectation of equation (3.11) squared (the variance is equal to the expectation of $Z_{1,a}^2$ in this case, since the mean of $Z_{1,a}$ is zero)

$$\sigma_{Z_1}^2 = E\left[Z_{1,a}^2\right] - 0 = \frac{1}{n^2}\sum_{i=1}^{n}\sum_{j=1}^{n}\rho_{z_{2i}z_{2j}}\cdot\sigma_{z_{2i}}\cdot\sigma_{z_{2j}} \tag{3.13}$$

Correlation must be defined between all considered scale combinations. Expanding the definition of covariance and rearranging equation (3.9) to solve for correlation gives

$$\rho_{Z_i,Z_j} = \frac{COV\left[Z_i, Z_j\right]}{\sigma_{Z_i}\sigma_{Z_j}} \tag{3.14}$$

where Z_i and Z_j refer to two elements within the random field at any scale with means μ_{Z_i} and μ_{Z_j}, and other terms as defined in equation (3.9). Making the appropriate substitutions at each scale and simplifying yields the definition of correlation between two Z_1 elements (equation (3.15a)) or between a Z_1 element and a Z_2 element (equation (3.15b))

$$\rho_{Z1a,Z1b} = \frac{\sum_{i=1}^{n}\sum_{k=1}^{n}\rho_{Z2a_i,Z2b_k}}{\sum_{i=1}^{n}\sum_{j=1}^{n}\rho_{Z2a_i,Z2a_j}} \tag{3.15a}$$

$$\rho_{Z2,Z1a} = \frac{\sum_{i=1}^{n}\rho_{Z2,Z2a_i}\sigma_{Z2a_i}}{\sqrt{\sum_{i=1}^{n}\sum_{j=1}^{n}\rho_{Z2a_i,Z2a_j}\sigma_{Z2a_i}\sigma_{Z2a_j}}} \tag{3.15b}$$

where subscripts a and b refer to two different local averages as shown in Figure 3.4, and where scale 2 correlation was defined earlier in equation (3.7). These results are comparable to corresponding results for Local Average Processes in Random Fields modeling [42], but differ slightly here in that they are defined for averages of discrete values rather than a continuous process. These results are used in later calculations and are needed to ensure consistency with the FEM.

Figure 3.5 compares correlation versus the normalized scalar distance measure between all combinations of scales. Note how averaging of the fine scale points effectively increases correlation for a given distance relative to the fine scale. Non-linear variation of correlation across the coarse scale puts more emphasis on fine-scale elements in closer proximity, which slightly increases correlation for a given centroidal distance. If correlation were to somehow vary linearly with distance, the correlations would be identical at all scales. This is similar to what occurs with fractal geometrical variations, although

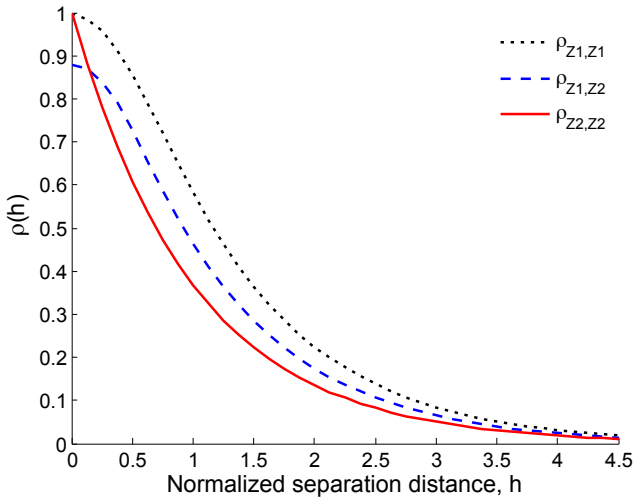

Figure 3.5. Correlation vs. distance at all scales.

that type of correlation structure is not as easily incorporated into this spatial correlation characterization.

Also note how the correlation between a fine-scale element and a local average is not unity at a distance of zero, which is expected by the definition of inter-scale correlation given by equation (3.15b). In this figure, each element at the coarse scale is subdivided into 16 fine-scale elements. If each element at the coarse scale was comprised of only a single fine-scale element, the correlation between scales at a distance of zero would be unity.

3.3.2. Normal-score mapping at the coarse scale

Figure 3.2 above verified that the target distribution is satisfactorily obtained through transformation at the fine scale, but it must be also verified that the mapping is consistent

across scales. The challenge is that the variable Y_1 at the coarse scale is defined as the average of the fine-scale y_2 values within the coarse cell, but in the sections above, multi-scale averaging has been performed on the Gaussian variables Z. When mapping back the averaged (coarse-scale) z_1 values to coarse-scale y_1 values, we need to ensure that the distribution of Y is identical to what would be attained without this normal-score mapping.

There are several possibilities for performing this mapping at the coarse scale. In the first case, we do the transforming of the simulated z_2 values at the fine scale to get fine-scale y_2 values, and then average those fine-scale y_2 values to get a coarse-scale y_1 value.

$$y_1 = \frac{1}{n}\sum_{i=1}^{n} F_{Y_2}^{-1}\left(\Phi\left(z_{2,i}\right)\right) \tag{3.16}$$

This transformation would be guaranteed to ensure the averaging properties of Y, but it is not practically feasible as we will not simulate fine-scale y_2 values at all locations (this would eliminate the benefit of multi-scale simulation). It therefore becomes necessary to perform the transformation directly on the coarse-scale y_1 values. Nonetheless, this method is used here as a benchmark for comparison of the other methods.

In a second case, we perform the transformation directly on the coarse-scale z_1 simulations, using the CDF of Y_1

$$y_1 = F_{Y_1}^{-1}\left(\Phi\left(\frac{z_1}{\sigma_{Z_1}}\right)\right) \tag{3.17}$$

In this mapping, we first re-normalize z_1 by dividing by its variance (it has mean zero, and the average of Gaussian variables is Gaussian, so no other normalization is necessary).

We then transform it using the standard Gaussian CDF and the CDF of Y_1. Note that the CDF of Y_1 is not the same as the CDF of the fine-scale Y_2. This transformation is also guaranteed to ensure the averaging properties of Y, as we have explicitly used the desired marginal distribution of Y_1 in the transformation, but it requires the additional step of finding the marginal CDF of Y_1. In most cases this cannot be done analytically, but it is possible to estimate it through a relatively simple simulation procedure.

When estimating Y_1 for equation (3.17), several alternatives are considered which vary in goodness of fit depending on the defined distribution of Y_2 and the number of fine-scale y_2 elements in each coarse-scale y_1 element. Realizations of Y_2 are first simulated and averaged. From here it is possible to compute the empirical CDF of Y_1 (this will be called equation (3.17) alternate 1), which should generally be a good approximation if sufficient realizations are generated, but in order to have the convenience of a functional form two more methods are examined. As more fine-scale y_2 elements are included in the each y_1 elements, it becomes more appropriate to approximate Y_1 as Gaussian with estimated parameters (equation (3.17) alternate 2). With fewer fine-scale y_2 elements included in each y_1 element—and when the distribution of Y_2 is similar to Gaussian—it may instead be appropriate to approximate Y_1 by the same form as that of Y_2, first taking care to update the parameters to reflect the effect of equation (3.11) (equation (3.17) alternate 3).

As a third transformation case, we simply use the fine-scale transformation but input coarse-scale z_1 values

$$y_1 \cong F_{Y_2}^{-1}\left(\Phi\left(z_1\right)\right) \tag{3.18}$$

The z_1 values have less than unit standard deviation (equation (3.13)), so putting them through this transformation will result in coarse-scale y_1 simulations where value in the tails of the distribution are less likely. This is as desired, due to the averaging process. There is no guarantee, however, that the y_1 values will have the desired marginal distribution in this case. Note that due to the central limit theorem, the marginal distribution of Y_1 will tend toward Gaussian as more fine-scale elements are included in the average. In particular, the quality of the approximate transformation of equation (3.18) depends upon the similarity of the fine-scale distribution to a Gaussian distribution. This tendency may need to be accounted for by explicitly using the revised coarse-scale distribution in the mapping (equation (3.17)). This is the simplest mapping of the above three cases, but the lack of guaranteed match with the desired marginal distribution is a disadvantage.

Figure 3.6 depicts empirical CDF's of coarse-scale elements obtained by three different methods. As mentioned above, the transformation of equation (3.16) is considered the benchmark, but it is not feasible in this multi-scale context for obtaining coarse-scale values in the target distribution. It is obvious from the figure that in this case it is most appropriate to approximate the marginal distribution of Y_1 as lognormal (mapping by equation (3.17) alternate 3 using the the same form as Y_2 with the mean and standard deviation updated by equations (3.12) and (3.13)). It is worth noting that this method works best for this particular fine-scale distribution and number of elements included in the coarse scale, but it is not guaranteed to work in a general sense, so a similar check is recommended for each particular distribution of Y_2 and degree of refinement.

An illustration of the case where it is not adequate to use the form of Y_2 for Y_1 is represented in Figure 3.7. Here, the y_2 values (for a hypothetical distribution of porosity)

follow a truncated exponential model. As soon as these fine-scale y_2 elements are averaged to form a coarse-scale y_1 element, the extreme values of the distribution become much less likely. Thus, it is clearly inappropriate to approximate the functional form of the coarse scale as that of the fine scale (either by equation (3.18) or equation (3.17) alternate 3). Instead, Figure 3.7 suggests that the best approximation of the true marginal CDF of Y_1 is the empirical CDF obtained as described above. Transformations performed directly on coarse-scale y_1 elements would be achieved by interpolating between the points derived for the empirical model. Note that the curves for equations (3.16) and (3.17) alternate 1 are identical here because the same empirical model is used to visually represent each transformation. The purpose of including an additional example is to emphasize that in general it is adviseable to evaluate all or most of these transformation options for the coarse scale: what works well in one situation may not work at all for another.

3.3.3. Implementation

The methodology here is based on defining parameters at the finest scale of consideration. The simulation will initially generate a coarse-scale resolution of the sample, then an empirically determined set of these are further refined to the fine scale. For refinement, the same conditional framework described above is used with care taken to specify appropriate values of variance and correlation. The fact that the simulation begins at the coarse scale and works toward higher resolution should not result in a field any different than starting with a fine-scale field and subsequently averaging those elements together.

In the context of multiple scales, the sequential simulation process described above has the benefit of adaptive refinement (as introduced in section 2). If deemed necessary at

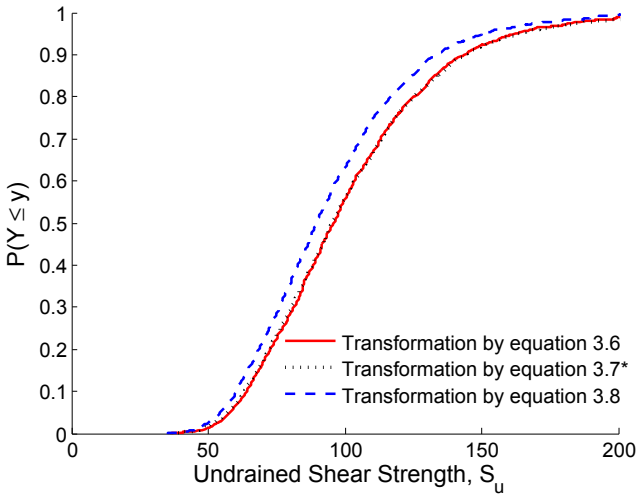

Figure 3.6. Empirical CDFs of simulations produced using several transformation approaches at the coarse scale (scale 1). The fine scale (scale 2) properties are modeled as lognormal.

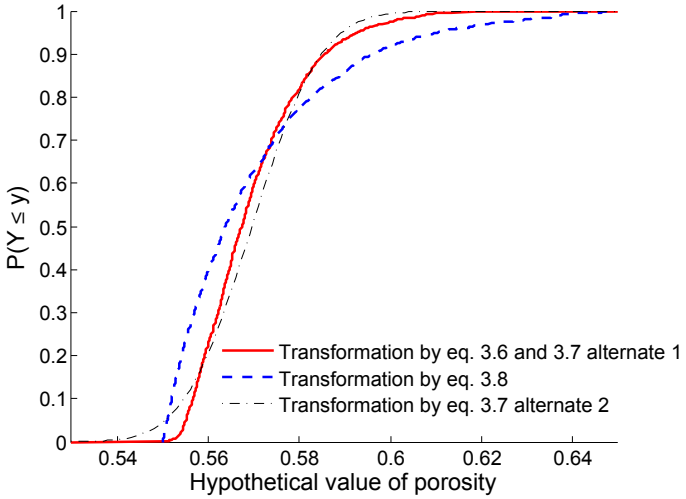

Figure 3.7. Empirical CDFs of simulations produced using several transformation approaches at the coarse scale (scale 1). The fine scale (scale 2) properties are modeled as truncated exponential.

any point in time, any element can be broken down into its fine scale components without consideration of sequence. A powerful implication of this is that the number of scales need not be limited to two; while the above definitions explicitly consider two scales, they are easily expanded to more. The finest scale is always the scale at which the soil property's CDF and spatial correlation are defined, and any number of averaging scales can be defined relative to the fine scale using recursive applications of the equations above for coarse-scale properties. If it is desired to specify soil properties at the coarse scale, then the above multi-scale definitions and results of Figure 3.5 can be used to approximately invert for the fine-scale properties that result in the desired coarse-scale properties. With this approach, it may not even be necessary to specify in advance the number of scales to consider.

Even in the two-scale case presented here, computational expense can prove significant. As the size of $\mathbf{Z_p}$ increases, the computational demand of equation (3.10) grows geometrically due to the need to invert ever-larger matrices. It therefore becomes desirable to limit the size of $\mathbf{Z_p}$ each time equation (3.10) is evaluated. To achieve this, one option is to determine a maximum distance along each axis for which to consider previously generated realizations. Another is to limit the total number of previously simulated realizations to consider correlations with (keeping only those with the highest correlations). The latter approach is adopted for this research. The motivation for these approaches is that distant soil values have little impact on the distribution of Z_n, and that even non-distant points are "shielded" from having an effect if there are many closer values with stronger correlations. These and other approaches are documented for single-scale conditional simulations [40], and appear to be generally applicable to multi-scale simulations as well.

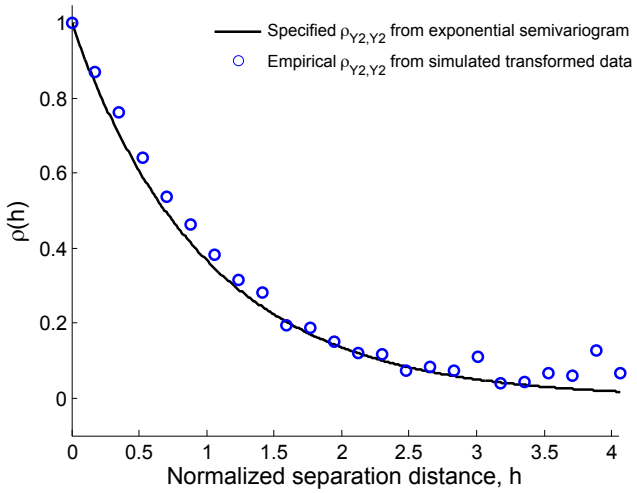

Figure 3.8. Empirical and specified correlation versus distance for a given realization of undrained shear strength, with the maximum number of conditioning elements to be considered limited to 125.

Figure 3.8 below shows that limiting the maximum number of previously generated elements with which to correlate to 125 does not adversely affect the specified spatial relationship significantly where correlation is significant. Correlation is indirectly upheld at distances greater than a radius inside which the maximum number of elements will fit. Some variation from the specified correlation is expected due to the finite sample size, but the discrepancy (relative to that in Figure 3.3) is more obvious when the maximum number of elements included in the operations precludes direct correlation. The threshold at which the additional discrepancy arises depends on the maximum number of points allowed in $\mathbf{Z_p}$ (with the discrepancy going to zero as an infinite number of points are allowed), so this number of can be varied to optimize the tradeoff between gained efficiency and lost accuracy.

As the simulation begins to refine coarse-scale elements, numerical instabilities must also be considered. As defined, the average value of all fine-scale z_2 values within a z_1 element must equal the originally simulated z_1 value. As a coarse-scale element is subdivided, the conditional variance given by equation (3.10) will tend to decrease. For the last realization of Z_2 to be simulated, only one value exists such that the average is preserved, so the conditional variance for that element will theoretically be zero. In practice, however, it is likely that the exact value will be slightly non-zero due to numerical approximations, so the simulation framework used for this research automatically sets this value appropriately. Failure to set this value manually may result in a negative (though extremely small) variance, which in turn results in an imaginary standard deviation after the inversion of equation (3.10), and therefore unrealistic realizations of Z_2.

3.4. Framework for coupling random fields and the FEM at multiple-scales

In this section, a multi-scale framework that couples random fields and the FEM is presented. The formulation of the framework is based on the assumption that the strain and stress at an arbitrary material point in the coarse-scale domain are the volume average of the strain and stress fields over the fine-scale domain. In this paper, we focus on problems with material behavior being described by continuum constitutive theories. We utilize FEs at both the macro- and micro-scales. The kinematical constraints on the fine-scale domain are first discussed. Then, the main ingredients used to construct the framework, i.e., the element-splitting technique and the concurrent information-passing scheme are proposed.

3.4.1. Kinematical constraints on the fine-scale FEs

Derivation of the kinematical constraints on fine-scale elements is based on the assumption that strain at an arbitrary point at the coarse scale is the volume average of the strain fields over the fine-scale domain. Here, we follow the discussion from [43]:

$$\boldsymbol{\varepsilon}_1 = \frac{1}{\text{meas}(\Omega)} \int_\Omega \boldsymbol{\varepsilon}_2(x) \mathrm{d}\Omega \tag{3.19a}$$

$$\boldsymbol{\varepsilon}_2 = \nabla^{\mathrm{s}} \boldsymbol{u}_2 \tag{3.19b}$$

where $\boldsymbol{\varepsilon}$ is the strain tensor, $\boldsymbol{u}$ is the displacement vector, subscripts "1" and "2" refer to macro- (coarse) and micro- (fine) scale, respectively, "meas(Ω)" is the measure of Ω, which equals to the volume (in 3D) or the area (in 2D) of the fine-scale domain and ∇^{s} is the symmetric gradient operator. Only displacement fields that satisfy equation (3.19) are said to be kinematically admissible. Furthermore, the fine-scale displacement field, $\boldsymbol{u}_2$, can be split into the sum of a linear displacement, $\boldsymbol{\varepsilon}_1 \boldsymbol{x}_2$, where $\boldsymbol{x}$ is a position vector, and a displacement fluctuation, $\tilde{\boldsymbol{u}}_2$, i.e.,

$$\boldsymbol{u}_2 = \boldsymbol{\varepsilon}_1 \boldsymbol{x}_2 + \tilde{\boldsymbol{u}}_2 \tag{3.20}$$

The corresponding fine-scale strain field is then written as,

$$\boldsymbol{\varepsilon}_2 = \boldsymbol{\varepsilon}_1 + \nabla^{\mathrm{s}} \tilde{\boldsymbol{u}}_2 \tag{3.21}$$

Substitute equation (3.21) into equation (3.19a), we have the kinematical constraint on displacement fluctuation,

$$\frac{1}{\text{meas}(\Omega)} \int_{\Omega} \nabla^{\text{s}} \tilde{\boldsymbol{u}}_2 \text{d}\Omega = 0 \tag{3.22}$$

Depending on the choice of displacement fluctuation field $\tilde{\boldsymbol{u}}_2$ that satisfies equation (3.22), we can further constrain the fine-scale displacement field. In this paper, we choose the case where the kinematical constraint on the fine scale mesh is $\tilde{\boldsymbol{u}}_2 = 0$. Following equation (3.20), we have:

$$\boldsymbol{u}_2 = \boldsymbol{\varepsilon}_1 \boldsymbol{x}_2 \tag{3.23}$$

For displacement fields that satisfy equation (3.23), it can be shown that the Hill's energy condition, $\boldsymbol{\varepsilon}_1 : \boldsymbol{\sigma}_1 = \frac{1}{\text{meas}(\Omega)} \int_{\Omega} \boldsymbol{\varepsilon}_2 : \boldsymbol{\sigma}_2 \text{d}\Omega$ is satisfied [44].

3.4.2. Element-splitting technique

In order to take into account material property fluctuations at higher resolution, the domain of interest at coarse scale needs to be further discretized. In the FEM, the domain of interest is discretized by coarse-scale elements. Naturally, the first step is to split coarse-scale FEs where needed. Consider a typical coarse-scale quadrilateral element as shown in the upper left corner of Figure 3.9. So-called "ghost nodes" are first generated using the interpolation function as

$$\boldsymbol{x}^{\text{g}} = \boldsymbol{N} \cdot \boldsymbol{x}^{\text{FE node}} \tag{3.24}$$

where $\boldsymbol{x}^{\mathrm{g}}$ is the position vector for ghost nodes, $\boldsymbol{N}$ is the interpolation function and $\boldsymbol{x}^{\text{FE node}}$ is the FE nodal position vector.

The element is then subdivided into tributary areas based on the generated ghost points and the existing FE nodes, e.g. shadow area in the coarse-scale element in Figure 3.9. Each of these tributary areas defines a domain for the finer scale, which is then further discretized using a new FE mesh. Therefore, each Gauss point at the coarse scale can be linked to a fine-scale mesh through element splitting. The information passing between these two scales will be described in the next section.

At this point, material properties at different levels of resolution will be needed and hence the method described in Sections 3.2 and 3.3 is utilized. The levels of resolution at the FE and the random field are set to match each other at each scale. Moreover, each material point in the random field is set to be at the centroid of a FE so that each element has constant material properties.

3.4.3. Concurrent information-passing scheme

Once the domain is discretized, a systematic way to access information at multiple scales is needed. Here, we propose using a concurrent information-passing scheme where essentially displacements from coarser scale are passed onto the finer scale as boundary conditions and the averaged stress is passed back from the finer scale up to the coarser scale.

The first step of this scheme is to precondition the fine-scale mesh by a homogeneous state of strain $\boldsymbol{\varepsilon}_1^{\mathrm{n}}$ and internal variables $\boldsymbol{\xi}_1^{\mathrm{n}}$, which correspond to the converged state at

previous time station t_{n} of the coarse-scale Gauss point, i.e.,

$$\boldsymbol{\varepsilon}_2^0 = \boldsymbol{\varepsilon}_1^{\mathrm{n}}; \qquad \boldsymbol{\xi}_2^0 = \boldsymbol{\xi}_1^{\mathrm{n}} \tag{3.25}$$

where the superscripts "0" refers to the initial sub-step at the fine scale computation and "n" refers to the nth time step at coarse scale computation.

This precondition step is necessary for the fine-scale computation to start from the same state as the corresponding Gauss point at the coarse scale. Following equation (3.23), displacements $\Delta\boldsymbol{u}$ are imposed on the fine-scale FE mesh by :

$$\Delta\boldsymbol{u}_2 = \Delta\boldsymbol{\varepsilon}_1 \cdot \boldsymbol{x}_2 \tag{3.26}$$

where $\Delta\boldsymbol{u}_2$ is the applied displacement boundary condition on the fine scale, $\Delta\boldsymbol{\varepsilon}_1$ is the strain increment of the coarse-scale Gauss point and $\boldsymbol{x}_2$ is the position vector of the fine scale mesh. equation (3.26) means that the fine scale displacement field is constrained to follow the coarse scale displacement field at the boundary. The imposed displacements define a new boundary value problem, where the domain is the tributary area of the coarse-scale element.

Then, the fine scale stress $\boldsymbol{\sigma}_2(x)$ is computed from the constitutive equation with the prescribed strain $\boldsymbol{\varepsilon}_2^0$ and the boundary condition $\Delta\boldsymbol{u}_2$. Upon the completion of the fine-scale FE computation, the coarse-scale stress is then obtained by the homogenization equation, i.e.,

$$\boldsymbol{\sigma}_1 = \frac{1}{\mathrm{meas}(\Omega)} \int_\Omega \boldsymbol{\sigma}_2(\boldsymbol{x})\, \mathrm{d}\Omega \tag{3.27}$$

Since we employ FEs at both scales, we rely on the Newton-Raphson iterative algorithm to solve non-linear problems. A consistent tangent operator (CTO) is needed for nonlinear FE analyses. In general, the CTO is defined as:

$$\boldsymbol{c} := \frac{\partial \boldsymbol{\sigma}}{\partial \boldsymbol{\varepsilon}} \tag{3.28}$$

where $\boldsymbol{\sigma}$ and $\boldsymbol{\varepsilon}$ are stress and strain tensors, respectively.

When we invoke the multi-scale computation for a particular coarse-scale element, to compute the corresponding CTO for the coarse scale, we use equation (3.27) and equation (3.28), and take into account the assumption that a homogeneous state of strain and strain increment are applied:

$$\begin{aligned} \boldsymbol{c}_1 : &= \frac{\partial \boldsymbol{\sigma}_1}{\partial \boldsymbol{\varepsilon}_1} \\ &= \frac{1}{\text{meas}(\Omega)} \int_\Omega \frac{\partial \boldsymbol{\sigma}_2}{\partial \boldsymbol{\varepsilon}_2} : \frac{\partial \boldsymbol{\varepsilon}_2}{\boldsymbol{\varepsilon}_1} \text{d}\Omega \\ &= \frac{1}{\text{meas}(\Omega)} \int_\Omega \boldsymbol{c}_2 : \boldsymbol{I} \text{d}\Omega \\ &= \frac{1}{\text{meas}(\Omega)} \int_\Omega \boldsymbol{c}_2 \text{d}\Omega \end{aligned} \tag{3.29}$$

where $\boldsymbol{I}$ is the fouth-order identity matrix.

Finally, the averaged stress and CTO are passed back to the Gauss point at the coarse scale for global stiffness and residual matrices assembly. Figure 3.9 summarizes the above-described multi-scale framework.

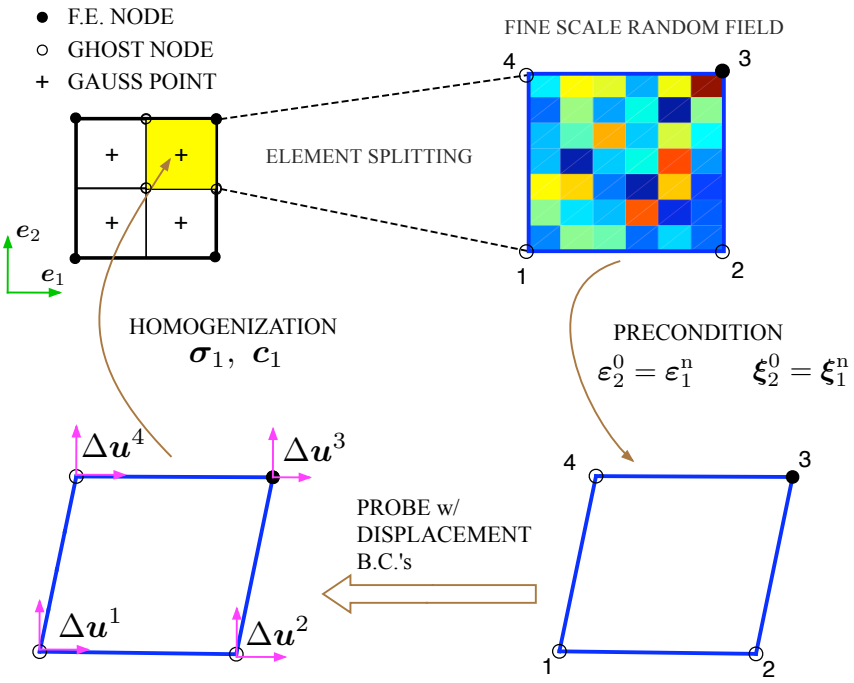

Figure 3.9. The multi-scale framework for coupling the FE method and random fields.

The above-described scheme will allow one to systematically refine the domain of interest and passing information from field scales all the way to specimen and meso-scales. The selective refining strategy, on the other hand, would allow for a more efficient solution where details are only resolved when necessary. The idea here is to zoom into zones where intense deformation is taking place. Identifying those "key areas" is a non-trivial task and may require an error estimator and an adaptive algorithm, which is beyond the focus of this paper. Here, we will loosely define such key areas through the deterministic study. For the footing problem shown later, we know *a priori* to a good extend where the intense deformation occurs.

3.5. Numerical simulations

In this section, we present numerical simulations of a typical footing problem utilizing random fields and the FEM at multiple scales. The geometry of the problem is 20 by 8 m, which is discretized by a coarse-scale FE mesh. A rough rigid footing on cohesive weightless soil is modeled with width of the footing (B) being 4m. A Drucker-Prager model [4] is used to describe the elasto-perfectly-plastic behavior of the soil. The friction angle in the following simulations is set to be zero for simplicity. Soil properties needed in the mechanical model are: Young's modulus E, Poisson's ratio ν and the undrained shear strength S_u. Both the bearing capacity and the settlement of the footing will be analyzed. S_u and E could be modeled as cross-correlated random fields for higher accuracy, e.g., via suitable correlation functions. However, it is known that S_u is the dominant factor in bearing capacity analysis, while E is the dominating factor in settlement analysis. To simplify the analysis and to focus on the effect of randomness across different scales, S_u is treated as the only spatially correlated random variable in the bearing capacity analysis with constant (deterministic) E and ν, while E is treated as a correlated random field in settlement analysis with S_u and ν being constant and deterministic.

The objective of this footing problem is to utilize the above-described framework to study the effect of random fields on the performance of the geosystem in a multi-scale context. In particular, the influence of considering finer-scale random fields will be analyzed. In the following simulations, three length parameters are of particular interest to the analysis, i.e., a, L_1 and L_2, where a is the parameter related to spacial correlation (ref: equation (3.5)) and larger value of a indicates a more smoothly varying field; L_1 is the size of a coarse-scale element, which is a constant in this paper ($L_1 = 0.5$ m); L_2 is the

size of a fine-scale element, which depends on the degree of discretization. The degree of discretization (ds) indicates how quickly a coarse-scale cell will be refined. For example, $ds = 4$ means a 1×1 cell at the coarse scale will be refined to 4×4 smaller pieces at the fine scale.

3.5.1. Deterministic study

A deterministic study was first carried out using single scale FEs (at the coarse scale) to obtain the deterministic bearing capacity and settlement, and to identify possible "key areas" that will be linked to fine-scale information. Material properties used here are: Young's modulus $E = 100$ MPa, Poisson's ratio $\nu = 0.3$, and the undrained shear strength $S_u = 100$ kPa.

Typical load-displacement curves are shown in Figure 3.10. Here, failure is said to occur when further loading no longer increases the bearing pressure (within a very small tolerance). It can be seen from Figure 3.10 that as the mesh is refined, the bearing capacity will converge to the value calculated by Prandtl's solution, $q_f = N_c S_u = 514$ kPa. Taking into account both accuracy and efficiency, we choose a coarse-scale mesh of 40×16 elements, as shown in Figure 3.11, for all simulations in the following sections. The deterministic bearing capacity for this mesh is $q_d = 556.27$ kPa, which is about 8% higher than that given by Prandtl. For rigid rough footing condition simulated here, the footing nodes settle vertically by the same amount with no rotation. When loading pressure on the footing equals 300 kPa, the deterministic settlement δ_{det} equals to 0.012 m, which can be normalized by the width of the footing, i.e., $\delta_{\text{det}}/B = 0.003$. In simulations utilizing

random fields, the settlement at 300 kPa loading pressure will be obtained and compared with this deterministic value.

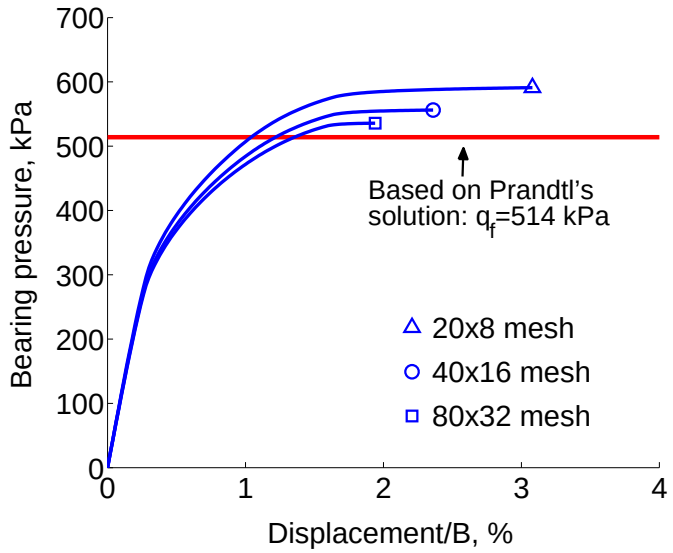

Figure 3.10. Load-displacement curves for a strip footing on homogeneous soil.

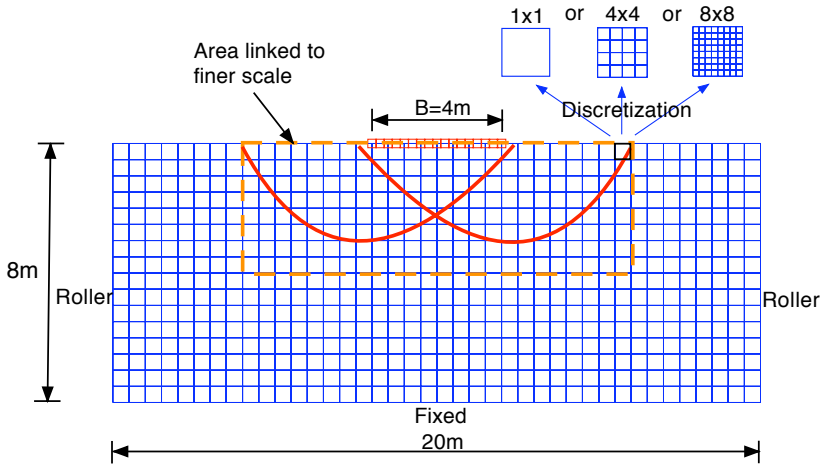

Figure 3.11. The coarse-scale FE mesh (40×16) and the area linked to the finer scale.

Figure 3.12 shows the deviatoric strain contour at failure. Intense deformation occurs at the edge of the footing and failure surfaces are clearly formed. The "key area" is therefore chosen to encompass the intense deformation zone and the failure surfaces, as shown in the dashed box in Figure 3.11. The geometry of this area is 12×4 m. Also shown in Figure 3.11 are different levels of discretization.

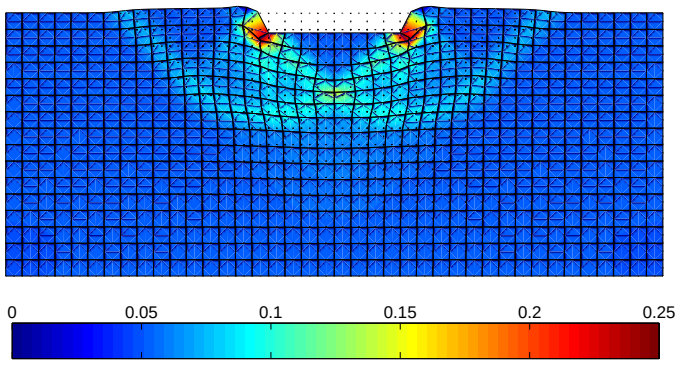

Figure 3.12. Deviatoric strain contour at failure for deterministic study.

3.5.2. Influence of multi-scale random fields on bearing capacity

In this section, the multi-scale random fields and the FEM are incorporated to simulate the footing problem. An initial coarse-scale random field for the undrained shear strength is generated using 40×16 grids and hence matching the FE resolution. Three coarse-scale correlation length parameters (normalized), i.e., $a/L_1 = 0.5$, 1.0 and 2.0 will be considered

when generating random fields. In the "key area", the fine-scale resolution will be different depending on the degree of discretization. Three particular cases with $ds = 1$, 4 and 8 are considered. The coarse-scale FE mesh will be split accordingly as shown in Figure 3.11 to match the random field resolution.

Material parameters for generating lognormally distributed random fields are the mean $\mu = 100$ kPa, which equals to the shear strength value used in the deterministic study, and the standard deviation $\sigma = 50$ kPa, which gives the coefficient of variation (COV) a value of 0.5. Constant material properties are Young's modulus $E = 100$ MPa and Poisson's ratio $\nu = 0.3$.

The initial random field simulation will first generate a coarse-scale resolution for the entire domain. This field will be referred to as "coarse-scale random field". Within the "key area", the framework described in Section 3.3 will be used to resolve the coarse-scale points down to finer pieces according to specified degree of discretization. The generated random field after this refinement process will be referred to as "multi-scale random field". Through comparison of these two types of random fields, we will show how considering finer scale information will influence the mechanical behavior of the whole system.

Typical realizations of initial undrained shear strength fields for different degrees of discretization are shown in Figure 3.13 for $a/L_1 = 2.0$. Coarse-scale random fields are on the left column and corresponding multi-scale random fields are on the right column. The degree of discretization increases from top to bottom.

Though the same material parameters, i.e., μ and σ, are used for generating every random field in this paper, they are defined at different length scales for different degrees of discretization. For every realization, we can compute the mean and standard deviation of

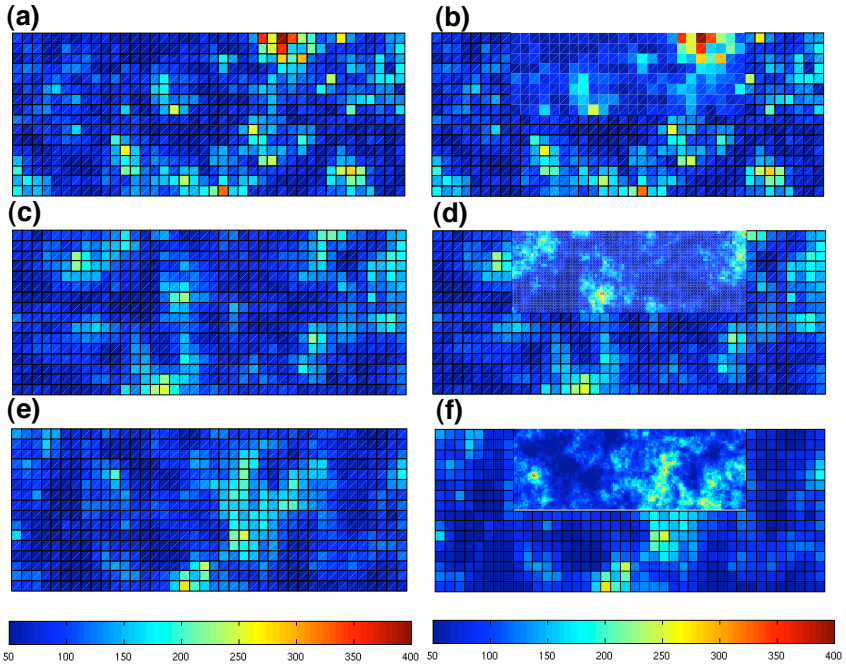

Figure 3.13. Initial undrained shear strength fields for $a/L_1 = 2.0$ with different degrees of discretization: from top to bottom: ds=1, 4 and 8 respectively with the left column being coarse-scale random fields and the right column being multi-scale random fields.

each generated random field as well as the averages of those mean and standard deviation values, as shown in Figure 3.14 and Figure 3.15. Moreover, those averaged values can be used in approximating mean bearing capacities [45].

The idea is to start from the simplified bearing capacity equation, where soil is assumed to be weightless, then

$$q_f = S_u N_c \tag{3.30}$$

If we assume Prandtl's solution for frictionless soil (as is the case in this paper) holds, then Nc is constant ($Nc = 5.14$). Take natural logarithm of equation (3.30),

$$\ln q_f = \ln S_u + \ln N_c \tag{3.31}$$

The mean of $\ln q_f$ is therefore

$$\begin{aligned} \mu_{\ln q_f} &= \mu_{\ln S_u} + \mu_{\ln N_c} \\ &= \ln \mu_{S_u} - \frac{1}{2}\ln(1 + \frac{\sigma^2_{S_u}}{\mu^2_{S_u}}) + \ln N_c \end{aligned} \tag{3.32}$$

Then the mean of q_f can be approximated as

$$\mu_{q_f} = \exp\left\{\ln N_c + \ln \mu_{S_u} - \frac{1}{2}\ln(1 + \sigma^2_{S_u}/\mu^2_{S_u})\right\} \tag{3.33}$$

This approximated analytical mean value of bearing capacity will be plotted with the results obtained by FEM computation as will be shown later.

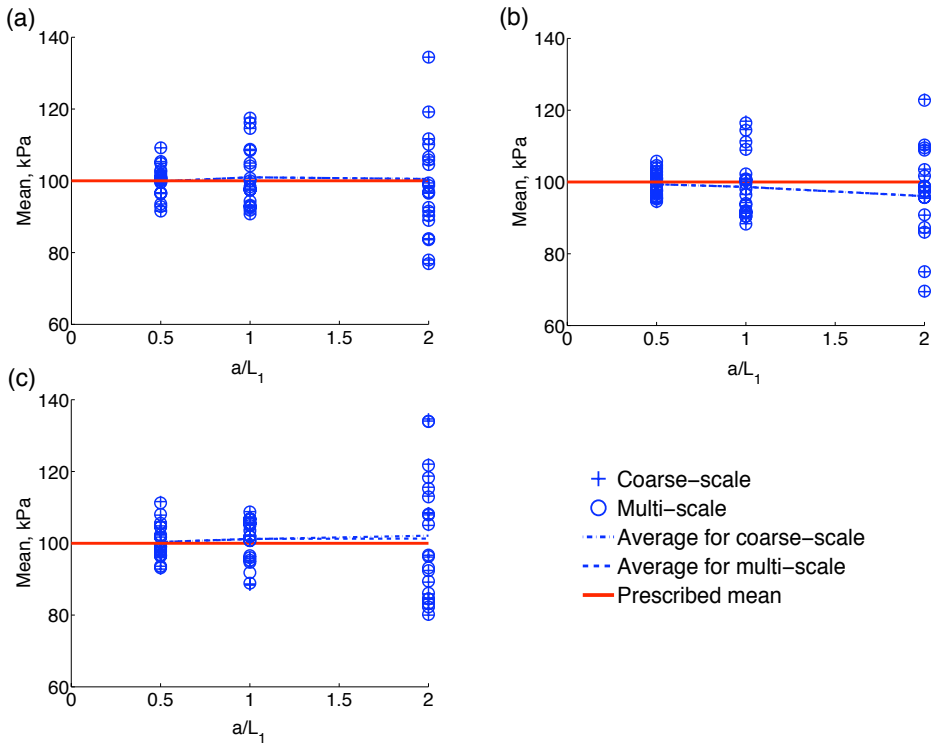

Figure 3.14. Mean for the generated initial undrained shear strength: (a) ds=1, (b) ds=4 and (c) ds=8.

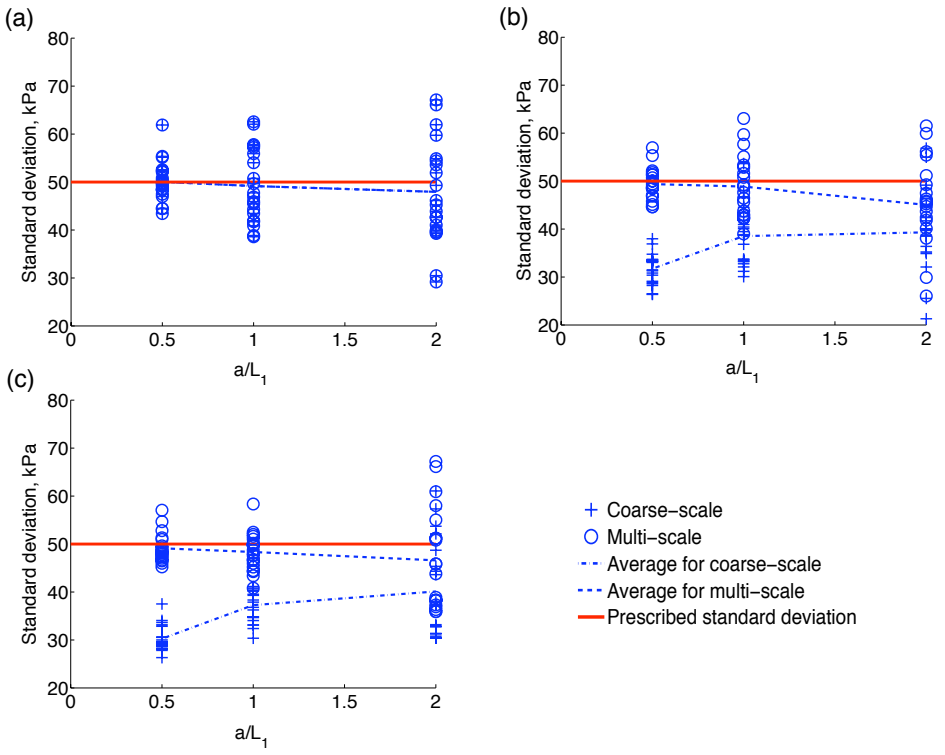

Figure 3.15. Standard deviation for the generated initial undrained shear strength: (a) ds=1, (b) ds=4 and (c) ds=8.

The load-displacement behavior obtained by random fields and deterministic analyses is shown in Figure 3.16 for all simulations. It can be seen that bearing capacities of spatially varying soil are significantly lower (18% on average) than the corresponding deterministic value.

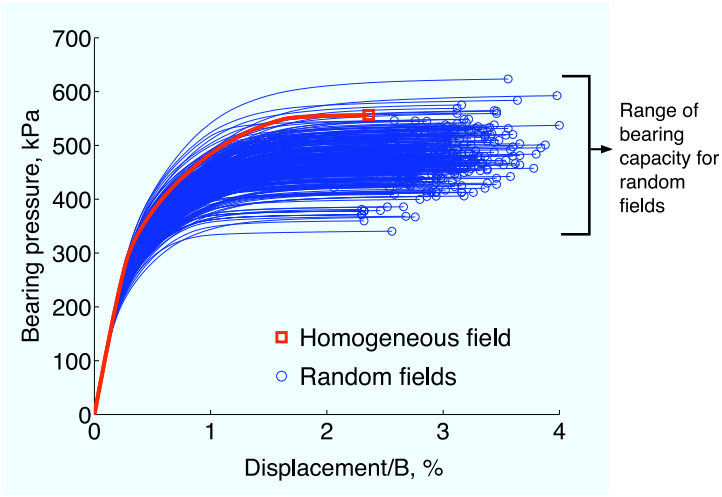

Figure 3.16. Load-displacement curves for all simulations.

Figure 3.17 shows how bearing capacities change with a/L_1 for different degrees of discretization. The first observation is that the mean bearing capacities computed by equation (3.33) are in good agreement with the FEM results especially for multi-scale cases, which shows equation (3.33) can be used as a rough estimation of mean bearing capacities. Also, it can be seen that (1) for coarse-scale results with the same discretization level, the averaged bearing capacity increases slightly as a/L_1 decreases, this observation is consistent with the standard deviation curve shown in Figure 3.15, where smaller value of a/L_1 gives a lower standard deviation and, therefore, a stronger field; (2) for coarse-scale results with the same a/L_1, the averaged bearing capacity increases with ds. This is because the coarse-scale data point is seen as the average of the fine-scale points. The averaging process effectively reduces the variability, especially for larger values of ds, which is shown in Figure 3.15 where the standard deviations for ds=4 and 8 are smaller than that of ds=1 for the same a/L_1 values. While the mean values are roughly the same

for all simulations, the reduced variability will result in stronger fields that lead to higher bearing capacities.

Even more important observation in Figure 3.17 is the effect of using multi-scale random fields. It can be seen that the mean of the bearing capacities obtained by multi-scale computation is not influenced as much by either ds or a/L_1. This is because the mean of the bearing capacities are mainly affected by the mean and standard deviation of the undrained shear strength fields, which as shown in Figures 3.14 and 3.15, are not significantly sensitive to either ds or a/L_1. Further, with ds and a/L_1 being the same, multi-scale bearing capacity results are, in general, smaller than coarse-scale ones, especially for smaller values of a/L_1. The reason is that, instead of using a local average of the material properties, multi-scale computations zoom into the specific area to obtain more detailed fine-scale information, which has roughly the same mean but higher variability than their coarse-scale counterparts (as shown in Figure 3.14 and 3.15). Therefore, this results in weaker zones that lead to lower bearing capacities. Also, the trend that the diffence between coarse-scale and multi-scale bearing capacities decreases as a/L_1 increases is consistent with the trend observed in the standard deviation of generated data shown in Figure 3.15. The above observations confirm that using averaged coarse-scale material properties tends to over-estimate the bearing capacity. In other words, coarse-scale results are less conservative.

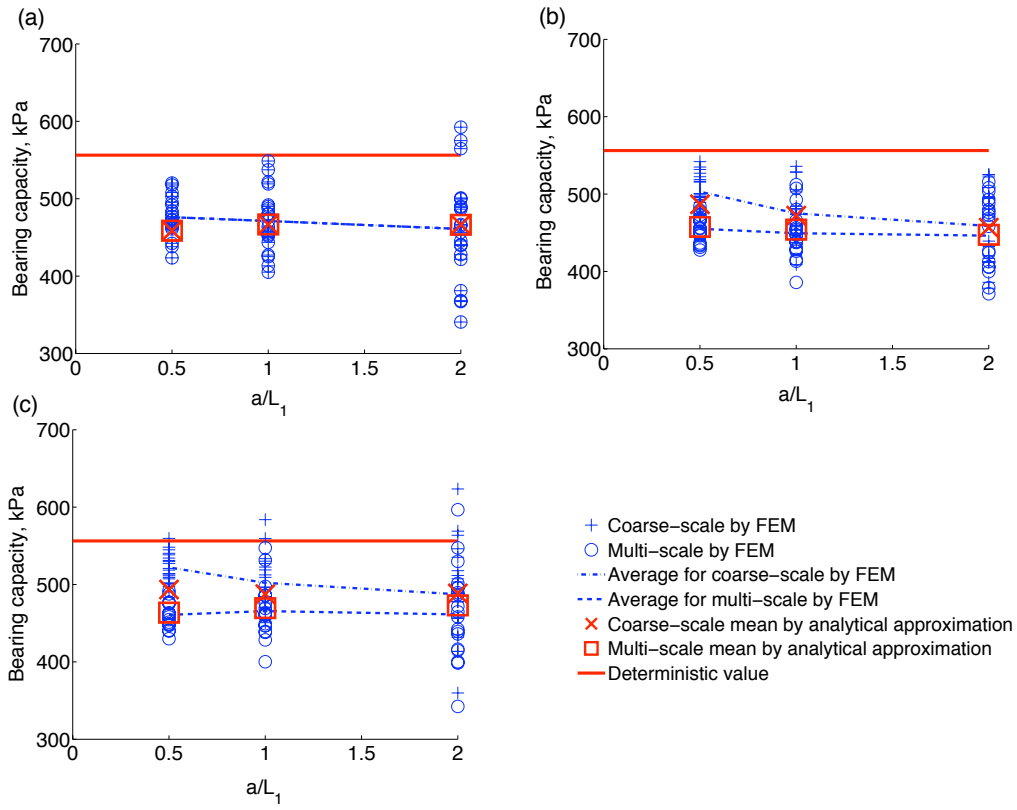

Figure 3.17. Bearing capacities for different degrees of discretization: (a) ds=1, (b) ds=4 and (c) ds=8.

Figure 3.17 shows how the bearing capacities are influenced by multi-scale random fields with different levels of discretization. However, it does not provide information on how the failure surfaces are affected by considering the random field at multiple scales. Such insight is provided in Figures 3.18, 3.19 and 3.20, which show the deviatoric strain contours for one particular realization for $a/L_1 = 0.5$ with ds=1, 4 and 8. Unsymmetrical failure surfaces can be clearly seen in these figures. In the literature, e.g., [**26**, **27**, **28**], effects of single scale random fields on formation of failure surfaces are studied. It has been shown that spatially varying soil properties trigger unsymmetrical failure surface passing

mainly through weaker soil zones. Figures 3.18, 3.19 and Figure 3.20 show clearly these trends. More interestingly, these figures show that, in multi-scale random cases there are more local fluctuations in the shear strains than in the coarse-scale cases, because higher levels of resolution are taken into account. These detailed information may lead to effectively weaker spots resulting in lower bearing capacities.

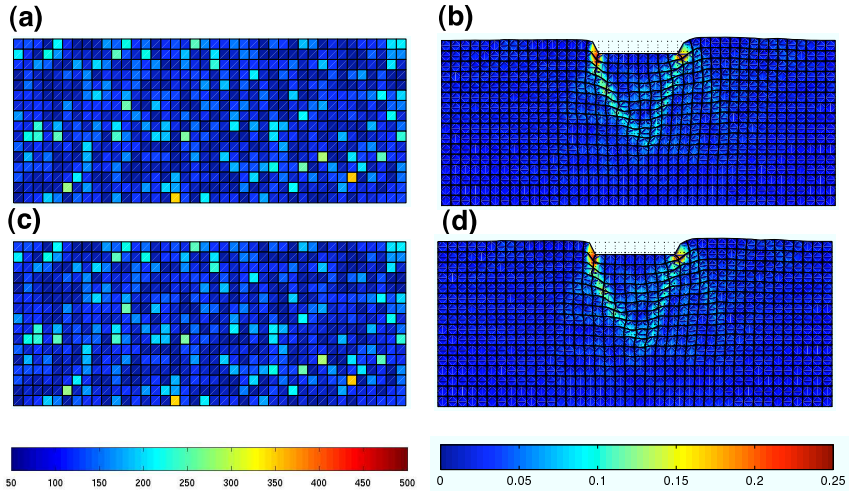

Figure 3.18. Comparison between coarse-scale and multi-scale random fields on failure surface for $a/L_1 = 0.5$ with ds=1: left column are initial shear strength fields and right column are shear strain contours at failure; (a) and (b) correspond to coarse scale; (c) and (d) correspond to multi-scale.

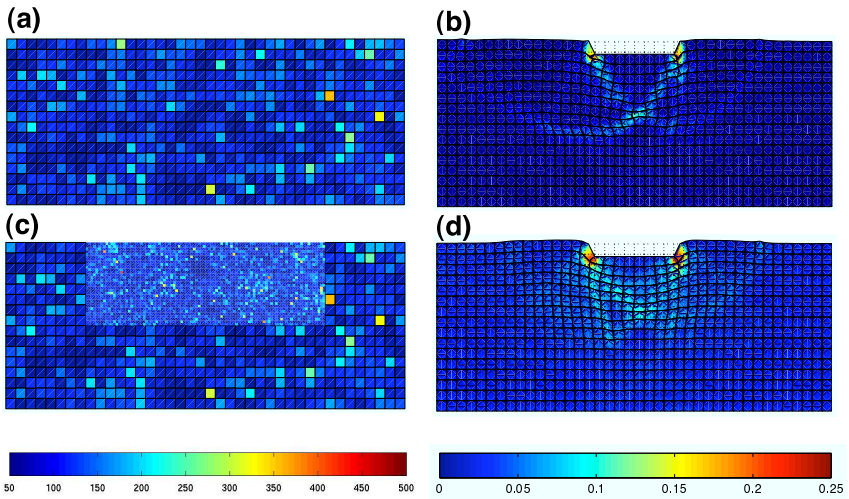

Figure 3.19. Comparison between coarse-scale and multi-scale random fields on failure surface for $a/L_1 = 0.5$ with ds=4: left column are initial shear strength fields and right column are shear strain contours at failure; (a) and (b) correspond to coarse scale; (c) and (d) correspond to multi-scale.

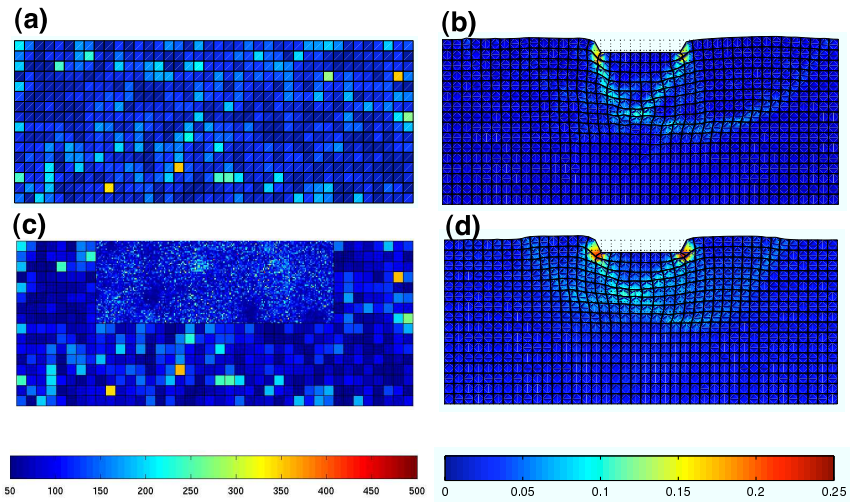

Figure 3.20. Comparison between coarse-scale and multi-scale random fields on failure surface for $a/L_1 = 0.5$ with ds=8: left column are initial shear strength fields and right column are shear strain contours at failure; (a) and (b) correspond to coarse scale; (c) and (d) correspond to multi-scale.

3.5.3. Influence of multi-scale random fields on settlement

In this section, the influence of multi-scale random fields on settlement is analyzed. For this purpose, the Young's modulus E is treated as the random variable while ν and S_u are held constant. Material parameters for generating lognormally distributed Young's modulus fields are the mean $\mu = 100$ MPa, which is equal to the values used in the deterministic study, and standard deviation $\sigma = 50$ MPa, which gives a COV value of 0.5. Three correlation length parameters (normalized) $a/L_1 = 0.5$, 1.0 and 2.0 are used. The process for generating random fields, the definition of degree of discretization and the notation for results are exactly the same as those used in bearing capacity analysis. We look at the variations in settlement at a pressure level of 300 kPa.

Typical realizations of initial Young's modulus fields for different degrees of discretization are shown in Figure 3.21 for $a/L_1 = 2.0$. Coarse-scale random fields are on the left column and corresponding multi-scale random fields are on the right column. The degree of discretization increases from top to bottom.

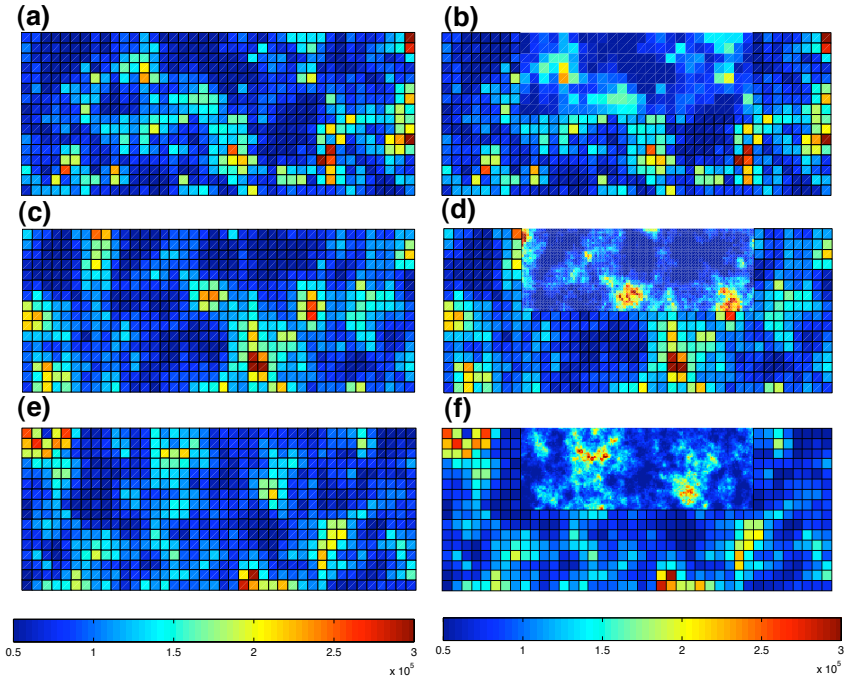

Figure 3.21. Initial Young's modulus fields for $a/L_1 = 2.0$ with different degree of discretization: from top to bottom: ds=1, 4 and 8 respectively with left column being coarse-scale random fields and right column being multi-scale random fields.

Figure 3.22 shows settlements versus a/L_1 for different degrees of discretization. The settlements are normalized by the width of the footing. Analogous to bearing capacity analysis, it can be seen that (1) for coarse-scale results with the same discretization level, the averaged settlement increases as a/L_1 increases; (2) for coarse-scale results with the same a/L_1, the averaged settlement decreases with increasing ds; (3) for ds=1, there is no difference between coarse-scale and multi-scale results as expected; (4) for ds=4 and 8

cases, higher levels of resolution are taken into account in multi-scale computations and the results show that the multi-scale random fields yield larger settlements on average for every value of a/L^1, which confirms that coarse-scale results are less conservative.

Remark 1. Sections 5.2 and 5.3 explore the effects of changing resolution for the specific examples presented in this paper. Generally, increasing number of fine-scale elements within a coarse-scale element will result in lower bearing capacity (in bearing capacity analysis) and higher settlement (in settlement analysis). In this formulation, the correlation length sets the macroscopic size of the elements. In essence, the element size should be such as to be able to resolve the gradients in the stochastic field. This is accounted for in our analysis. As for the effect of the RVE size, this formulation does not determine or sets the size of RVE, this is something would rather be problem dependent and determined by the correlation lengths and the deformation gradient in the problem. Interested readers may refer to [46] for discussions on selecting the size of the averaging window.

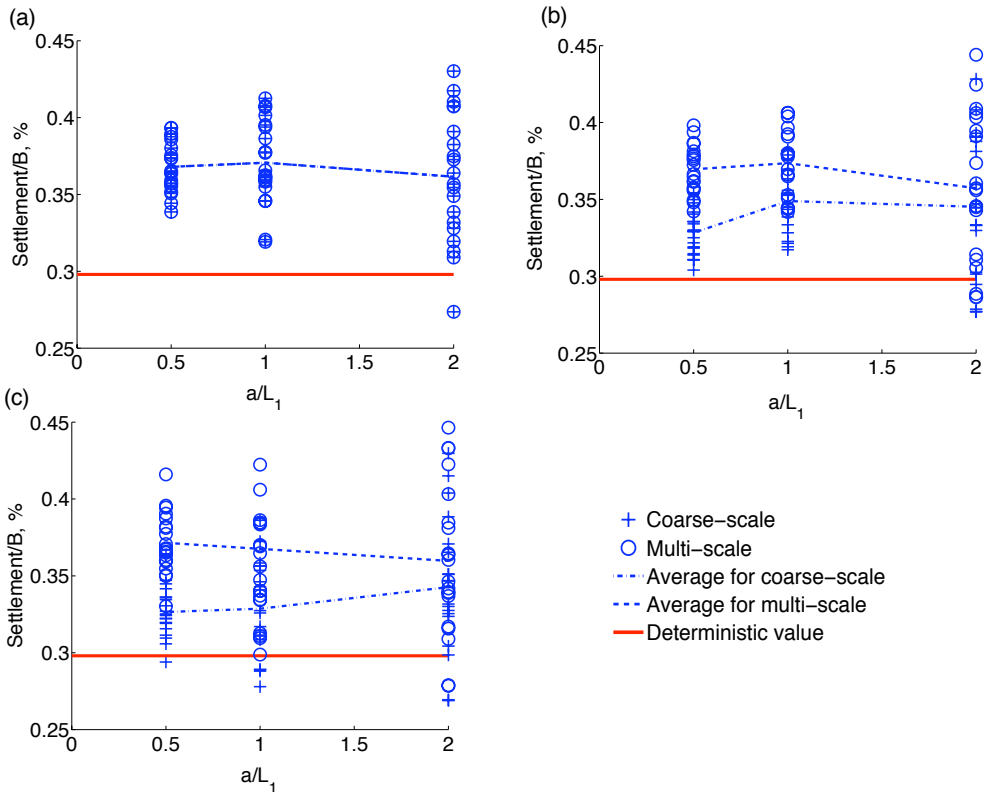

Figure 3.22. Settlements for different degrees of discretization: (a) ds=1, (b) ds=4 and (c) ds=8.

3.6. Conclusions

In this paper, we presented a novel method for characterizing multi-scale random fields. Cumulative density functions and spatial correlation for two soil properties of interest, undrained shear strength and Young's modulus, were described at the finest considered scale. The relationship between this scale and a coarser scale was defined and incorporated into a sequential simulation procedure. While two scales were presented here, including more by expanding the multi-scale definitions is straightforward, and there is no need to specify a number of scales in advance. Simulations begin at the coarse scale

and work toward higher resolution, but the results are indiscernable from starting at the fine scale and averaging those elements together. For convenience, a correlated standard Gaussian field was initially generated and then transformed to the target distribution via normal-score mapping.

We then proposed a framework for coupling the FEM with random fields at multiple scales. The formulation of the framework is based on the assumption that the strain and stress at an arbitrary material point in the coarse-scale domain are the volume average of the strain and stress fields over the fine scale domain, respectively. The framework consists of an element-splitting technique and a concurrent information-passing scheme. A selective refining strategy was used so that resolution is only increased where necessary.

A total of 720 simulations were performed. Among them, half utilized the proposed multi-scale framework and the other half utilized coarse-scale random fields for comparison purposes. Bearing capacity and settlement analyses were performed using the undrained shear strength and the Young's modulus as the random variable, respectively. It was shown that material property fluctuations, in general, will result in lower bearing capacities, unsymmetrical failure surfaces and larger settlements. More importantly, multi-scale results showed that higher levels of resolution result in lower bearing capacities and larger settlements. Or in other words, coarse-scale results are generally less conservative. These results show how the mechanics of the geosystem is influenced by multi-scale random fields and the importance of accounting for material inhomogeneities at different scales.

Acknowledgments

Support for this work is provided by NSF grant numbers CMMI 0726908 and CMMI 0727121. This support is gratefully appreciated. Any opinions, findings and conclusions or recommendations expressed in this material are those of the authors and do not necessarily reflect the views of the National Science Foundation.

CHAPTER 4

From continuum scales to granular scale: a semi-implicit return mapping algorithm for multiscale plasticity

This Chapter is published in: X. Tu, J.E. Andrade and Q. Chen. Return mapping for nonsmooth and multiscale elastoplasticity. *Computer Methods in Applied Mechanics and Engineering*, 18:2286–2296, 2009.

Abstract

We present a semi-implicit return mapping algorithm for integrating generic non-smooth elastoplastic models. The semi-implicit nature of the algorithm stems from 'freezing' the plastic internal variables at their previous state, followed by implicitly integrating the stresses and plastic multiplier. The plastic internal variables are incrementally updated once convergence is achieved (*a posteriori*). Locally, the algorithm behaves as a classic return mapping for perfect plasticity and, hence, inherits the stability of implicit integrators. However, it differs from purely implicit integrators by keeping the plastic internal variables locally constant. This feature affords the method the ability to integrate nonsmooth (C_0) evolution laws that may not be integrable using implicit methods. As a result, we propose and use the algorithm as the backbone of a semi-concurrent multiscale framework, in which nonsmooth constitutive relationships can be directly extracted from the underlying micromechanical processes and faithfully incorporated into elastoplastic continuum models. Though accuracy of the proposed algorithm is step size-dependent,

its simplicity and its remarkable ability to handle nonsmooth relations make the method promising and computationally appealing.

4.1. Introduction

Elastoplasticity is perhaps the most widely utilized and reliable framework used to capture material nonlinearities and inelastic behavior [47]. From metals to composites to aggregates, most solids can be simulated using elastoplastic models. Furthermore, many elastoplastic models make use of nonsmooth functions (in general, C_0 functions) to either represent yield surfaces e.g., [48, 49, 50] or hardening (evolution) laws e.g., [51, 52]. In the case of cohesive-frictional materials, C_0 yield surfaces have been proposed to model two salient properties. On the one hand, the yield surface is generally dependent on the third invariant of stress. Using multiple smooth functions to describe the third invariant dependency [48, 53] constituted one major source for nonsmoothness. On the other hand, cohesive-frictional materials feature very distinct responses under deviatoric and volumetric stresses. These two features have been accounted for by proposing models with two distinct yield surfaces, providing a potential source for discontinuities in the gradient function [49, 50, 9]. Nevertheless, the past decades have seen a great advance in the development of smooth yield surfaces aimed at capturing the behavior of complex geomaterials [54, 51, 55, 56, 57, 58]. Naturally, smooth plastic potentials can also be derived based on their similarity to the yield surfaces.

In contrast, C_0 functions are very much still used to describe the evolution of internal plastic variables via nonsmooth hardening laws. It is well-known that the evolution of

plastic internal variables (PIVs) is difficult to obtain and is mostly based on phenomenology. Hardening laws that conform well to experimental data may not necessarily yield smooth evolutions. Unsurprisingly, many nonsmooth hardening laws have been proposed to capture the behavior of complex elastoplastic materials accurately [**51**, **52**]. In this paper, we refer to a relation defining the variation of a PIV as an *evolution law*. Nonsmooth evolution laws permeate the plasticity literature. Accurately handling these C_0 evolution laws within a computational framework is not a trivial task and defines the objective of this work.

From a physics standpoint, one limitation of plasticity models emanates from the underlying phenomenology. On the one hand, plasticity relations, especially evolution laws, are determined from limited experiments or simply based on empirical intuition. On the other hand, a plasticity model only describes an average behavior at the macroscopic scale but fails to account for the underlying microscale mechanisms. In contrast, multiscale computational approaches can derive the constitutive relationship from a fundamental level 'on-the-fly' [**59**, **33**, **60**, **61**, **12**]. In particular, for granular matter this fundamental level corresponds to the grain scale, from which the micromechanical phenomena—including particle geometry, force chains, fabric arrangement—intrinsically govern the macroscopic response of the material. These grain-scale phenomena can be explicitly simulated using micromechanical models [**62**, **63**, **64**]. An alternative and recently proposed technique is to link micromechanical models with elastoplasticity using a multiscale framework [**12**]. The main idea is to replace phenomenological evolution laws with direct extraction of physically meaningful PIVs from the micromechanics. The resulting

micromechanically-based evolution of PIVs is nonsmooth and falls within the realm of C_0 evolution laws tackled in this work.

Among the few previous efforts to address nonsmooth elastoplasticity problems, the nonsmooth Newton method [65] is responsible for laying down an important theoretical foundation for integrating nonsmooth plasticity relations. However, as pointed out in [65], the derivation of the method relies on the assumption of J_2-plasticity and, hence, the applicability of this method to other type of plasticity models (e.g., pressure-dependent models) remains to be determined. There have been other semi-implicit algorithms proposed in the literature (see [66, 67] for example), but these have been aimed at explicitly integrating the hardening or evolution law and the flow rule, while the rest of the algorithm is fully implicit.

In this work, a simple semi-implicit algorithm is proposed to effectively combine the strengths of implicit and explicit architectures. On the one hand, implicit integration algorithms easily lose their advantages when integrating nonsmooth relations. On the other hand, though explicit algorithms have the ability of accommodating nonsmoothness, they may suffer shortcomings such as drifting and small critical time steps [67, 68]. Further, combining explicit stress integrators with implicit FE schemes may be problematic [69]. We unveil a semi-implicit algorithm that conserves all the features of the implicit schemes except for integration of the plastic internal variables. Specifically, the method 'freezes' the plastic internal variables (PIVs) incrementally. Hence, the method resembles implicit perfect plasticity integrators at the local level and therefore inherits unconditional stability. The PIVs are then updated *a posteriori* at every time increment. The combination of local freezing and the *a posteriori* update of PIVs affords the method the ability to

handle nonsmooth (C_0) evolution laws. It is also shown that incremental updating is efficient computationally and its application to recent multiscale techniques will be clearly demonstrated. The robustness and accuracy of the proposed algorithm is investigated using several numerical examples.

This paper is organized as follows. Section 2 summarizes the rate elastoplasticity formulation and presents the classic implicit return mapping scheme. In Section 3, the proposed semi-implicit algorithm is presented based on the implicit return mapping algorithm. Section 4 presents a detailed verification of the semi-implicit algorithm where we focus on boundary value problems to assess accuracy and robustness (convergence) of the algorithm against the backdrop of the fully implicit return mapping integrator. We conclude that the incrementally updated semi-implicit algorithm furnishes an appropriate balance between accuracy and robustness and, as a result, we utilize this method to perform proof-of-concept micromechanically-based semi-concurrent multiscale computations in Section 5. We summarize our findings and make some closing remarks in the last section.

As for notations and symbols used in this paper, bold-faced letters denote tensors or vectors; the symbol '$\cdot$' denotes an inner product of two vectors (e.g. $\boldsymbol{a} \cdot \boldsymbol{b} = a_i b_i$), or a single contraction of adjacent indices of two tensors (e.g. $\boldsymbol{c} \cdot \boldsymbol{d} = c_{ij} d_{jk}$); the symbol '$\otimes$' denotes a juxtaposition (e.g. $\boldsymbol{a} \otimes \boldsymbol{b} = a_i b_j$, or $\boldsymbol{\alpha} \otimes \boldsymbol{\beta} = \alpha_{ij} \beta_{kl}$); the symbol ':' denotes an inner product of two second-order tensors (e.g. $\boldsymbol{c} : \boldsymbol{d} = c_{ij} d_{ij}$); the symbol '$||\cdot||$' denotes an L_2 norm of a vector, e.g., $||\boldsymbol{e}|| = (\boldsymbol{e} \cdot \boldsymbol{e})^{1/2}$ or a tensor $\|\boldsymbol{A}\| = (\boldsymbol{A} : \boldsymbol{A})^{1/2}$. Stress and strain are expressed in Voigt notation, and as a result, the associated stiffness/compliance are expressed as matrices.

4.2. Infinitesimal elastoplasticity and implicit integrators

The most salient ingredients of the infinitesimal elastoplasticity theory are [13]:

- Additive decomposition of strain rate into elastic and plastic components, i.e., $\dot{\boldsymbol{\epsilon}} = \dot{\boldsymbol{\epsilon}}^{\mathrm{e}} + \dot{\boldsymbol{\epsilon}}^{\mathrm{p}}$.
- Generalized Hooke's law, i.e., $\dot{\boldsymbol{\sigma}} = \boldsymbol{c}^{\mathrm{e}} : \dot{\boldsymbol{\epsilon}}^{\mathrm{e}}$, where $\boldsymbol{c}^{\mathrm{e}}$ is the elastic constitutive tensor.
- Elastic domain and yield condition such that the yield surface $F = 0$ defines the limit of the elastic domain.
- Non-associative plastic flow rule, i.e., $\dot{\boldsymbol{\epsilon}}^{\mathrm{p}} = \dot{\lambda}\boldsymbol{g}$, where $\dot{\lambda} \geq 0$ is the consistency or optimality parameter and $\boldsymbol{g} := \partial G/\partial\boldsymbol{\sigma}$ is the direction of the plastic flow, where G is the plastic potential function.
- Evolution laws for the PIVs involved in F and G. In this paper, we use a vector $\boldsymbol{\alpha}$ to represent the set of PIVs. In classical infinitesimal elasoplasticity, the evolution relations for the PIVs are typically cast in rate-form, $\dot{\boldsymbol{\alpha}} = \dot{\lambda}\hat{\boldsymbol{\alpha}}(\boldsymbol{\sigma}, \boldsymbol{\alpha})$.
- The Kuhn-Tucker optimality condition, $\dot{\lambda}F = 0$, which induces the consistency requirement $\dot{\lambda}\dot{F} = 0$.

The aforementioned ingredients are the foundation for most plasticity models available, which are typically integrated numerically into a finite element (FE) or finite differences code. Numerical integration of these models is crucial for successful modeling of boundary value problems in engineering. A well-established integration technique is the implicit return mapping algorithm. A schematic showing the role of the implicit return mapping in the material subroutine inside a FE code is shown in Figure 4.1. As shown in this flowchart, the material subroutine is at the heart of the FE code and its main purpose

is to compute, given an increment in the strain $\Delta\boldsymbol{\epsilon}$, the resulting incremental change in state, i.e., $\Delta\boldsymbol{\sigma}$ and $\Delta\boldsymbol{\alpha}$. Here we use the incremental notation $\Delta\square := \square_{n+1} - \square_n$, where $\square_{n+1}$ corresponds to the value of the function evaluated at time station t_{n+1}. In addition, the material subroutine computes the consistent tangent algorithm defined as $\boldsymbol{c} = \partial\boldsymbol{\sigma}_{n+1}/\partial\boldsymbol{\epsilon}_{n+1}$. The consistent tangent is available in closed-form when implicit integrators are invoked and this is one of the reasons that make implicit algorithms appealing. Consistent tangent operators afford implicit nonlinear FE codes asymptotic rates of convergence, a key feature for efficient engineering analyses.

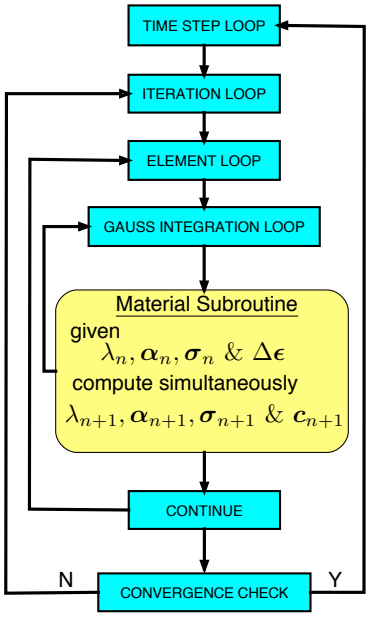

Figure 4.1. Flowchart for an implicit return mapping algorithm within an FE code.

Implicit return mappings rely heavily on Newton-Raphson schemes to iteratively arrive at a solution [70, 71, 57]. These schemes typically construct residual vectors $\boldsymbol{r}$ as a function of the unknowns $\boldsymbol{x}$, i.e.,

$$\boldsymbol{r}\left(\boldsymbol{x}\right) = \left\{ \begin{array}{c} \boldsymbol{c}^{\mathrm{e}\,-1} : \Delta\boldsymbol{\sigma} + \Delta\lambda G_{,\boldsymbol{\sigma}} - \Delta\boldsymbol{\epsilon} \\ \Delta\boldsymbol{\alpha} - \Delta\lambda\hat{\boldsymbol{\alpha}}(\boldsymbol{\sigma},\boldsymbol{\alpha}) \\ F(\boldsymbol{\sigma},\boldsymbol{\alpha}) \end{array} \right\}; \quad \boldsymbol{x} = \left\{ \begin{array}{c} \boldsymbol{\sigma} \\ \boldsymbol{\alpha} \\ \Delta\lambda \end{array} \right\} \tag{4.1}$$

where $\boldsymbol{c}^{\mathrm{e}}$ is the linear elastic stiffness matrix and $\Delta\lambda$ is the discrete consistency parameter. Solution to the local system of generally nonlinear equations is achieved when $\boldsymbol{r}\left(\boldsymbol{x}\right) = \mathbf{0}$ and the rate of convergence is intimately dependent on the consistent local tangent (Jacobian) such that

$$\boldsymbol{r}_{,\boldsymbol{x}} = \left[\begin{array}{ccc} \boldsymbol{c}^{\mathrm{e}\,-1} + \Delta\lambda G_{,\boldsymbol{\sigma}\boldsymbol{\sigma}} & \Delta\lambda G_{,\boldsymbol{\sigma}\boldsymbol{\alpha}} & G_{,\boldsymbol{\sigma}} \\ -\Delta\lambda\hat{\boldsymbol{\alpha}}_{,\boldsymbol{\sigma}} & \boldsymbol{\delta} - \Delta\lambda\hat{\boldsymbol{\alpha}}_{,\boldsymbol{\alpha}} & -\hat{\boldsymbol{\alpha}} \\ F_{,\boldsymbol{\sigma}} & F_{,\boldsymbol{\alpha}} & 0 \end{array} \right] \tag{4.2}$$

where $\boldsymbol{\delta}$ is the second-order identity tensor. The above Jacobian underscores the potential issues related to accommodating nonsmooth evolution laws $\hat{\boldsymbol{\alpha}}$ and $\hat{\boldsymbol{\beta}}$. If these functions are only C_0, the required derivatives appearing in the local Jacobian may not be continuous or may not even be defined. By way of example, we will show that this lack of continuity in the derivatives of the evolution laws could be detrimental in the convergence of the local integration algorithm and, as a result, that of the global computation. The next section describes a plausible alternative to fully implicit algorithms where the Jacobian matrix does not require evaluation of the derivatives of the evolution laws, making it possible to handle C_0 evolution functions.

Remark 2. If the formulation is isotropic, the yield surface F and plastic potential G can be expressed as a function of the stress invariants and the spectral decomposition can be exploited. These algorithms are efficient since they reduce the number of unknowns from full stress space to principal stress space. The interested reader is referred to [71] for an elaboration of this type of algorithms.

4.3. The semi-implicit return mapping algorithm

The implicit algorithm introduced in the foregoing section is a classic approach to integrate plasticity models. Under optimal conditions, this algorithm is able to achieve asymptotic quadratic convergence rates, first order accuracy, while featuring unconditional stability. However, in the presence of nonsmoothness, the implicit approach may not be suitable. As shown in equation (4.2), the local Jacobian, and hence the convergence of the algorithm, depend crucially on the computability of the necessary gradients. In the case of C_0 evolution laws, it is clear that convergence rates could be severely affected and the algorithm may diverge altogether. It is well known that the Newton-Rapson scheme will have serious issues converging near inflection points. Hence, it is often difficult, sometimes almost impossible, to use the conventional implicit method to integrate plasticity models with nonsmooth evolution relations (e.g., emanating from complex micromechanical substructures) [72, 68].

To ameliorate the shortcomings of fully implicit schemes in the context of C_0 evolution laws, we propose a simple semi-implicit scheme. The main procedure is simple and it involves freezing the plastic internal variables (PIVs) in the model at their previous, converged value. If the solution at time station t_{n+1} is being pursued, the PIVs in the

model are fixed at their value at time station t_n, or $\boldsymbol{\alpha}_n$ This strategy of freezing the PIVs is different from previous semi-implicit algorithms such as those presented in [66, 67], where the plastic flow and moduli are explicitly integrated.

A flowchart explicating the semi-implicit return mapping algorithm is given in Figure 4.2. Comparing the new semi-implicit scheme in Figure 4.2 with the fully implicit algorithm in Figure 4.1, it is clear that the material subroutine only updates the stresses $\boldsymbol{\sigma}$ and the plastic increment $\Delta\lambda$ at t_{n+1}, while keeping the PIVs fixed at their previous t_n value. Accordingly, the unknown vector $\boldsymbol{x}$ and the corresponding residual $\boldsymbol{r}$ read

$$\boldsymbol{x} = \left\{ \begin{array}{c} \boldsymbol{\sigma} \\ \Delta\lambda \end{array} \right\}, \quad \boldsymbol{r}(\boldsymbol{x}) = \left\{ \begin{array}{c} (\boldsymbol{c}^{\mathrm{e}})^{-1} \cdot \Delta\boldsymbol{\sigma} + \Delta\lambda G_{,\boldsymbol{\sigma}} - \Delta\boldsymbol{\epsilon} \\ F(\boldsymbol{\sigma}) \end{array} \right\} \tag{4.3}$$

Note the reduction in the number of unknowns and the resulting disappearance of the derivatives of the PIVs, cf., equation (4.2). In general, it is still necessary to invoke the Newton-Raphson locally to solve for $\boldsymbol{x}$. Hence, the local Jacobian is defined such that

$$\boldsymbol{r}_{,\boldsymbol{x}} = \left[\begin{array}{cc} \boldsymbol{a} & \boldsymbol{g} \\ \boldsymbol{f} & 0 \end{array} \right]; \quad \boldsymbol{a} := (\boldsymbol{c}^{\mathrm{e}})^{-1} + \Delta\lambda\boldsymbol{\Lambda}; \quad \boldsymbol{\Lambda} := G_{,\boldsymbol{\sigma}\boldsymbol{\sigma}}; \quad \boldsymbol{g} := G_{,\boldsymbol{\sigma}}; \quad \boldsymbol{f} := F_{,\boldsymbol{\sigma}} \tag{4.4}$$

The consistent tangent operator $\boldsymbol{c} = \partial\boldsymbol{\sigma}_{n+1}/\partial\boldsymbol{\epsilon}_{n+1}$ is obtained in the standard form, similar to the fully implicit algorithms, by exploiting the converged residual function [73, 74, 57], i.e.,

$$\boldsymbol{c} = \boldsymbol{a}^{-1} - \frac{1}{\bar{\chi}}\boldsymbol{a}^{-1} : \boldsymbol{g} \otimes \boldsymbol{f} : \boldsymbol{a}^{-1}; \qquad \bar{\chi} = \boldsymbol{g} : \boldsymbol{a}^{-1} : \boldsymbol{f} \tag{4.5}$$

where one can show that $\boldsymbol{c}$ corresponds to the upper fourth-order tensor of the inverse of the local jacobian $\boldsymbol{r}_{,\boldsymbol{x}}$. It is interesting to note the similarity between the consistent tangent and the continuum elastoplastic tangent for perfect plasticity, i.e.,

$$\boldsymbol{c}^{\mathrm{ep}} = \boldsymbol{c}^{\mathrm{e}} - \frac{1}{\chi}\boldsymbol{c}^{\mathrm{e}} : \boldsymbol{g} \otimes \boldsymbol{f} : \boldsymbol{c}^{\mathrm{e}}; \qquad \chi = \boldsymbol{g} : \boldsymbol{c}^{\mathrm{e}} : \boldsymbol{f} \tag{4.6}$$

For the case of a two-invariant model, such as Drucker-Prager, the above return mapping converges in one iteration and the state is obtained directly such that,

$$\boldsymbol{\sigma} = \boldsymbol{\sigma}^{\mathrm{tr}} - \Delta\lambda \boldsymbol{g}; \qquad \boldsymbol{\sigma}^{\mathrm{tr}} = \boldsymbol{\sigma}_n + \boldsymbol{c}^{\mathrm{e}} : \Delta\boldsymbol{\epsilon} \tag{4.7}$$

and

$$\Delta\lambda = \frac{F^{\mathrm{tr}}}{\chi}; \qquad F^{\mathrm{tr}} = F(\boldsymbol{\sigma}^{\mathrm{tr}}) \tag{4.8}$$

These equations of state for the stress $\boldsymbol{\sigma}$ and the plastic multiplier $\Delta\lambda$ are obtained departing from a trial state i.e., $\boldsymbol{\sigma} = \boldsymbol{\sigma}^{\mathrm{tr}}$ and $\Delta\lambda = 0$. The isotropy of the linear elastic model and the yield and plastic potential functions imply coaxiality, which affords the model constant gradients $\boldsymbol{f} = \boldsymbol{f}^{\mathrm{tr}}$ and $\boldsymbol{g} = \boldsymbol{g}^{\mathrm{tr}}$ in the Drucker-Prager model, where the trial gradients are simply the gradients of the yield function and plastic potential evaluated at the trial stress $\boldsymbol{\sigma}^{\mathrm{tr}}$. A geometrical interpretation for the algorithm in stress space is given in Figure 4.3. From this figure and from equations (4.7) and (4.8), it can be appreciated that the converged state is only a function of the trial state and therefore can be obtained without iterations. Finally, based on equation (4.7) a simplified closed-form

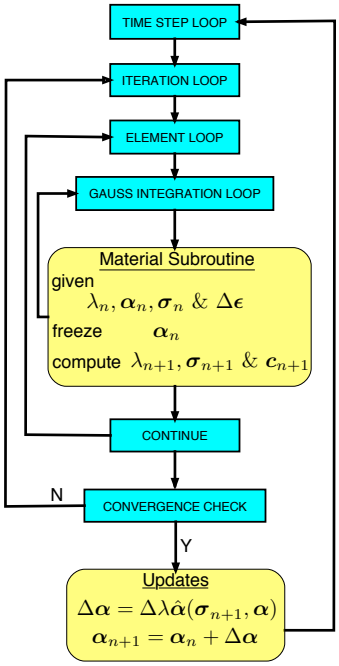

Figure 4.2. Flowchart for the semi-implicit return mapping algorithm within an FE code.

expression for the consistent tangent operator is obtained, i.e.,

$$\boldsymbol{c} = \underbrace{\boldsymbol{c}^{\mathrm{ep}}}_{\text{continuum tangent}} - \underbrace{\Delta\lambda \boldsymbol{c}^{\mathrm{e}} : \boldsymbol{\Lambda} : \boldsymbol{c}^{\mathrm{e}}}_{\text{algorithmic tangent}} \tag{4.9}$$

where one can observe the $O(\Delta\lambda)$ contribution from the algorithmic tangent.

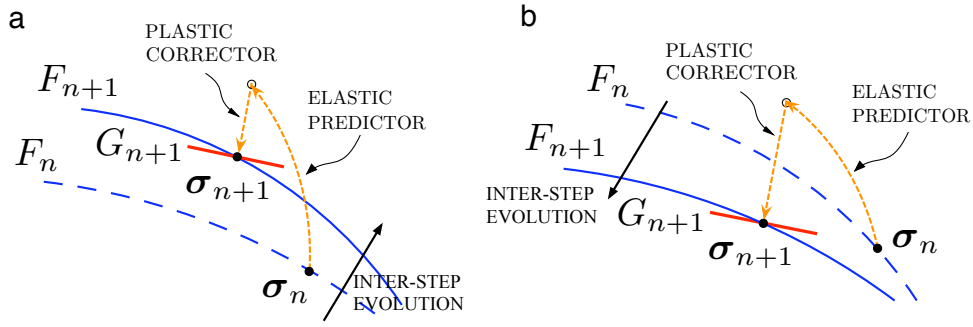

Figure 4.3. Two scenarios for the semi-implicit algorithm: (a) hardening and (b) softening.

Remark 3. The plastic internal variables (PIVs) are not updated until the global equation of motion have been satisfied at the global level. Figure 4.2 shows the updating procedure. In essence, the PIVs are direct functions of the converged values of stress $\boldsymbol{\sigma}$ and the plastic multiplier $\Delta\lambda$. These PIVs are used for the next time step calculation and kept frozen until the subsequent converged state is achieved.

To bypass potential problems with nonsmooth evolution (C_0) functions, the semi-explicit algorithm presented above, freezes the plastic internal variable at the previous time station. Hence, effectively behaving as a perfectly plastic material for a given time step. Similarly, truly explicit algorithms e.g., [**75, 76**] will also be able to bypass issues related to C_0 functions for the evolution laws. However, the explicit algorithms have two potential shortcomings. First, explicit algorithms generally need to be corrected to prevent yield surface from 'drifting', i.e., a violation of the consistency condition [**67, 68**]. Furthermore, an explicit stress integration is better employed within an explicit FE framework e.g., [**69**], as there is no closed-form solution for the consistent tangent operator. In fact, it has been shown that the derivation of such CTO can be quite tedious [**77**] and could necessitate numerical differentiation [**72, 78**], which is computationally expensive. In contrast, the semi-implicit algorithm presented above combines the advantages of implicit and explicit methods.

Remark 4. It can be seen that the main shortcoming of the semi-implicit method will be potential lack of accuracy stemming from the frozen plasticity. However, as Figures 4.2 and 4.3 show, the stress is corrected to enforce consistency, i.e., $F_{n+1} = F(\boldsymbol{\sigma}_{n+1}, \boldsymbol{\alpha}_n) = 0$, where the PIVs are frozen at their values at t_n. This inaccuracy should not be confused

with drifting, which is typically defined as $F_{n+1} \neq= 0$ in explicit schemes (see [67], pp. 277).

In this section, and without loss of generality, we apply the semi-implicit return mapping to a Morh-Coulomb-type model exemplified by the classic linear elastic-plastic Drucker-Prager model with nonlinear hardening/softening [4]. Naturally, we will demonstrate the robustness of the method within the context of C_0 evolution laws for the plastic internal variables involved. The elastic region of the model is furnished by the linear tangent such that

$$\boldsymbol{c}^{\mathrm{e}} = K\boldsymbol{\delta} \otimes \boldsymbol{\delta} + 2\mu \left(\boldsymbol{I} - \frac{1}{3}\boldsymbol{\delta} \otimes \boldsymbol{\delta} \right) \tag{4.10}$$

where K and μ are the constant elastic bulk and shear moduli, $\boldsymbol{\delta}$ is the second-order identity tensor and $\boldsymbol{I}$ is its fourth-order counterpart. Within this context, we can define two invariants of the stress tensor such that

$$p = \frac{1}{3}\operatorname{tr}\boldsymbol{\sigma}; \qquad q = \sqrt{\frac{3}{2}}\|\boldsymbol{s}\| \tag{4.11}$$

where $\operatorname{tr}\square = \square : \boldsymbol{\delta}$ is the trace operator, $\|\square\|$ is the L_2-norm, and $\boldsymbol{s} = \boldsymbol{\sigma} - p\boldsymbol{\delta}$ is the deviatoric component of the stress tensor. Similarly, the invariants of the strain rate tensor (total, elastic, or plastic) are defined as

$$\dot{\epsilon}_{\mathrm{v}} = \operatorname{tr}\dot{\boldsymbol{\epsilon}}; \qquad \dot{\epsilon}_{\mathrm{s}} = \sqrt{\frac{2}{3}}\|\dot{\boldsymbol{e}}\| \tag{4.12}$$

where $\dot{\boldsymbol{e}} = \dot{\boldsymbol{\epsilon}} - 1/3\dot{\epsilon}_{\mathrm{v}}\boldsymbol{\delta}$ is the deviatoric component of the strain tensor.

Using the aforementioned invariants of the stress tensor, we can define the yield surface and plastic potential for the Drucker-Prager (D-P) model:

$$F = q + \alpha p - c_{\mathrm{f}} \qquad G = q + \beta p - c_{\mathrm{q}} \tag{4.13}$$

Typically, the cohesion parameter $c_{\mathrm{f}} = 0$ for granular materials, while the cohesion-like parameter c_{q} is to be adjusted so that the potential surface G is always attached to the current stress point. Two evolution parameters are involved in the D-P model—the friction resistance α and the dilatancy parameter β. For $c_{\mathrm{f}} = 0$ (assumed henceforth) and at yielding, the friction parameter takes the form

$$\alpha = -\frac{q}{p} \tag{4.14}$$

Note that the only allowable states of stress when $c_f = 0$ are compressive, i.e., $p < 0$.The physical interpretation for the plastic internal variable α is that it directly represents the mobilized friction angle of the granular material. Hence, α indicates the mobilized friction resistance at any given state. Invoking the nonassociative flow rule, one can show that the volumetric and deviatoric invariants of the plastic strain rate tensor are defined by

$$\dot{\epsilon}_{\mathrm{v}}^{\mathrm{p}} = \dot{\lambda}\frac{\partial G}{\partial p}; \qquad \dot{\epsilon}_{\mathrm{s}}^{\mathrm{p}} = \dot{\lambda}\frac{\partial G}{\partial q} \tag{4.15}$$

For the D-P model presented here, it turns out that the dilatancy β takes the form

$$\beta = \frac{\dot{\epsilon}_{\mathrm{v}}^{\mathrm{p}}}{\dot{\epsilon}_{\mathrm{s}}^{\mathrm{p}}} \tag{4.16}$$

Similar to the friction coeficient α, the dilatancy β measures the change in volumetric plastic deformations for a given change in deviatoric plastic deformations. Reynolds in 1885 coined the term and pointed out its crucial role in the mechanical behavior of granular media [79]. Finally, the corresponding gradients to the yield surface and plastic potential are given such that

$$\begin{aligned} \boldsymbol{f} &= \frac{1}{3}\alpha\boldsymbol{\delta} + \sqrt{\frac{3}{2}}\hat{\boldsymbol{n}} \\ \boldsymbol{g} &= \frac{1}{3}\beta\boldsymbol{\delta} + \sqrt{\frac{3}{2}}\hat{\boldsymbol{n}} \end{aligned} \tag{4.17}$$

where $\hat{\boldsymbol{n}} = \boldsymbol{s}/\|\boldsymbol{s}\|$ is the unit deviatoric tensor. Due to coaxiality, it can be shown that the deviatoric unit tensor can be defined using the trial stress tensor, i.e., $\hat{\boldsymbol{n}} = \boldsymbol{s}^{\mathrm{tr}}/\|\boldsymbol{s}^{\mathrm{tr}}\|$ and, consequently, $\boldsymbol{f} = \boldsymbol{f}^{\mathrm{tr}}$ and $\boldsymbol{g} = \boldsymbol{g}^{\mathrm{tr}}$.

In what follows, different evolution laws for the PIVs α and β will be considered to evaluate the accuracy, stability, and efficiency of the proposed semi-implicit algorithm against the backdrop of its fully implicit counterpart.

4.3.1. Smooth evolution law

The accuracy, stability, and efficiency of the semi-implicit integration technique will be evaluated in this section. A smooth evolution law will be considered to provide both the semi-implicit and fully-implicit algorithms the same datum to make meaningful comparisons.

Consider the following smooth evolution laws for the friction and dilatancy parameters, respectively

$$\begin{aligned} \alpha &= a_0 + a_1 \lambda \exp\left(a_2 p - a_3 \lambda\right) \\ \beta &= \alpha - \beta_0 \end{aligned} \tag{4.18}$$

where a_0, a_1, a_2, a_3 and β_0 are (positive) material constants. It is clear that the evolution laws above are highly nonlinear and state-dependent (stress and cumulative plastic strain). Note that the friction resistance α and the dilatancy parameter β differ by a constant β_0, which is amenable to the stress-dilatancy relation widely observed in granular media [**80**, **81**, **12**]. The evolution laws defined above were introduced in [**71**] to test the robustness of fully-implicit return mapping algorithms. Similar to the values used in [**71**], we use $a_0 = 0.7$, $a_1 = 50$, $a_2 = 0.0005/\text{kPa}$, $a_3 = 50$ and $\beta_0 = 0.7$. For the elastic parameters, we use $E = 25000$ kPa and $\nu = 0.3$.

Here, we will perform plane strain compression 'experiments' under constant confinement. These experiments will furnish homogeneous BVPs that can be used to assess accuracy, stability and rate of convergence at the global level. The specimens are initially isotropically consolidated to a hydrostatic state of $p_0 = 50$ kPa. Subsequently, the specimens are sheared under constant lateral confining stress σ_3^* but increasing axial strain ϵ_1. The axial strain is increased by $\Delta\epsilon_1 = 0.3\%$ until the cumulative strain reaches about 10%. This situation allows us to define the global scalar residual function such that $R(\epsilon_3) = \sigma_3^* - \sigma_3(\epsilon_3)$, where we underscore the dependence of the residual function on the unknown lateral strain ϵ_3. Hence, the solution of the problem is $R = 0$ when we have found an appropriate ϵ_3 such that the calculated lateral stress σ_3 equals the prescribed

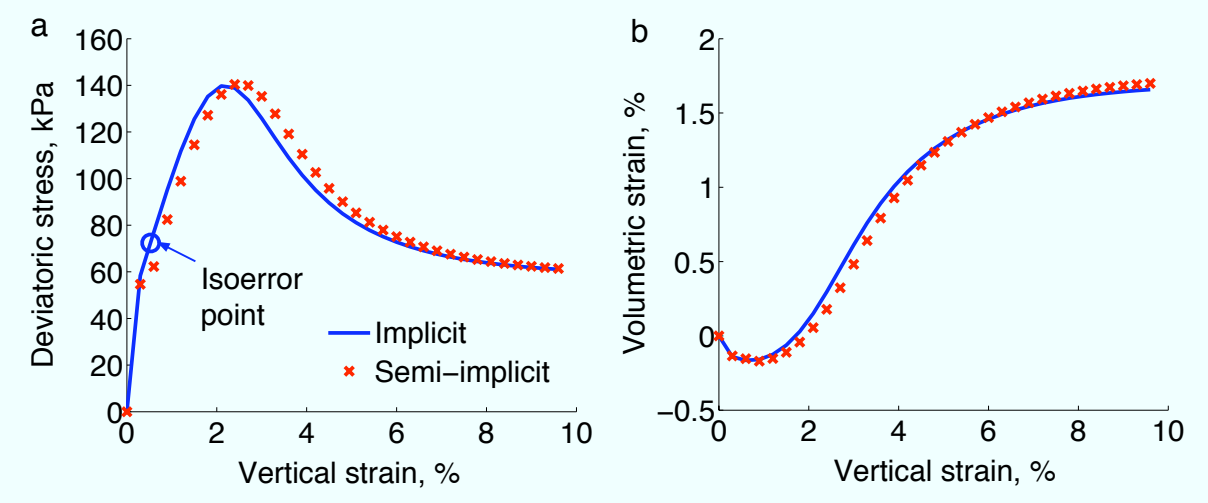

Figure 4.4. Integration of the smooth evolution relation under plane-strain compression: (a) stress response and (b) strain response.

lateral stress σ_3^*, for a given axial strain ϵ_1. The convergence criterion for the BVP is given such that

$$|R|/|R_0| < 10^{-10} \tag{4.19}$$

where R_0 is the initial residual.

Figure 4.4 shows the results of the experiments for both numerical integration techniques. It can be seen that both the stress-strain response and the volume-strain evolution are captured very well by the semi-implicit algorithm. The peak stress is captured correctly with a slight delay due to the PIVs lagging (freezing). Overall, we can conclude that the results for both algorithms are comparable. Similarly, it is important to compare the rate of convergence globally to obtain a sense of the efficiency of the method for implicit codes where the consistent tangent operator is needed. Figure 4.5 shows the semi-log plot of the normalized residual degradation curves in two typical load steps for each integration

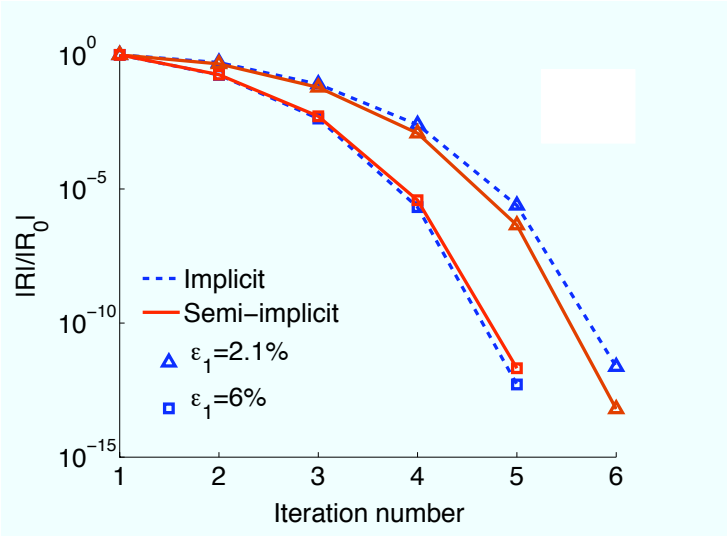

Figure 4.5. Residual degradation for plane strain problem with smooth evolution law.

algorithm. One convergence profile is reported pre-peak and the other post-peak. Clearly, the convergence rates of both algorithms are asymptotically quadratic. Convergence profiles at all other time steps are also asymptotically quadratic. These results suggest the semi-implicit algorithm is capable delivering the same advantage, as far as convergence is concerned, as its implicit counterpart.

Finally, to assess the accuracy of the scheme in a more quantitative fashion, isoerror analysis was performed. This numeric tool is typically employed to quantify the percent error of a solution compared to an 'exact' solution for one time step and under homogeneous conditions [**13**, **70**, **71**]. Figure 4.6 shows an isoerror map generated using various combinations of $(\Delta\epsilon_1, \Delta\epsilon_3)$. The semi-implicit algorithm was used in all computations, starting from the same "isoerror point" shown in Figure 4.4a ($\sigma_1 = -131.2$ kPa, $\sigma_2 = -83.0$ kPa, $\sigma_3 = -50.0$ kPa). Each computation of $(\Delta\epsilon_1, \Delta\epsilon_3)$ was first prescribed

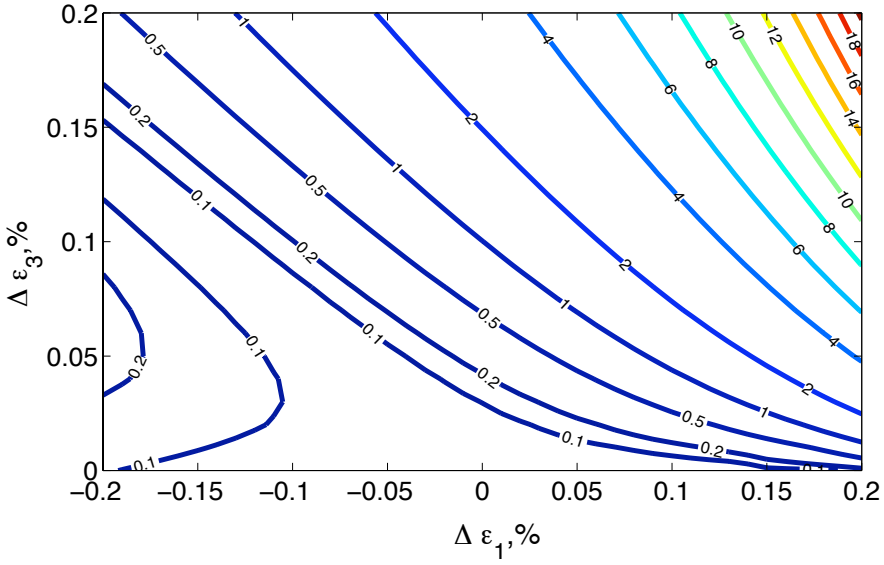

Figure 4.6. Isomaps for the semi-implicit algorithm relative to the 'exact' solution

in a single step, and the computed stress is denoted by $\boldsymbol{\sigma}$. Then, we calculated the 'exact' stress $\boldsymbol{\sigma}^*$ by subdividing the strain increment of $(\Delta\epsilon_1, \Delta\epsilon_3)$ until further refinement produces negligible changes in the resulting stress. The relative error was calculated from the equation

$$ERR := \frac{||\boldsymbol{\sigma} - \boldsymbol{\sigma}^*||}{||\boldsymbol{\sigma}^*||} \times 100 \tag{4.20}$$

The step-size dependent error is represented by the isolines in Figure 4.20, where negative strain increment is compressive. As expected, accuracy generally deteriorates as the strain increments increase. Nevertheless, increases of up to 0.1% in the strain increment, which is large, yield errors below 2%, which is generally acceptable.

These results suggest an equivalence between the semi-implicit and implicit return mappings under smooth conditions. Generally, implicit methods claim greater stability,

good accuracy and quadratic convergence profiles. This example has shown that the semi-implicit return mapping proposed can claim similar properties. In what follows, we will show a case where the semi-implicit algorithm performs much better than its implicit counterpart.

4.3.2. Nonsmooth (C_0) evolution law

In this section, the robustness of the semi-implicit method in handling C_0 evolution laws will be demonstrated by way of a numerical example. As mentioned earlier, the complexity of granular materials often requires the use of highly nonlinear and often empirical evolution laws for the plastic internal variables. It is not uncommon for evolution laws to contain ranges over which the evolutions are continuous but that introduce kinks at the intersections. One such evolution law was proposed by Lade to simulate the behavior of granular materials [**51**, **52**]. Consider the following evolution for the frictional resistance and dilatancy, respectively [**51**, **52**],

$$\alpha = \begin{cases} \beta_0 + h_1\lambda & \text{if} \quad \lambda \leq l \\ \beta_0 + h_1 l + h_2(\lambda - l) & \text{if} \quad \lambda > l \end{cases} \tag{4.21}$$

$$\beta = \alpha - \beta_0 \tag{4.22}$$

Figure 4.7 shows the plot of the evolution law proposed for α, labeled as 'imposed' since this function effectively imposes the allowable values for the stress ratio $-q/p$. From Figure 4.7 and equation (4.21), it can be observed that the evolution law for the friction parameter is bilinear, with a potential change in slope from h_1 to h_2 at $\lambda = l$. Hence, if

$h_1 \neq h_2$, as it is usually the case, the derivative function is discontinuous at $\lambda = l$. This discontinuity will make it difficult for fully implicit return mapping to converge.

For this example, we have chosen the following material parameters $\beta_0 = 0.7$, $h_1 = 20$, $h_2 = -20$ and $l = 0.09$. We perform axisymmetric compression simulations using the implicit return mapping and the semi-implicit algorithm within the context of the Drucker-Prager model presented above. The numerical example is started from a state of hydrostatic compression of $p_0 = 50$ kPa and then the confining stress is held constant with an increasing axial strain at a rate of $\Delta\epsilon_1 = 0.5\%$ in compression. Similar to the previous example, the axisymmetric compression simulation furnishes a BVP with mixed boundary conditions and a global residual where the confining stress is prescribed and must be matched by the computed lateral stress. Of course, the global convergence of the problem depends crucially on the local performance of the integration algorithm.

The results of the simulations are shown in Figure 4.7. Clearly, one measure of success, is for the computed stress ratio $-q/p$ to follow the 'imposed' evolution of α. Figure 4.7 shows that the semi-implicit algorithm is capable of reproducing the imposed evolution of the friction parameter α before and after the peak. On the other hand, the fully implicit algorithm runs into trouble near the peak, loosing convergence and producing spurious results. Part of the problem is explained by the global convergence profiles reported in Figure 4.8. It can be seen that both algorithms converge quadratically in the hardening regime. Near the peak, however, the implicit algorithm looses its convergence and finally diverges. In contrast, the convergence profile for the semi-implicit algorithm is undeterred even during the softening regime.

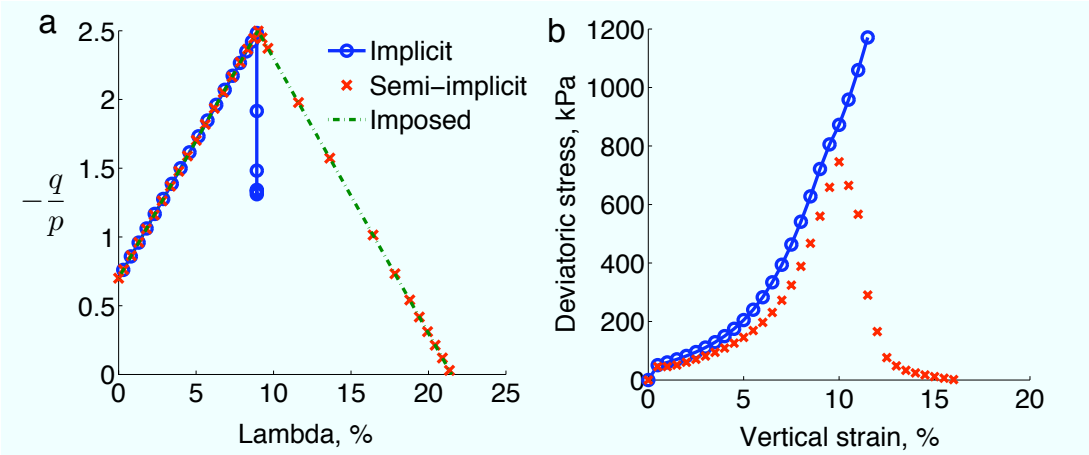

Figure 4.7. Integration of nonsmooth evolution law (a) friction evolution and (b) stress-strain curve.

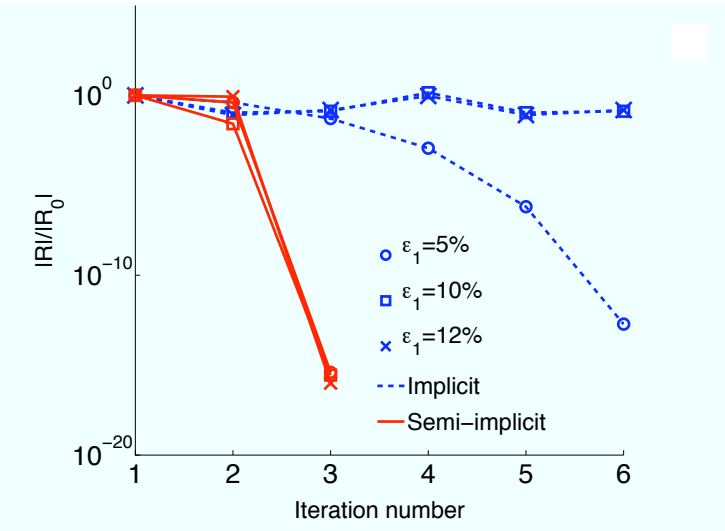

Figure 4.8. Convergence profile for nonsmooth evolution law at various time steps.

These results clearly show the ability of the semi-implicit method to efficiently handle C_0 functions describing the evolution laws necessitated to perform computations using elastoplastic models. Nevertheless, in the next section, a new class of nonsmooth evolutions for the PIVs will be introduced

4.4. Application to multiscale plasticity

In an effort to capture the micromechanical effects governing the behavior of granular media, macroscopic phenonmenological models have been introduced. These models have had relative success modeling the behavior of granular materials using plasticity theory and phenomenological evolution laws (e.g., the nonsmooth evolution shown in the previous example [51, 52]). However, it is now well accepted that these phenomenological laws break down outside of the realm of the boundary conditions used to develop them. For example, it is not uncommon for an evolution law to break down under plane strain if it was developed under axisymmetric conditions. For this reason, micromechanical models such as the discrete element method (DEM) [14] have been proposed. Unfortunately, micromechanical models such as DEM are very computationally intensive and will not be able to tackle engineering scale problems for the next 20 years [82]. Therefore, similar to Molecular Dynamics computations, these discrete methods have introduced a bottleneck in engineering computations, ameliorated by the advent of multiscale methods.

The key idea of multiscale methods is to retain high fidelity where necessary and use continuum (phenomenological) approximations elsewhere. In general, multiscale methods can be classified as either hierarchical or concurrent [60]. Hierarchical methods use information from the smaller scale as input to the relation for the larger scale. On the other hand, concurrent methods apply models at different scales to different domains and run them simultaneously. In an effort to capture the behavior of granular materials accurately while bypassing phenomenological evolution laws, Andrade and Tu have proposed a semi-concurrent multiscale method for updating Drucker-Prager-type models [12].

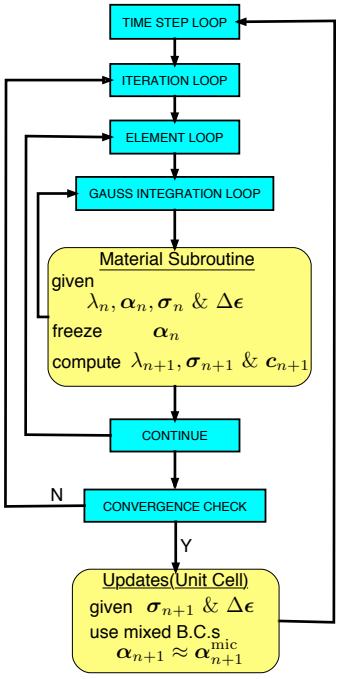

Figure 4.9. Flowchart for the hierarchical multiscale scheme.

The basic idea behind the semi-concurrent multiscale method is to link the granular scale and the continuum scale by extracting the evolution of the basic plastic variables α and β directly from the grain scale computations. Figure 4.9 shows the basic recipe for the method. Comparing Figures 4.9 and 4.2, one realizes that the algorithms are form-identical, with the only difference being that the update in the multiscale model is performed directly at the grainscale and then passed back to the continuum plasticity model. Hence, the semi-implicit algorithm presented herein is at the heart of the multiscale computational procedure proposed in [12].

4.4.1. Unit cell computations and PIV evolution

In the semi-concurrent multiscale scheme, and as shown in Figure 4.9, the update of the PIVs is performed at the so-called unit cell and then this continuum information is passed to the plasticity model e.g., [61]. The unit cell contains a certain physical volume of microstructure, from which continuum quantities (the critical parameters) are computed. A closely related concept is the so-called representative volume element (RVE), defined as the smallest possible region representative of the whole heterogeneous media, on average [83]. Unlike the RVE, the unit cell may not necessarily represent the behavior of the entire domain. However, similar to the RVE, the unit cell is a finite physical domain where a continuum description is applicable (high frequency oscillations are not present in a given continuum quantity, e.g., dilantancy). In a multiscale framework using FE, the unit cell can be selected to cover a representative area around a Gauss point, resembling the local Quasi-Continuum strategy [59]. In Figure 4.10a, for instance, the unit cell corresponds to the hatched area outlined by the so-called ghost nodes. Alternatively, the whole finite element can be taken as a unit cell, or the unit cell can be allowed to cover multiple elements, resembling the non-local Quasi-Continuum [59].

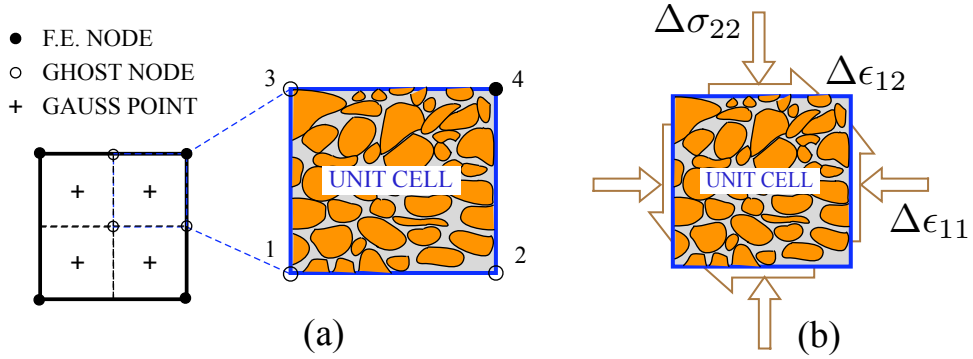

Figure 4.10. Unit cell computation: (a) domain, (b) mixed boundary condition.

The unit cell contains a configuration of the microstructure, associated with a specific Gauss point. The usefulness of the unit cell—furnishing the critical parameters necessitated by the macroscopic plasticity model—is realized through probing the microstructure in the *current* configuration. This probing imposes selected components from $\boldsymbol{\sigma}$ and $\Delta\boldsymbol{\epsilon}$ onto the boundary of the unit cell domain. As shown in Figure 4.9, the unit cell is invoked at the end of the current load step $n+1$. After the probing is completed, the resulting configuration of the microstructure is recorded, which will be used as the starting configuration, or the current configuration, for the next unit cell computation. More details about the multiscale procedure and the unit cell computation are given in [12] and are outside the scope of this paper.

The basic PIVs in the D-P model are realized by invoking their physical significance, i.e.,

$$\begin{aligned} \alpha^{\text{mic}} &= -\frac{q^{\text{mic}}}{p^{\text{mic}}} \\ \beta^{\text{mic}} &= \frac{\Delta\epsilon_{\text{v}}^{\text{mic}}}{\Delta\epsilon_{\text{s}}^{\text{mic}}} \end{aligned} \tag{4.23}$$

where the superscript 'mic' signifies that the quantity is computed from the micromechanical model as a means to distinguish it from its continuum counterpart. The micromechanical variables are then passed as approximations to the continuum plastic internal variables, i.e., $\alpha \approx \alpha^{\text{mic}}$ and $\beta \approx \beta^{\text{mic}}$. In the next section, explanation is given in terms of how to compute the stress and strain in a micromechanical model.

4.4.2. A representative example

To demonstrate the effectiveness of the semi-implicit algorithm in incorporating non-smooth micromechanical response into the multiscale scheme, we present the results of an axisymmetric compression computation on a granular assembly. We use DEM as the micromechnical model. To extract the stress tensor, equilibrium conditions for a particulate system can be invoked, yielding [84, 64],

$$\bar{\boldsymbol{\sigma}} = \frac{1}{V}\sum_{c=1}^{N_c} \boldsymbol{l}^c \otimes \boldsymbol{d}^c \tag{4.24}$$

where $\boldsymbol{l}^c$ represents the contact force at contact point c, $\boldsymbol{d}^c$ denotes the distance vector connecting the two neighboring particles, N_c is the total number of contacts in the particle assembly and V denotes the volume of the assembly, i.e., the volume of the unit cell domain associated with a specific Gauss point. To compute a homogenized strain tensor, the domain of the DEM-based unit cell can be partitioned into a series of polygonal subdomains, with the corners of each polygon being the centers of participating particles [85]. These polygons are deformed as the particle centers move, and the methods for computing these deformations are given in [86, 87]. Consequently, a homogenized strain tensor can be obtained by averaging these polygon-based deformations over the entire domain of the unit cell.

At the continuum level, the sample domain is discretized using one 8-node isoparametric 'brick' element. A single unit cell is used to contain the cubic assembly of 1800 polydisperse spherical particles, shown in Figure 4.11. Initially, the assembly was isotropically compressed to $p_0 = 5500$ kPa, with the initial configuration depicted in Figure 4.11.

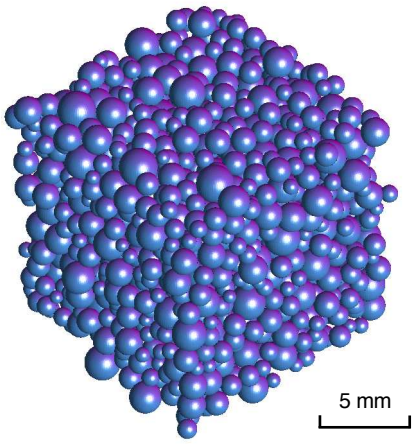

Figure 4.11. Initial configuration of the DEM-based unit cell.

The mixed boundary conditions of the unit cell include vertical strain control and horizontal stress control, consistent with the boundary conditions imposed on the finite element. A vertical strain increment $\Delta\epsilon_1 = 0.4\%$ was prescribed on the finite element. Putting the DEM model aside, the multiscale scheme involves only two parameters: $E = 5 \times 10^5$ kPa and $\nu = 0.25$. For comparison purposes, a direct numerical simulation (DNS) was performed on the same DEM assembly, with identical initial state and identical loading mode. The DNS results are regarded as the 'exact' solution against which the accuracy and performance of the multiscale scheme is evaluated.

Figure 4.12 shows the critical parameters (α^{mic} and β^{mic}) obtained from unit cell computation and the resulting friction resistance calculated using the multiscale method, i.e., $-q/p$. Figure 4.12b reports the evolution of the micromechanically-based dilatancy β^{mic}, which is later passed onto the macroscopic plasticity model. It is clear that the micromechanical relations for both parameters are nonsmooth, especially in the post-peak, finite deformation regime. These nonsmooth evolutions of α^{mic} and β^{mic} are recast

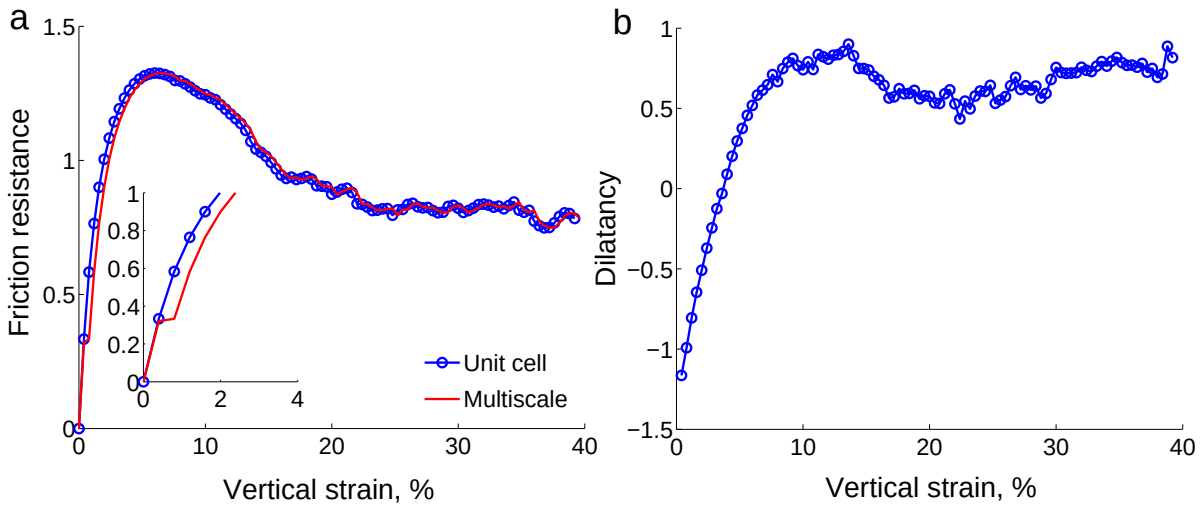

Figure 4.12. nonsmooth evolution of the critical parameters: (a) friction resistance obtained from unit cell vs. $-q/p$ computed by capsule model and (b) dilatancy parameter obtained from unit cell.

into the semi-implicit return mapping algorithm presented herein as nonsmooth evolution laws for the plastic internal variables α and β. However, these evolutions of the PIVs are not empirical and rather extracted on-the-fly from the actual microstructure. As shown in Figure 4.12a, the semi-implicit return mapping is able to reproduce the nonsmooth evolution of the frictional resistance parameter effectively and accurately.

Remark 5. In this paper, we use infinitesimal elastoplasticity as an example to demonstrate the effectiveness of the proposed algorithm. Extension to finite deformation plasticity is straightforward and will not incur any substantial change in algorithm. This has been done before in the context of implicit return mapping algorithms (see [74, 88]). We recognize the inaccuracy of the small deformation theory in representing the large deformations shown in the previous examples. However, these examples are not

shown to capture the physics of deformation per se but to demonstrate the effectiveness of the semi-implicit return mapping algorithm.

Figure 4.13 shows results obtained from the multiscale computation compared with those from the DNS. The accuracy of the multiscale method is measured here solely based on how closely it can reproduce the DNS results (verification). It can be seen that both the stress-strain response and the volumetric deformations are captured accurately by the multiscale model. This is remarkable in many levels, but most importantly due to the few parameters necessitated for the multiscale computation. The two elastic parameters are calibrated based on the initial response from the DNS and held constant for the duration of the simulation. Subsequently, the only parameters necessitated by the model are the frictional resistance and the dilatancy, which are allowed to evolve and extracted from the micromechanics. It is remarkable that such a simple model can capture the material response so closely. Finally, Figure 4.14 shows the global convergence rates for several different strain levels, highlighting the optimal convergence rate displayed by the algorithm. These results are very promising as they may open the door to more physics-based constitutive models to capture the mechanical behavior of granular media, without resorting to phenomenological evolution laws.

Remark 6. There is a noticeable shift in the responses obtained from the multiscale computation relative to the DNS. This finite gap occurs at the transition from pure elasticity to elastoplasticity and can be reduced by decreasing the time step. The shift is due to the semi-implicit return mapping freezing of the plastic internal variables involved in the multiscale computation.

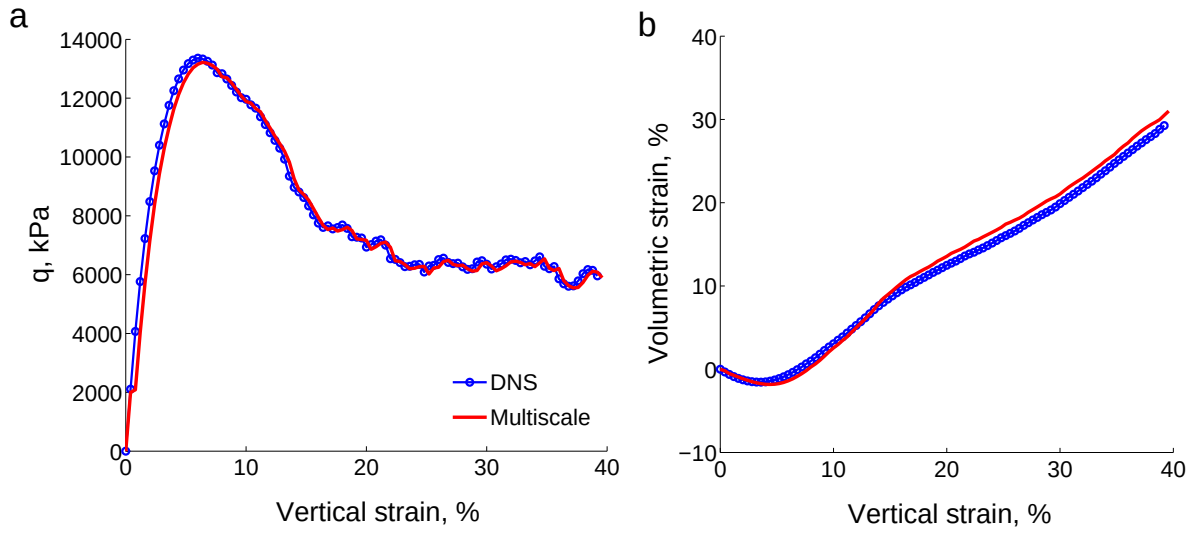

Figure 4.13. Comparison of multiscale and DNS results: (a) stress response and (b) strain response.

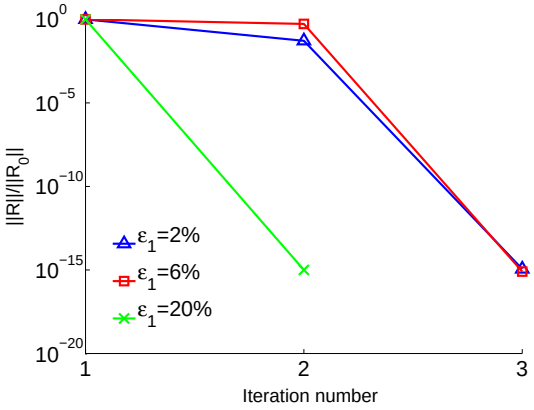

Figure 4.14. Convergence profiles at the finite element level for the multiscale simulation.

Remark 7. The unit cell, representing the granular assembly, requires a number of parameters to describe the micromechanical response accurately. For the DEM model, these parameters include particle geometry, grain stiffness, intergranular friction, etc. These parameters substantially determine how accurately the micromechanical model captures the true material behavior, which, however, is not the main focus of this paper. The goal of

the multiscale scheme is to faithfully reproduce the response of the underlying micromechanical model at the continuum scheme whatever that micromechanical model is. Hence, the multiscale method provides a bridge from the micro scale to the macroscale but it does not provide a micromechanical model. However, it is our believe that this multiscale technique will allow further development of accurate and physics-based micromechanical models in the near future.

Remark 8. There are two key items related to the success of the multiscale technique. The first one is the appropriate selection of the so-called critical parameters—those parameters that are passed back to the macroscopic model. How to select these parameters is key. In the case of granular materials under slow flow (quasi-static deformation) it appears as though the frictional resistance and the dilatancy are sufficient to describe the bulk of the material response. Hence, many models that encapsulate these mechanisms can be used in the multiscale framework. This has been demonstrated elsewhere [12]. The second crucial item is the appropriate selection of the size of the unit cell. In this work, we have not invoked any theoretical basis for the selection of the size, but rather have based our determination on the concept of the unit cell (and RVE for that matter), that it is the minimum size element where high oscillations in continuum properties can be filtered out.

4.5. Closure

We have presented a semi-implicit return mapping algorithm for integration of the stress response in elastoplastic models with nonsmooth (C_0) evolution laws. The algorithm owes its versatility to the notion of freezing the plastic internal variables and *a posteriori*

update of the PIVs. We have demonstrated that the semi-implicit algorithm displays some crucial qualities including good accuracy, stability, and the ability to calculate consistent tangent operators in closed-form, which result in global quadratic convergence. The simple algorithm was verified by way of numerical examples using empirically-based C_0 evolution laws as well as micromechanically-based evolutions of the critical variables. In both instances, it was demonstrated that the semi-implicit algorithm can handle nonsmooth evolutions accurately and efficiently. These features make the method promising and computationally appealing.

Acknowledgments

Support for this work was provided in part by NSF grant number CMMI-0726908 and AFOSR grant number FA9550-08-1-1092 to Northwestern University. This support is gratefully acknowledged. The DEM model used in the multiscale computation is a modification of *Oval*, an open source GNU software that was developed by Prof. Matthew R. Kuhn from the University of Portland.

CHAPTER 5

Multiscale localization modeling in granular media

This Chapter is published in: Q. Chen, J.E. Andrade and E. Samaniego. AES for multiscale localization modeling in granular media. *Computer Methods in Applied Mechanics and Engineering*, doi: 10.1016/j.cma.2011.04.022, 2011.

Abstract

This work presents a multiscale strong discontinuity approach to tackle key challenges in modeling localization behavior in granular media: accommodation of discontinuities in the kinematic fields, and direct linkage to the underlying grain-scale information. Assumed enhanced strain (AES) concepts are borrowed to enhance elements for post-localization analysis, but are reformulated within a recently-proposed hierarchical multiscale computational framework. Unlike classical AES methods, where material properties are usually constants or assumed to evolve with some arbitrary phenomenological laws, this framework provides a bridge to extract evolutions of key material parameters, such as friction and dilatancy, based on grain scale computational or experimental data. More importantly, the phenomenological softening modulus typically used in AES methods is no longer required. Numerical examples of plane strain compression tests are presented to illustrate the applicability of this method and to analyze its numerical performance.

5.1. Introduction

Failure in granular materials may present in various modes, such as diffuse, localized, etc. Many research efforts have been devoted to understand the failure phenomenon in granular materials (e.g., [89, 90]). Diffuse failure refers to failure modes with no strain localization pattern, see e.g., some recent work by [91] and [92], among others. In this paper, we are particularly interested in studying failure in the form of localized deformations, i.e., large strains occurring over a narrow zone. Macroscopic detection of localization phenomena is relatively well understood and its modeling has been cast within the finite element method, e.g., [10, 93, 94, 74, 95]. However, advancement of solutions beyond the localization point remains a challenge in computational mechanics. On the one hand, propagation of localization bands necessitates accommodation of discontinuities in some kinematical fields (e.g., displacements or strains) in a deforming body; on the other hand, the underlying grain structures and particle interactions, which are known to govern material responses at the macroscale, are yet to be taken into account when modeling localization behavior in granular materials. This latter point would allow for enhanced modeling capabilities and higher accuracy.

Regarding discontinuities in kinematical fields, there are usually two types identified in the literature [17]: weak discontinuities, which involve a discontinuous deformation gradient; and strong discontinuities, which involve a discontinuous displacement field. Classical approaches typically consider localization bands as weak discontinuities. However, due to the lack of an intrinsic characteristic length scale, classical rate-independent plasticity models have difficulties in resolving material behavior beyond localization and usually experience pathological mesh dependence [96, 67].

An alternative way for analyzing localization problem has been proposed in recent years and is predicated on the strong discontinuity concept, see for example [**97**, **98**, **99**, **17**, **18**, **100**, **101**, **102**, **103**, **104**], among others. Failure kinematics related to localization bands are approximated by means of discontinuous displacement fields embedded within the finite elements undergoing localization. Multiple approaches have been proposed for finite elements with embedded discontinuities, see [**105**, **106**, **107**] for comparative studies. Among them is the assumed enhanced strain (AES) concept, first proposed in [**21**] and which has been successfully used to capture the mechanism of deformations in strain localization problems.

An appealing feature of the AES method is that no additional global degrees of freedom are required since the enhancements for discontinuities are condensed out locally. Two algorithms are readily available in the literature for condensation: the first one is based on the standard static condensation technique, where the discontinuities of the deformation mapping are condensed out at the element level, see for example [**21**, **20**, **17**, **18**, **103**, **108**, **109**, **110**]; an alternative way was recently proposed in [**22**, **23**, **111**, **24**, **25**], where the parameters defining the displacement jump within the finite element are condensed out at the material point level and the standard Galerkin approximation is utilized. In this paper we adopt a material point level condensation, where the resulting set of linearized constitutive equations are formally identical to those of standard continuum models [**24**]. This is a great advantage from an implementation point of view, since it only requires minor modifications to the material subroutine in an existing standard finite element code.

A major drawback afflicting all current post localization models, including AES, is the lack of proper material description within the band. Most implementations use simple constitutive formulations with constant material parameters, such as, the friction coefficient. Moreover, some form of softening law, requiring softening moduli selected arbitrarily and *a priori*, is generally required. A recent work by [**112**], which incorporates a variable friction coefficient into the AES formulation, makes a clear attempt to address this issue.

To overcome this drawback, we exploit the multiscale nature of granular materials. Multiscale approaches have recently surfaced in granular mechanics. Among others, a recent work by [**113**] investigates the mechanical behavior of granular materials within a multiscale framework using an internally-consistent probabilistic model. The work in [**113**] bridges scales at continuum level, but has not yet explicitly linked the continuum scale with the grain scale, which is known to be the fundamental scale for granular materials. To this end, the discrete element method (DEM), proposed by [**14**], was developed to capture the behavior of granular materials at the fundamental scale. The method has also been extensively used in modeling localization band in granular media, see for example [**114**, **115**, **116**, **117**, **118**], among others. However, as pointed out in [**12**], DEM suffers two major shortcomings: expensive computational cost and inability to capture real grain shapes. To overcome the shortcomings of DEM and combine the strengths of available continuum and discrete models, we resort to a recently proposed multiscale computational framework in [**12**, **2**, **119**] for modeling granular materials. The key idea is to bypass the phenomenological evolutions of material parameters in the continuum model, e.g., friction and dilatancy, and rather extract such evolutions directly from grain-scale

structures and then upscale them into the continuum scale model. In this paper, we will reformulate the AES methodology within this multiscale computational framework, using a hierarchical information passing scheme. Following the taxonomy proposed by [16], hierarchical means that the two scales are not coupled directly, but rather finer scales provide data that can be used in a sequential way as the calculations are coarsened or upscaled. By doing so, the evolutions of material parameters in the AES method could be provided based on the grain scale information. More importantly, phenomenological softening moduli are no longer required.

The remainder of the paper is structured as follows: in Section 5.2, the kinematics induced by strong discontinuities and the constitutive equations of the AES method are briefly summarized; in Section 5.3, a hierarchical multiscale framework is first presented and the AES method is reformulated within the multiscale framework; in Section 5.4, two numerical examples are presented utilizing the multiscale framework to couple the AES with grain-scale computations and experiment data. Finally, we summarize our findings and make some concluding remarks in the conclusion section.

As for notations and symbols used in this paper, bold-faced letters denote tensors or vectors; the symbol '$\cdot$' denotes an inner product of two vectors (e.g. $\boldsymbol{a} \cdot \boldsymbol{b} = a_i b_i$), or a single contraction of adjacent indices of two tensors (e.g. $\boldsymbol{c} \cdot \boldsymbol{d} = c_{ij} d_{jk}$); the symbol '$\otimes$' denotes a juxtaposition (e.g. $\boldsymbol{a} \otimes \boldsymbol{b} = a_i b_j$, or $\boldsymbol{\alpha} \otimes \boldsymbol{\beta} = \alpha_{ij} \beta_{kl}$); the symbol ':' denotes an inner product of two second-order tensors (e.g. $\boldsymbol{c} : \boldsymbol{d} = c_{ij} d_{ij}$); the symbol '$||\cdot||$' denotes an L_2 norm of a vector, e.g., $||\boldsymbol{e}|| = (\boldsymbol{e} \cdot \boldsymbol{e})^{1/2}$ or a tensor $\|\boldsymbol{A}\| = (\boldsymbol{A} : \boldsymbol{A})^{1/2}$. Stress and strain are expressed in Voigt notation, and as a result, the associated stiffness/compliance are expressed as matrices.

5.2. Discontinuous kinematics and constitutive equations for the AES method

In this section, discontinuous kinematics and constitutive equations for the AES method are briefly summarized. As mentioned in the introduction, material point level condensation will be utilized. For more detailed formulations and development of this method, including its variational and matrix formulation, we refer the interested reader to [22, 23, 24].

5.2.1. Kinematics induced by strong discontinuities

The domain of interest here is a body Ω split by a surface of discontinuity $\mathcal{S}$. As usual, Γ_u and Γ_t furnish the essential and natural boundaries and $\boldsymbol{n}$ is the unit normal of the discontinuity surface, pointing towards Ω_+. An additional subdomain $\Omega^h \subset \Omega$ is defined by two arbitrary boundaries *ahead* ($\mathcal{S}^h_+$) and *behind* ($\mathcal{S}^h_-$) the discontinuity surface, and split by $\mathcal{S}$ into the subdomains Ω^h_+ and Ω^h_-. This subdomain defines the support of the ramp function in Eq. (5.1).

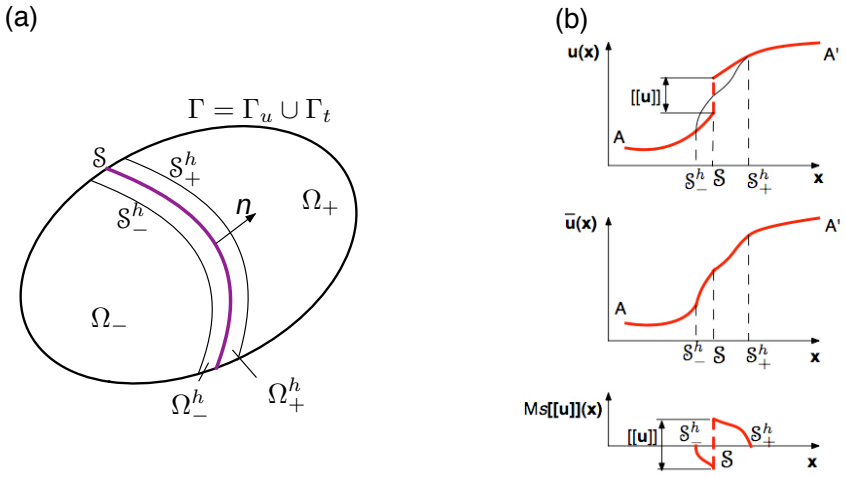

Figure 5.1. (a) Domain Ω with a surface of discontinuity $\mathcal{S}$; (b) One-dimensional representation of the decomposed displacement field.

The discontinuous displacement field can be decomposed into a continuous part and a discontinuous part as

$$\boldsymbol{u}(\boldsymbol{x}) = \underbrace{\bar{\boldsymbol{u}}(\boldsymbol{x})}_{\text{continuous}} + \underbrace{M_{\mathcal{S}}(\boldsymbol{x})[\![\boldsymbol{u}]\!](\boldsymbol{x})}_{\text{discontinuous}} \tag{5.1}$$

where $[\![\boldsymbol{u}]\!](\boldsymbol{x})$ is the displacement jump. The scalar function $M_{\mathcal{S}}(\boldsymbol{x})$ generates discontinuity on the surface $\mathcal{S}$ and is given by

$$M_{\mathcal{S}}(\boldsymbol{x}) = H_{\mathcal{S}}(\boldsymbol{x}) - f^h(\boldsymbol{x}), \text{ with supp}\,[\mathrm{M_S}] = \Omega_+^{\mathrm{h}} \cup \Omega_-^{\mathrm{h}} \tag{5.2}$$

where "supp" represents the support of a function. The Heaviside function $H_{\mathcal{S}}(\boldsymbol{x})$ is defined on $\mathcal{S}$ such that

$$H_{\mathcal{S}}(\boldsymbol{x}) = \begin{cases} 1 & \boldsymbol{x} \in \Omega_+ \\ 0 & \boldsymbol{x} \in \Omega_- \end{cases} \tag{5.3}$$

At the same rate, $f^h(\boldsymbol{x})$ is any arbitrary smooth function that satisfies the requirements

$$f^h(\boldsymbol{x}) = \begin{cases} 1 & \boldsymbol{x} \in \Omega_+ \backslash \Omega_+^h \\ 0 & \boldsymbol{x} \in \Omega_- \backslash \Omega_-^h \end{cases} \tag{5.4}$$

A one-dimensional representation of the decomposed displacement field is shown in Figure 5.1(b). Using such kinematic description of the displacement field, essential boundary conditions can be applied exclusively on $\bar{\boldsymbol{u}}(\boldsymbol{x})$. Therefore, it allows for the computed global nodal displacement $\bar{\boldsymbol{u}}(\boldsymbol{x})$ to be accepted as the final displacement field. The discontinuous part of the displacement field $[\![\boldsymbol{u}]\!]$ is condensed out at the material point level, leaving the global degrees of freedom unchanged.

In the AES concept, the enriched displacement field is modeled in an incompatible sense. It is acceptable to neglect the gradient of the displacement discontinuity, i.e., $\nabla^{\mathrm{s}}[\![\boldsymbol{u}]\!] = \boldsymbol{0}$. Then, for infinitesimal deformations, the total strain rate tensor is written as

$$\dot{\boldsymbol{\epsilon}} = \nabla^{\mathrm{s}}\dot{\boldsymbol{u}} = \nabla^{\mathrm{s}}\dot{\bar{\boldsymbol{u}}} - ([\![\dot{\boldsymbol{u}}]\!] \otimes \nabla f^h)^{\mathrm{s}} + \delta_{\mathcal{S}}([\![\dot{\boldsymbol{u}}]\!] \otimes \boldsymbol{n})^{\mathrm{s}} \tag{5.5}$$

where $\delta_{\mathcal{S}}$ is the Dirac delta function on the surface $\mathcal{S}$. It should be pointed out that it is a modeling assumption to neglect the gradient of the displacement jump, and that, in general, it is possible to allow variations in the displacement jump within one element, as for example in [**120**, **121**], where a linear interpolation for the displacement jump is used.

5.2.2. Constitutive equations for post-localization response

In this section, we will focus on the constitutive equations for post-localization response, since there is no difference between the constitutive framework used in the classical finite element method and the AES method at the pre-localization stage.

Once a material is localized, a post-localization model describing material response at the damaged state is invoked. In developing the constitutive equations, it is assumed that inelastic deformations induced by plasticity or material damage are restricted to the deformation band in question. A convex elastic domain $\tilde{E}$ is defined by a smooth yield function F, characterizing the yield condition on the band,

$$\tilde{E} = \left\{ (\boldsymbol{\sigma}, \boldsymbol{\alpha}) \in \mathbb{R}^{ndim} \mid F(\boldsymbol{\sigma}, \boldsymbol{\alpha}) \leq 0 \right\} \tag{5.6}$$

where $\boldsymbol{\alpha}$ is a stress-like vector of internal variables of dimension n. The yield function F can be different from its counterpart at the intact stage. In addition, a plastic potential function G can be defined. The model does not require an explicit form for this function, but some restrictions apply on G, as will be shown in Eq. (5.10).

Decomposing the displacement jump rate $[\![\dot{\boldsymbol{u}}]\!]$ into its magnitude $\dot{\xi}$ and direction vector $\boldsymbol{m}$ we obtain

$$[\![\dot{\boldsymbol{u}}]\!] = \dot{\xi}\boldsymbol{m} \tag{5.7}$$

from which expression the associated strain rate tensor emanates, cf., equation (5.1)

$$\dot{\boldsymbol{\epsilon}} = \nabla^{\mathrm{s}}\dot{\boldsymbol{u}} = \nabla^{\mathrm{s}}\dot{\bar{\boldsymbol{u}}} - \dot{\xi}(\boldsymbol{m} \otimes \nabla f^h)^{\mathrm{s}} + \dot{\xi}\delta_{\mathrm{s}}(\boldsymbol{m} \otimes \boldsymbol{n})^{\mathrm{s}} \tag{5.8}$$

Then, by subtracting the plastic part, we obtain the elastic strain rate tensor $\dot{\boldsymbol{\epsilon}}^e$

$$\dot{\boldsymbol{\epsilon}}^e = \nabla^{\mathrm{s}}\dot{\boldsymbol{u}} - \dot{\xi}(\boldsymbol{m}\otimes\nabla f^h)^{\mathrm{s}} + \dot{\xi}\delta_{\mathbb{S}}(\boldsymbol{m}\otimes\boldsymbol{n})^{\mathrm{s}} - \lambda_\delta\delta_{\mathbb{S}}\frac{\partial G}{\partial\boldsymbol{\sigma}} \tag{5.9}$$

where $\lambda = \lambda_\delta\delta_{\mathbb{S}}$ is the usual plastic consistency parameter.

The last two terms of (5.9) cancel because of the assumption that plasticity is localized to the discontinuity and hence the slip rate tensor $\dot{\xi}(\boldsymbol{m}\otimes\boldsymbol{n})^{\mathrm{s}}$ is fully plastic, which actually imposes a constraint on the plastic potential function G

$$\frac{\partial G}{\partial\boldsymbol{\sigma}} = \Lambda(\boldsymbol{m}\otimes\boldsymbol{n})^{\mathrm{s}},\ \Lambda = \frac{\dot{\xi}}{\lambda_\delta} \tag{5.10}$$

The Cauchy stress rate tensor is then computed as

$$\dot{\boldsymbol{\sigma}} = \boldsymbol{c}^E : \dot{\boldsymbol{\epsilon}}^e = \boldsymbol{c}^E : \left[\nabla^s\dot{\boldsymbol{u}} - \dot{\xi}(\boldsymbol{m}\otimes\nabla f^h)^s\right],\ \text{in } \Omega\setminus\mathcal{S} \tag{5.11}$$

where $\boldsymbol{c}^E$ is the elastic constitutive tensor. The constitutive equation resembles the predictor-corrector scheme of continuum plasticity, where $\dot{\xi}$ plays the role of the plastic consistency parameter. Yielding in the damaged state is described by the consistency condition on the band,

$$\dot{F} = \boldsymbol{\psi} : \dot{\boldsymbol{\sigma}} - \dot{\xi}\tilde{H}_\delta = 0,\ \boldsymbol{\psi} = \frac{\partial F}{\partial\boldsymbol{\sigma}} \tag{5.12}$$

where $\tilde{H}_\delta$ is the softening modulus on the band. Substituting equation (5.11) into (5.12) and solving for the jump rate $\dot{\xi}$,

$$\dot{\xi} = \frac{\boldsymbol{\psi} : \boldsymbol{c}^E : \dot{\tilde{\boldsymbol{\epsilon}}}}{\boldsymbol{\psi} : \boldsymbol{c}^E : (\boldsymbol{m} \otimes \nabla f^h)^s + \tilde{H}_\delta} \ , \ \dot{\tilde{\boldsymbol{\epsilon}}} = \nabla^s \dot{\tilde{\boldsymbol{u}}} \tag{5.13}$$

Then, the Cauchy stress rate tensor, at the post-localization stage, is written as

$$\dot{\boldsymbol{\sigma}} = \tilde{\boldsymbol{c}}^{EP} : \nabla^s \dot{\tilde{\boldsymbol{u}}} \tag{5.14}$$

where $\tilde{\boldsymbol{c}}^{EP}$ is the equivalent elastoplastic tangential modulus with the presence of displacement jumps and is given as

$$\tilde{\boldsymbol{c}}^{EP} = \boldsymbol{c}^E - \frac{\boldsymbol{c}^E : (\boldsymbol{m} \otimes \nabla f^h)^s \otimes \boldsymbol{\psi} : \boldsymbol{c}^E}{\boldsymbol{\psi} : \boldsymbol{c}^E : (\boldsymbol{m} \otimes \nabla f^h)^s + \tilde{H}_\delta} \tag{5.15}$$

The constitutive framework implied by the yield function F, plastic flow (eq. (5.10)) and the softening modulus H_δ plays a crucial role in the accuracy of the AES method. Currently, constant material properties are usually assumed *a priori* and selection of values is quite arbitrary. This is one of the major drawbacks of the AES method. To overcome this, we will resort to the multiscale nature of granular materials and linking the underlying grain-scale information with the continuum scale AES method.

5.3. AES for multiscale framework

In this section, the standard AES method will be reformulated within a recently-proposed multiscale framework for granular materials, see for example [12, 2, 119]. The most salient difference between the algorithm presented herein and that in the standard AES formulation is that the softening modulus H_δ is no longer required in the current

framework. Moreover, the evolutions of the plastic internal variables will be extracted from the grain-scale information, instead of assuming their values *a priori*.

5.3.1. Hierarchical multiscale framework

In this section, a hierarchical multiscale framework is presented to couple continuum-scale plasticity models with information extracted from grain-scale kinematics, e.g., DEM computations or physical experiments.

Continuum description considers the classical two-invariant Drucker-Prager (D-P) model, where the two stress invariants are given as

$$p = \frac{1}{3}\mathrm{tr}\boldsymbol{\sigma};\ q = \sqrt{\frac{3}{2}}\|\boldsymbol{s}\| \tag{5.16}$$

with $\mathrm{tr}\,\square = \square : \boldsymbol{\delta}$ as the trace operator, $\boldsymbol{s} = \boldsymbol{\sigma} - p\boldsymbol{\delta}$ as the deviatoric component of the stress tensor and $||\square||$ denotes the L_2 norm of $\square$. Similarly, the invariants of the strain rate tensor are defined as

$$\dot{\epsilon}_v = \mathrm{tr}\,\dot{\boldsymbol{\epsilon}};\ \dot{\epsilon}_s = \sqrt{\frac{2}{3}}\|\dot{\boldsymbol{e}}\| \tag{5.17}$$

where $\dot{\boldsymbol{e}} = \dot{\boldsymbol{\epsilon}} - 1/3\dot{\epsilon}_v\boldsymbol{\delta}$ is the deviatoric component of the strain rate tensor.

Using the aforementioned invariants of the stress tensor, the yield function F and the plastic potential function G for the D-P model at the pre-localization stage can be defined as

$$F(\boldsymbol{\sigma}, \mu) = q + \mu p - c_f = 0 \tag{5.18}$$

$$G(\boldsymbol{\sigma}, \beta) = q + \beta p - c_q \tag{5.19}$$

where the cohesion parameter $c_f = 0$ for granular materials and the cohesion-like parameter c_q ensures that the potential surface G is always attached to the current stress point. Two plastic internal variables are involved in the D-P model: the friction coefficient μ and the dilatancy parameter β. Physically, μ directly represents the mobilized friction angle of granular materials. At yielding, μ takes the form

$$\mu = -\frac{q}{p} \tag{5.20}$$

The dilatancy parameter β measures the change in volumetric plastic deformation for a given change in deviatoric plastic deformation. Specifically,

$$\beta = \frac{\dot{\epsilon}_v^p}{\dot{\epsilon}_s^p} \approx \frac{\dot{\epsilon}_v}{\dot{\epsilon}_s} \tag{5.21}$$

where, in approximation, the elastic strain increments are neglected. This is a plausible approximation once plasticity dominates the deformation, which is the case for most granular materials after yielding. It is important to clarify that equation (5.21) is only used to extract β from granular scale computations or observations. This assumption only affects the accuracy of extracted value from granular scale. In the continuum scale computation, we do not enforce this assumption. As can be seen from the examples presented herein, this method yields good accuracy relative to experiments and direct observations.

In our case, post-localization, the same form of the yield function as in equation (5.18) is used, but different yield functions can be chosen, if desired. As discussed in Section 5.2.2, a specific form of the plastic potential function is not required. Instead, the direction of the plastic flow is provided by

$$\frac{\partial G}{\partial \boldsymbol{\sigma}} \propto (\boldsymbol{m} \otimes \boldsymbol{n})^s \tag{5.22}$$

where the relation between $\boldsymbol{m}$ and $\boldsymbol{n}$ is shown in Figure 5.2. Furthermore, the jump's dilatancy angle ψ (see [110, 109] for a closer definition) controls the distance between $\boldsymbol{m}$ and the slip surface $\mathcal{S}$. The specific geometrical relation between $\boldsymbol{m}$ and $\boldsymbol{n}$ is given by

$$\boldsymbol{m} \cdot \boldsymbol{n} = \sin\psi \tag{5.23}$$

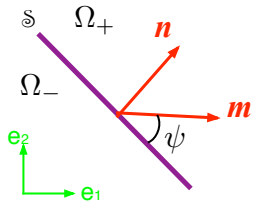

Figure 5.2. Relation between $\boldsymbol{m}$ and $\boldsymbol{n}$ relative to the discontinuity surface $\mathcal{S}$.

Remark 9. The procedure to evaluate $\boldsymbol{m}$ and $\boldsymbol{n}$, which are central to the AES formulation, deserves further explanation. In the numerical examples presented in this paper, the orientation of the shear band (e.g., given by $\boldsymbol{n}$) is readily available from DEM computations or experimental data by measuring the angle of the formed localization band. In this sense, the DEM is seen as a numerical experiment. Therefore, there are similarities between extracting shear band orientation and local information from DEM and from physical experiment. Also, for both physical experiment and the DEM simulation, we know exactly when the localization is triggered and the multiscale computation will read

localized data once the localization is reached. Alternatively, a more sophisticated pre-localization analysis of the acoustic tensor can be performed, signaling the onset of strain localization and providing the orientation of the band, see for example [**110**, **109**, **57**]. This latter analysis would be particularly useful when shear band information is not available or to make computations truly predictive. Here, we focus on post-bifurcation response and assume the orientation of the bands are known.

In standard AES, material properties, such as the aforementioned plastic internal variables, are usually assumed to be constant or to evolve with some arbitrary phenomenological relation. Moreover, an additional softening modulus H_δ is typically required so that the softening behavior after localization is captured. Within the multiscale framework, however, we exploit the physical significance of the plastic internal variables to extract them directly from grain-scale information available form DEM calculations or data from physical experiments.

In the case of DEM computations, the friction coefficient and dilatancy parameter are calculated based on average micro-mechanical stress and strain tensors [**84**, **122**, **63**]. Following the procedure presented in [**12**], μ and β are calculated as

$$\mu \simeq -\frac{\bar{q}}{\bar{p}};\ \beta \simeq \frac{\Delta\bar{\epsilon}_v}{\Delta\bar{\epsilon}_s} \tag{5.24}$$

where $\bar{\square}$ signifies micro-mechanically-based quantities; $\Delta\square = \square_{n+1} - \square_n$ represents the change of $\square$ from time t_n to t_{n+1}.

In the case of experiment-based computations, only dilatancy can be estimated directly. In the example presented herein, we use the data from [**15**], who measured the

change in volumetric and deviatoric strains, and related it to the angle of dilatancy as (cf. equation (6) in [15]),

$$\psi = \tan^{-1}\left(\frac{\Delta\epsilon_v}{\Delta\epsilon_s}\right) \tag{5.25}$$

and then β is directly related to the dilation angle via

$$\beta = \tan\psi \tag{5.26}$$

Remark 10. Recent advances in X-ray tomography and digital image correlation allow the kinematics of each grain to be captured throughout experiments and in real time, e.g., [123, 124]. In this case, the incremental strain field can be calculated using finite element interpolations and the incremental displacement data is obtained directly from experiments. Then, β is calculated from equation (5.24). This method is fully explored in a recent paper by [119].

Regarding the friction coefficient, since the micro-mechanical stress tensor is not readily available from experiments, one indirect way to estimate μ is to invoke a stress-dilatancy relation for granular materials [81]

$$\mu = \beta + \mu_{\text{cv}} \tag{5.27}$$

where μ_{cv} is a constant material parameter measuring the friction coefficient or stress ratio at critical state in a granular assembly.

Once evolutions of the plastic internal variables are fully defined, they will be used hierarchically as the calculations are coarsened or upscaled to the continuum scale. One

of the key features of this multiscale framework is that the plastic internal variables are "frozen" within each time step, and only updated when global convergence is achieved. Figure 5.3 shows the flow chart for the multiscale framework within a finite element program. Numerical implementation for pre-localization using conventional finite element method has been presented in recent publications by the authors [12, 2]. For post-localization analyses using the AES method, we will extend the previously-developed algorithms and present them in detail in the next section.

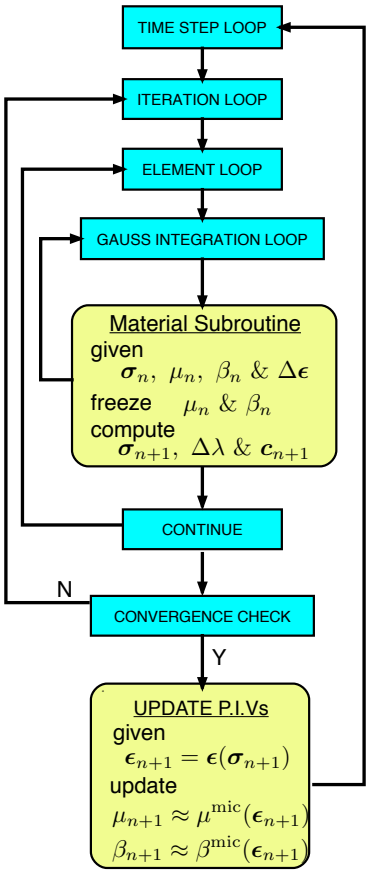

Figure 5.3. Flowchart for the hierarchical multiscale scheme, modified from [2].

In a nutshell, the hierarchical multiscale framework consists of the following key steps: (1) perform grain-scale computation using DEM, or obtain local measurement data from experiment; (2) extract evolutions of plastic internal variables from DEM using equation (5.24), or from experiments using either displacement field or measured dilatancy angle to obtain β, and use Eq. (5.27) to obtain μ; (3) use these evolutions of plastic internal variables as input for continuum scale computation using FEM, with localized elements enhanced through the AES technique.

Remark 11. One advantage of the aforementioned framework is that it provides insight into the granular scale information and a way to link it to continuum scale AES, wherever and whenever is necessary. This has not yet been taken into account by the standard AES. Also, a hierarchical multiscale framework has been presented in this section, but the framework could be extended to concurrent information passing schemes, as shown in [2]. This would allow AES to be linked with granular computation on the fly to achieve truly predictive capability .

5.3.2. Stress integration algorithm for AES within the multiscale framework

As shown in Figure 5.3, within each time step, the plastic internal variables are "frozen", and are only updated at global convergence. Therefore, the integration algorithm at each material point is analogous to that of a perfect plasticity model. Because of the delay in updating the plastic internal variables, the consistency condition (equation (5.12)) is no longer enforced when integrating stresses. Instead, the yielding condition $F_{n+1} = 0$ will be enforced.

To compute the stress state at time t_{n+1}, we will start with the rate form of the Cauchy stress. In AES formulation, the Cauchy stress rate is given as (cf. equation (5.11))

$$\dot{\boldsymbol{\sigma}} = \dot{\boldsymbol{\sigma}}^{\mathrm{tr}} - \dot{\xi}\boldsymbol{c}^{E} : (\boldsymbol{m} \otimes \nabla f^{h})^{s},\ \dot{\boldsymbol{\sigma}}^{\mathrm{tr}} = \boldsymbol{c}^{E} : \nabla^{s}\dot{\bar{\boldsymbol{u}}} \tag{5.28}$$

where $\dot{\boldsymbol{\sigma}}^{\mathrm{tr}}$ is the trial stress rate. Integrating equation (5.28) from t_n to t_{n+1}, we obtain

$$\boldsymbol{\sigma}_{n+1} = \boldsymbol{\sigma}^{\mathrm{tr}}_{n+1} - \Delta\xi\boldsymbol{c}^{E} : (\boldsymbol{m} \otimes \nabla f^{h})^{s} \tag{5.29}$$

where $\boldsymbol{\sigma}^{\mathrm{tr}}_{n+1}$ is the trial stress at time t_{n+1} and is written as

$$\boldsymbol{\sigma}^{\mathrm{tr}}_{n+1} = \boldsymbol{\sigma}_{n} + \boldsymbol{c}^{E} : \left(\nabla\bar{\boldsymbol{u}}^{h}_{n+1} - \nabla\bar{\boldsymbol{u}}^{h}_{n}\right)^{s} \tag{5.30}$$

As mentioned before, yielding condition on the band is enforced instead of the consistency condition, such that,

$$F_{n+1} = F(\boldsymbol{\sigma}_{n+1}, \mu_{n}) = 0 \tag{5.31}$$

Note that the plastic variable μ is held at its value at the previous time step t_n, resulting in a delayed update. The integration algorithm is based on finding the stress state $\boldsymbol{\sigma}_{n+1}$ so that equations (5.29) and (5.31) are satisfied. The algorithm is summarized in the following tables.

In table 5.1, the consistent tangent operator (CTO) $\boldsymbol{c}_{n+1}$ is needed in order to achieve optimal asymptotically quadratic convergences rate at the global level. For the stress

Table 5.1. Stress integration algorithm for the AES method within the multiscale framework

GIVEN: $\boldsymbol{\sigma}_n,\ \nabla\bar{\boldsymbol{u}}^h_{n+1},\ \nabla\bar{\boldsymbol{u}}^h_n,\ \nabla f^h,\ \boldsymbol{m}$ and μ_n.
FIND: $\boldsymbol{\sigma}_{n+1}$ and $\Delta\xi$ such that Eqs. (5.29) and (5.31) are satisfied.
STEP 1. Compute the trial stress state $\boldsymbol{\sigma}^{\text{tr}}_{n+1}$, and the yield function $F^{\text{tr}}(\boldsymbol{\sigma}^{\text{tr}}_{n+1}, \mu_n)$.
STEP 2. Check the yielding condition: $F^{\text{tr}}(\boldsymbol{\sigma}^{\text{tr}}_{n+1}, \mu_n) \leq 0$?
Yes, set $\boldsymbol{\sigma}_{n+1} = \boldsymbol{\sigma}^{\text{tr}}_{n+1}$ and exit.
STEP 3. No, initialize $\Delta\xi = 0$ and use Newton-Raphson to solve for $\Delta\xi$ (see table 5.2).
STEP 4. Update $\boldsymbol{\sigma}_{n+1} = \boldsymbol{\sigma}^{\text{tr}}_{n+1} - \Delta\xi \boldsymbol{c}^E : (\boldsymbol{m} \otimes \nabla f^h)^s$.
STEP 5. Compute the consistent tangent operator (CTO): $\boldsymbol{c}_{n+1} = \frac{\partial \boldsymbol{\sigma}_{n+1}}{\partial \nabla^s \bar{\boldsymbol{u}}^h_{n+1}}$ (see details below).

Table 5.2. Newton-Raphson loop to solve for $\Delta\xi$

STEP 1. Initialize the unknown $\Delta\xi^k = 0$ and set the iteration number $k = 0$.
STEP 2. Compute $\boldsymbol{\sigma}^k_{n+1} = \boldsymbol{\sigma}^{\text{tr}}_{n+1} - \Delta\xi^k \boldsymbol{c}^E : (\boldsymbol{m} \otimes \nabla f^h)^s$ and $F^k_{n+1}(\boldsymbol{\sigma}^k_{n+1}, \mu_n)$.
STEP 3. Check if the residual $r(\boldsymbol{\sigma}^k_{n+1}, \Delta\xi^k) = F^k_{n+1}(\boldsymbol{\sigma}^k_{n+1}, \mu_n) = 0$?
Yes, set $\Delta\xi = \Delta\xi^k$ and exit.
STEP 4. No, compute the local consistent tangent $r' = -\boldsymbol{b} : \boldsymbol{a}$
where $\boldsymbol{a} = -\frac{\partial \boldsymbol{\sigma}_{n+1}}{\partial \Delta\xi}$ and $\boldsymbol{b} = \frac{\partial F_{n+1}}{\partial \boldsymbol{\sigma}_{n+1}}$.
STEP 5. Update $\Delta\xi^{k+1} = -(r')^{-1} r + \Delta\xi^k,\ k = k + 1$ and go to STEP 2.

update presented in equation (5.29), the CTO can be computed as

$$\boldsymbol{c}_{n+1} = \frac{\partial \boldsymbol{\sigma}_{n+1}}{\partial \nabla^s \bar{\boldsymbol{u}}^h_{n+1}} = \boldsymbol{c}^E - \frac{\boldsymbol{a} \otimes \tilde{\boldsymbol{a}}}{\boldsymbol{b} : \boldsymbol{a}} \tag{5.32}$$

where

$$\boldsymbol{a} = -\frac{\partial \boldsymbol{\sigma}_{n+1}}{\partial \Delta\xi},\ \boldsymbol{b} = \frac{\partial F_{n+1}}{\partial \boldsymbol{\sigma}_{n+1}},\ \tilde{\boldsymbol{a}} = \boldsymbol{b} : \boldsymbol{c}^E \tag{5.33}$$

5.4. Numerical examples

In this section, we present two numerical examples to illustrate the applicability of the reformulated AES method within the hierarchical multiscale framework and to analyze its numerical performance. Both examples are plane strain compression tests. The first one utilizes DEM as the micromechanical model to extract evolutions of plastic internal variables, while the second one obtains such information directly from a well-instrumented physical experiment. In each example, different meshes are generated to demonstrate the objectivity of this framework with respect to mesh refinement and insensitivity to mesh alignment.

5.4.1. Coupling AES with DEM

In this example, a plane strain compression test coupling AES with DEM is presented. DEM is used as the microscale model to provide evolutions of the plastic internal variables. We chose two-dimensional (2D) DEM for its computational simplicity and efficiency. To this end, the stress and strain invariants given in equations (5.16) and (5.17) will be redefined for 2D cases.

The 2D DEM model consists of 2,520 disks, with the same radius of 0.05m. The dimensions of the sample are 0.31m by 0.62m. The sample is initially consolidated under stress controlled boundary conditions until $\sigma_a = \sigma_r = -100$ kPa, where σ_a and σ_r are the axial and lateral stresses. After consolidation stage, σ_r is held constant while the top platen moves vertically downward under prescribed incremental strain, with the bottom plate fixed. The loading continues after a localization band appears and stops when

critical state is apparently reached. The initial configuration and boundary conditions under plane strain loading for the DEM model are shown in Figure 5.4.

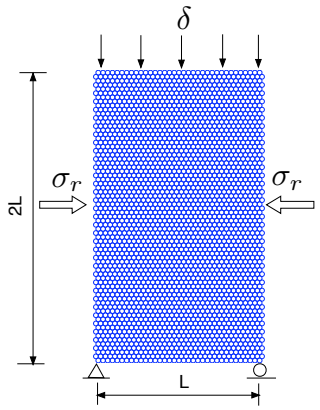

Figure 5.4. Initial configuration and boundary conditions under plane strain loading of the DEM model.

For 2D, we use the following definition for stress invariants, see also [125] for similar definitions for 2D biaxial test:

$$p = \sigma_r + \sigma_a;\ q = \sigma_r - \sigma_a \tag{5.34}$$

Similarly, for strain invariants

$$\epsilon_v = \epsilon_r + \epsilon_a;\ \epsilon_s = \epsilon_r - \epsilon_a \tag{5.35}$$

Using the 2D definitions of p and q in the D-P yield surface in equation (5.20) the friction coefficient takes the form

$$\mu = \frac{\sigma_r - \sigma_a}{\sigma_r + \sigma_a} = \sin\phi \tag{5.36}$$

where ϕ is called the friction angle, and it sets the angle of the failure envelope under Mohr-Coulomb failure criterion.

Figure 5.5 shows the global stress-strain behavior for this DEM simulation. The axial stress increases linearly with the axial strain up to 0.5%, where the stress reaches its peak value. Marked softening follows the peak. As will be seen later in the displacement field (see Figure 5.6), the initially homogeneous deformation breaks down at the peak stress, after which point the localization band starts to form. This band weakens the whole sample and contributes to the softening behavior seen in the axial stress. We will assume the sample undergoes elastic deformation up to 0.5% axial strain. Figure 5.5(b) shows that the volumetric strain decreases first (contracting behavior) and then increases (dilating behavior) until it approaches a plateau (critical state), as typically seen in a plane strain compression test in relatively dense granular materials. The particular shapes of stress strain response and the fact that peak stress not corresponding to the inflexion point of volumetric strain curve, are the results of the simplified DEM model we have chosen, i.e., equal radius disks arranged in a highly structured pattern. If a more sophisticated DEM is used, the behavior would be closer to that of real granular materials.

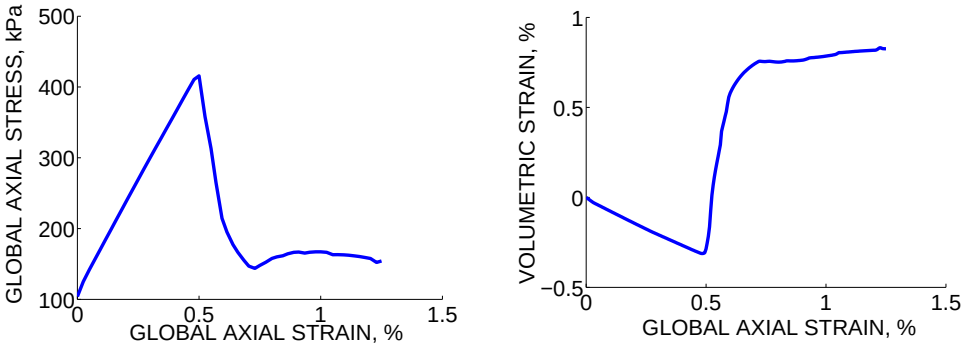

(a) (b)

Figure 5.5. Stress-strain behavior of the DEM simulation in plane strain compression test: (a) Axial stress vs. axial strain; (b) Volumetric strain vs. axial strain.

To pictorially show the mechanism of localization band formation in the DEM simulation, relative displacements at the center of the DEM disks are plotted at various stages of deformation in Figure 5.6. Here, relative displacements are computed as the difference between the current position particles and their values at the previous time step. In the figure, ϵ_a stands for axial strain. As seen in Figure 5.6, the sample deforms homogeneously up to the peak stress, where the axial strain level is about 0.5%. Then, a single localization band starts to form and breaks the homogeneous deformation. This single band persists throughout the simulation.

It is enlightening to compare the angle of the shear band obtained from the DEM simulation with those from analytical expressions. The DEM simulation results in a band of approximately 63° from the horizontal direction. If we adopt Mohr-Coulomb failure hypothesis, the failure plane would form an angle α_f from the plane of the major principal

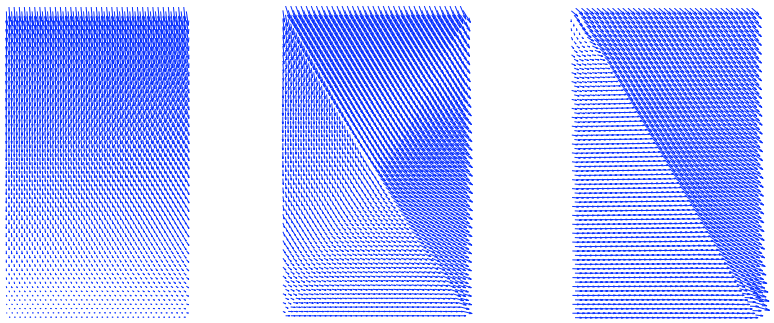

Figure 5.6. Relative displacement fields at different axial strain levels for the DEM simulation.

stress

$$\alpha_f = 45 + \frac{\phi}{2} \tag{5.37}$$

From equation (5.36), $\sin\phi = \mu \approx 0.56$, which gives $\phi \approx 34°$. Therefore, $\alpha_f \approx 62°$. Also, if we compute $\boldsymbol{n}$ based on localization analysis [93], we will obtain an angle of shear band of approximately 60°, which is fairly close to the DEM result.

As shown in section 5.3.1, friction and dilatancy can be calculated from DEM computation using equation (5.24), with definitions for stress and strain invariants in equations (5.34) and (5.35), and shown in Figure 5.7. Note that constant values are assumed for materials outside the band. This assumption will be immaterial because once localization happens, all materials outside of the localization band will unload elastically. Linear fits for both friction and dilatancy are used here for simplicity, but higher order interpolation functions could be incorporated easily.

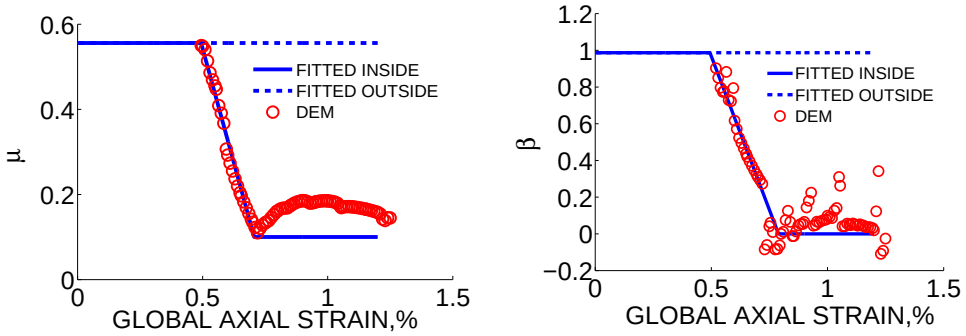

(a) Evolution of friction from DEM (b) Evolution of dilatancy from DEM

Figure 5.7. Evolutions of plastic internal variables from DEM computation.

The FE model is set up with the same sample dimension and boundary conditions. The material is described by a Drucker-Prager-type model, with evolutions of friction and dilatancy from Figure 5.7. Other material parameters used are two elastic constants: Young's modulus $E = 60$ MPa and Poisson's ratio $\nu = 0.3$, both computed based on the elastic portion of the stress-strain behavior from DEM simulations.

In the multiscale simulations, all elements are provided with the same evolution of friction and dilatancy up to 0.5% global axial strain. Once localization is reached at 0.5% axial strain, elements crossed by the localization band are equipped with enrichment furnished by the AES method. The evolution of the friction and dilatancy for those enhanced elements will be given by the solid line in Figure 5.7. Dashed line is used for regular elements outside the band.

To illustrate the mesh-insensitive nature of the method, two different meshes are used as shown in Figure 5.8. The dashed line is the potential localization band, as observed from DEM simulation. Figure 5.9 shows the comparison of the global stress-strain behavior for multiscale simulations and DEM results. Note that DEM is used as the benchmark for

verifying the performance of this multiscale framework. It can be seen that the multiscale model does a great job both pre- and post- localization. It captures the peak stress and the softening behavior very well. Also, it should be pointed out that two different finite element meshes produce identical results.

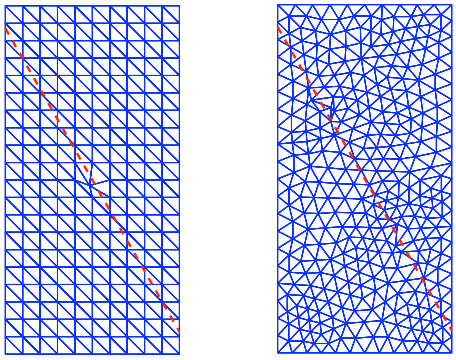

Figure 5.8. Meshes used in plane strain simulations coupled with DEM.

Remark 12. It should be pointed out that the discontinuity line observed in the DEM computation propagates across two off-diagonal corners. In the finite element mesh, the discontinuity is intentionally placed to avoid the corners. This is because, in the AES method, discontinuities propagating to essential boundaries will have difficulty converging. We did this by rotating the discontinuity line counter-clockwise so that there is at least one element between the discontinuity line and the essential boundary. In the current meshes shown, the discontinuity line is rotated about 3°. This angle could be reduced if finer meshes are used.

Deviatoric strain contours at 1% global axial strain are plotted for both meshes. As expected, the deviatoric strains are concentrated in the localization band. The sample

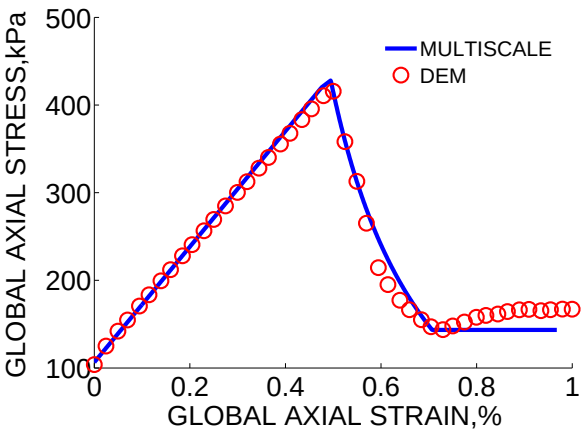

Figure 5.9. Comparison of global stress-strain behavior: multiscale vs. DEM.

essentially behaves like two rigid blocks sliding with respect to each other, which mimics what happens in the direct numerical simulation using DEM.

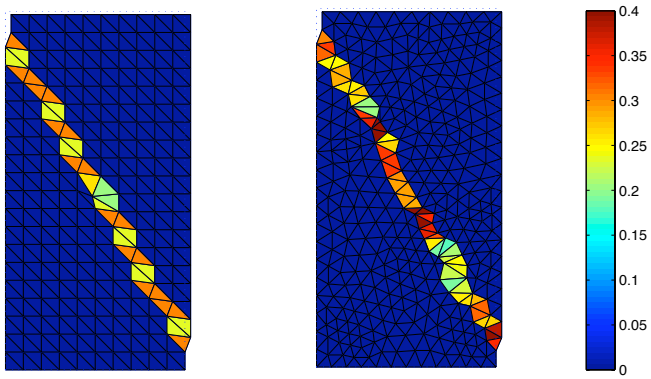

Figure 5.10. Deviatoric strain contour at 1% global axial strain.

Finally, the global convergence profiles at three different axial strain levels are plotted in Figure 5.11, where R is the global residual and R_0 is the value of R at the very

first iteration. It can be seen that the desired asymptotic quadratic convergence rate is achieved, demonstrating the efficiency of the proposed framework.

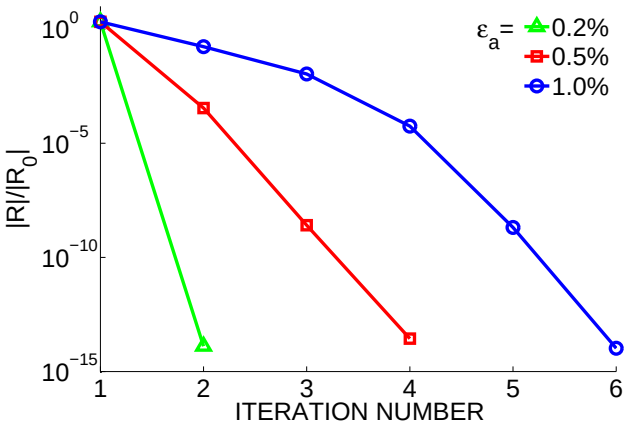

Figure 5.11. Global convergence profile at three different axial strain level.

5.4.2. Coupling AES with experiments

The previous example illustrates the coupling of AES with DEM within the multiscale framework. As will be seen in the second example, one of the most promising features of this multiscale framework is that it allows data from experimental measurements to be incorporated directly.

In this section, the behavior of a physical experiment of dense sand under drained plane strain compression is analyzed. The experiment was performed by [15] using a well-instrumented device. The sample dimensions are 140 x 40 x 80 mm. Plane strain is enforced by two rigid walls, in the 80 mm direction. The sample was initially consolidated anisotropically with axial stress $\sigma_a = -210$ kPa, and lateral stress $\sigma_r = -105$ kPa. After consolidation, lateral stress is kept constant while the top plate moves down under

displacement control. A localization band inclined at 63° from the horizontal axis was observed when the global axial strain reached about 3%. Dilation angle ψ within the band was extracted using stereophotogrammetry, shown as red circles in Figure 5.12.

In the numerical simulations, the material behavior is described by a Drucker-Prager model, same as in the first example. As discussed in Section 5.3.1, the dilatancy parameter β is related to the angle of dilatancy ψ by equation (5.26). Since there is no local measurement of either forces or stresses, the friction parameter μ can not be obtained directly from the experimental measurements. Instead, the stress-dilatancy relationship in (5.27) is used. In this study, $\mu_{\text{cv}} = 1.15$ is obtained from the experimental results.

In sum, material parameters input in the model are $E = 40,000$ kPa, $\nu = 0.2$, $\mu_{\text{cv}} = 1.15$, and β from Figure 5.12. Also, the orientation and location of the potential localization band are specified in the model based on experiment observations for the sake of simplicity.

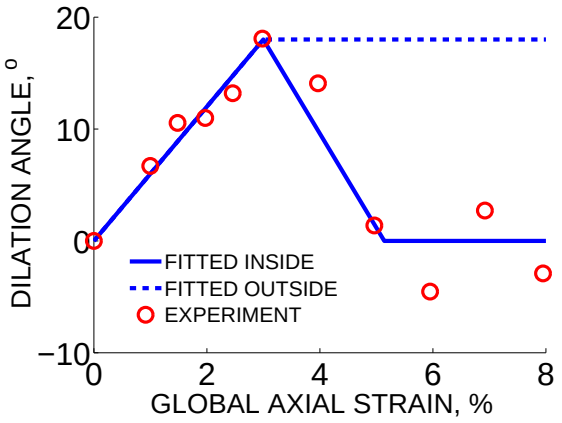

Figure 5.12. Evolution of dilation angle observed in the experiment.

Similar to the first example, all elements are provided with the same evolution of dilation angle up to 3% global axial strain. Once localization is reached, elements crossed

by the localization band will be equipped with enrichment using the AES concept. The evolution of the dilation angle for those enhanced elements will be given by the solid line in Figure 5.12. The dashed line on the figure represents elements outside the localization band. Since the sample unloads elastically outside the band, the assumption of a constant dilation angle will not affect the results. It should be pointed out the standard AES method would capture the behavior by fitting parameters. However, as mentioned in remark 3, the multiscale provides insight and a way to link the granular scale information for true predictiveness without phenomenology.

To illustrate the mesh-insensitive feature of the method, four different meshes are used as shown in Figure 5.13. The dashed line is the potential localization band, as observed in the experiment. Figure 5.14 shows the evolution of the stress ratio $-q/p$ for both simulation and experiment, where the values from the simulation correspond to the global averaged stresses. It is clear that the multiscale simulation captures the global stress response remarkably well. Also, four different meshes produce identical results. It should be clarified that in the example, the discontinuity orientation and placement are selected *a priori* and made to be the same for each mesh. When a propagation criterion is implemented, the results from different meshes may not be identical.

To show that the model can capture the deformation modes observed in the experiment, we compare the computed local lateral strain with the experiment data, as shown in Figure 5.15. "Upper" or "lower" means that the lateral strain was computed/measured above or below the localization band. From both simulation and experiment results, it can be seen that the mechanical behavior in the "upper" and "lower" block differ significantly. Once localization occurs, the upper part of the sample will slide, inducing large

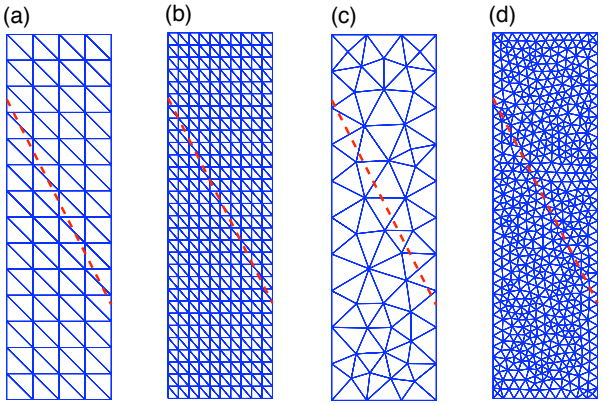

Figure 5.13. Meshes used in plane strain compression test coupled with experimental data.

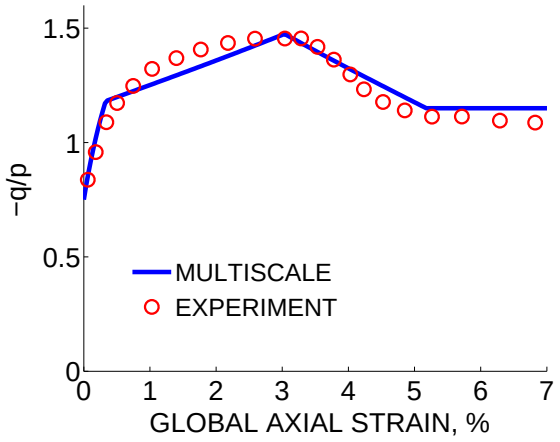

Figure 5.14. Evolution of stress ratio with global axial strain.

amount of lateral strain, while the lower part remains almost rigid and intact. Again, four meshes give identical results.

Remark 13. It should be pointed out that the strain level is higher than typical small strain assumption. However, in the experiment, the strains are actually computed by using small strain calculations. Therefore, the small strain formulation in the AES is consistent with the experiment. Also, the results by multiscale AES are not affected as

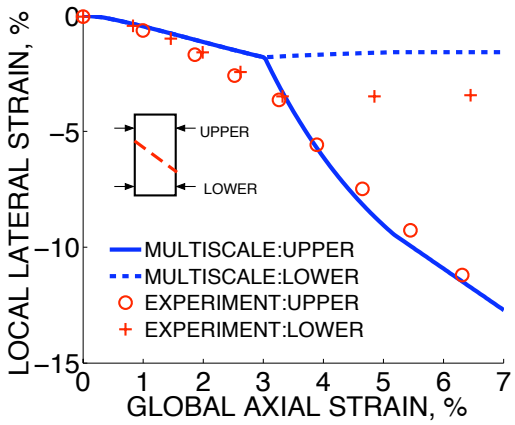

Figure 5.15. Lateral strain vs. axial strain.

much and match well with experiment data. Extension of the method to finite strains is currently under development.

The deformed meshes at 7% global axial strain are plotted in Figure 5.16. The modes of deformation for all meshes are practically identical and all meshes propagate successfully to the end of the simulation, demonstrating the applicability of the framework to incorporate experimental data directly. Finally, the deviatoric strain contour at 7% global axial strain is plotted for mesh 3. As expected, it is clear that the strains are concentrated in the localization band. The sample essentially unloads elastically outside the localization band.

5.5. Conclusions

We have presented a reformulated AES method within a hierarchical multiscale framework for modeling localization behavior in granular materials. A key feature of this framework is that, instead of constant or phenomenologically varied material properties typically used in standard AES methods, evolutions of material properties are extracted

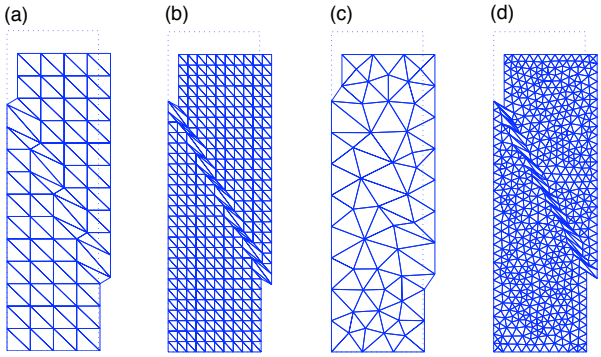

Figure 5.16. Deformed samples for plane strain simulations.

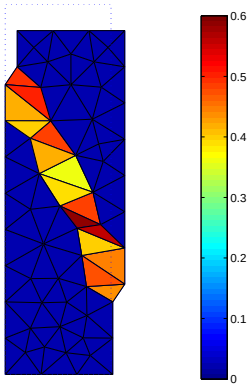

Figure 5.17. Deviatoric strain contour at 7% global axial strain for mesh 3.

from grain scale computations or experimental data and used as direct input for the underlying continuum model. More importantly, the softening modulus, which appears in standard AES formulations, is bypassed. The stress-point integration algorithm is similar to the classical elastic-perfectly plastic model, resulting in a simple yet powerful method. Numerical examples of two plane strain compression tests, coupling the AES method with DEM and experimental data, demonstrate the applicability of this method. The

mesh objectivity and numerical efficiency of this method are also shown in the numerical examples.

Acknowledgments

Support for this work is provided by AFOSR grant number FA9550-08-1-1092. This support is gratefully acknowledged. The DEM code used in this research is developed by Prof. Kuhn from University of Portland. The authors are grateful to Prof. Kuhn for making the source code available.

CHAPTER 6

Bridging solid-like and fluid-like behavior in dry dilative granular media

This Chapter will be published in: J.E. Andrade, Q. Chen, P.B.H. Le, C.F. Avila and M.T. Evans. On the rheology of dilative granular media: bridging solid and fluid-like behavior. *Journal of the Mechanics and Physics of Solids*, in review, 2011.

Abstract

A new rate-dependent plasticity model for dilative granular media is presented, aiming to bridge the hitherto seemingly disparate solid- and fluid-like behavioral regimes. Up to date, solid-like behavior is typically tackled with rate-independent plasticity models emanating from Mohr-Coulomb and Critical State plasticity theory. On the other hand, the fluid-like behavior of granular media is typically treated using constitutive theories amenable to viscous flow, e.g., Bingham fluid. In our proposed model, the material strength is composed of a dilation part and a rate-dependent residual strength. The dilatancy strength plays a key role during solid-like behavior but vanishes in the fluid-like regime. The residual strength, which in classical plasticity model is considered constant and rate-independent, is postulated to evolve with strain rate. The main appeal of the model is its simpleness and its ability to reconcile the classic plasticity and rheology camps. The applicability and capability of the model are demonstrated by numerical simulation of granular flow problems, as well as a classical shear banding problem, where

the performance of the continuum model is compared to discrete particle simulations and physical experiment. These results shed much-needed light into the mechanics and physics of granular media at various shear rates.

6.1. Introduction

A salient feature of dry granular media is its ability to feature a wide range of complex behavior, even though these materials are composed of relatively simple individual units or particles. Granular matter may behave like a solid in the quasi-static regime, such as sand dune; or like a fluid when a flow is provoked, such as granular avalanche; or even like a gas when strongly agitated [126]. While the mechanical behavior of granular materials is essentially governed by interactions between particles, the imperfect knowledge of contact forces between particles and prohibitive computational cost renders it impractical to model any field-scale problem by directly utilizing discrete models at the grain scale [82, 14]. To this end, a continuum description of granular materials is still of great importance for modeling and understanding natural hazards, such as landslides, rock avalanches, and for important industrial applications, such as powder handling, granulates in pharmacy, just to name a few.

Within the scope of interest to this work, i.e., solid- to fluid-like regime, the current understandings of granular materials are mostly confined to two extremes, i.e., solid-like behavior and fluid-like behavior. On the one hand, the solid-like state is typically tackled using soil plasticity models emanating from Mohr-Coulomb plasticity theory, see for instance, [57, 127, 128, 129, 130] among others. These plasticity models have been successfully implemented into numerical tools such as finite element methods and applied to

model quasi-static behavior of granular materials see e.g., [2, 12, 131]. Experiments conducted under quasi-static conditions have revealed that the strength of granular materials can be decomposed into a dilatancy strength and a residual strength [81, 132, 80, 133]. The dilatancy strength typically vanishes towards the so called critical state [81, 129], where granular materials undergo isochoric deformations. The material strength at the critical state is given by the residual strength, which is considered to be constant and rate-indepedent.

On the other hand, the flow of granular materials has been a very active research area in the physics community. Much of the work in this area focuses on steady regime of the flows, trying to identify relevant quantities such as flow threshold, kinematic profiles, effective friction. Extensive experiments and discrete particle simulations have been carried out on various configurations and geometries: flow on inclined planes [134, 135, 136, 137], roatating drum [138, 139], plane shear [140, 141] etc, see also [142] for a collection of results, and [143] for a review. From a theoretical point of view, even in very simple configurations with sphere-shaped particles, the flow can be very complex to model [139, 134]. Constitutive models have been developed to capture some of the key features of granular flow. One family of constitutive laws considers local rheology using dimensional analysis, where the effective friction coefficient and volume fraction are expressed as some functions of a dimensionless inertial number I [144, 145, 146]. For instance, in [144], a flow criteria and the dependence on shear rate were established, analogous to classical viscous Bingham fluids [147]. Quantitative predictions for flow shape and velocity profiles have been relatively successfully. Still, there are limitations for this approach, such as quasi-static or solid-like regime and hysteresis, which are not correctly

captured [148]. Other approaches have been proposed beyond the local rheology, linking rheology to the evolution of distribution of contacts [149, 150], or relating stress tensor to non-local functions of velocity field and material structures [151]. The depth-averaged or Saint-Venant equations first introduced by [152] have also been successfully applied to capture the main flow characteristics, see, e.g., [153, 154].

The aforementioned efforts have been mostly focusing on uniform steady flows, and the transition from solid-like to fluid-like state remains an open question in granular materials. A few efforts in experiments or numerical simulations have been proposed [139, 155, 137, 141], while constitutive models able to bridge these two domains are yet to be developed. To this end, we postulate in this paper a rate-dependent plasticity model aiming to bridge this gap. We adopt concepts from critical state soil mechanics [81], where the material strength classically decomposed into a dilatancy strength and a residual strength at critical state. However, unlike the classical critical state models, where the residual strength is constant, rate-dependent residual strength is postulated based on experimental and numerical evidence. Another key ingredient of the proposed model is the role of dilatancy, which is typically neglected in the study granular flows. It is believed that dilatancy plays a key role in the solid-like state, but vanishes in fluid-like state of granular materials. The proposed constitutive model features dilatancy as the many variable controlling solid-fluid behavioral transitions.

The remainder of the paper is structured as follows: in Section 2, the proposed constitutive model is presented within the framework of rate-dependent plasticity. Evolution laws for dilatancy and rate-dependent residual strength are postulated. In Section 3, the model is calibrated and verified using data from a numerical triaxial test done by discrete

element simulation. In Section 4, the model is put into tests for simulating a typical granular flow problem and a classical plane strain compression problem in soil mechanics, where results of both classical rate-independent model and the proposed model are compared with experiment data. Finally, some conclusions and discussions are presented in Section 5.

As for notations and symbols used in this paper, bold-faced letters denote tensors and vectors; the symbol '$\cdot$' denotes an inner product of two vectors (e.g. $\boldsymbol{a}\cdot\boldsymbol{b} = a_i b_i$), or a single contraction of adjacent indices of two tensors (e.g. $\boldsymbol{c}\cdot\boldsymbol{d} = c_{ij}d_{jk}$); the symbol ':' denotes an inner product of two second-order tensors (e.g. $\boldsymbol{c} : \boldsymbol{d} = c_{ij}d_{ij}$), or a double contraction of adjacent indices of tensors of rank two and higher (e.g. $\boldsymbol{C} : \boldsymbol{\epsilon}^{\mathrm{e}} = C_{ijkl}\epsilon^{\mathrm{e}}_{kl}$); the symbol '$\otimes$' denotes a juxtaposition, e.g., $(\boldsymbol{a}\otimes\boldsymbol{b})_{ij} = a_i b_j$. Finally, for any symmetric second order tensors $\boldsymbol{\alpha}$ and $\boldsymbol{\beta}$, $(\boldsymbol{\alpha}\otimes\boldsymbol{\beta})_{ijkl} = \alpha_{ij}\beta_{kl}$, $(\boldsymbol{\alpha}\oplus\boldsymbol{\beta})_{ijkl} = \alpha_{ik}\beta_{jl}$, and $(\boldsymbol{\alpha}\ominus\boldsymbol{\beta})_{ijkl} = \alpha_{il}\beta_{jk}$.

6.2. Rate-dependent rigid-plastic model for granular media

In this section, we present a rate-dependent phenomenological model to simulate the behavior of granular matter. In particular, the model is founded upon the basic features of material behavior: pressure-dependence, dilatancy, non-associative flow, and strain-rate dependence. The model departs from classic Coulomb plasticity and is able to evolve into Bingham-type flow. Furthermore, the model is cast within the critical state framework [129, 81], characterized by a state of isochoric deformations, i.e., zero dilatancy. For simplicity, we describe the model within the framework of rigid-plasticity and infinitesimal deformations such that $\dot{\boldsymbol{\epsilon}} = \dot{\boldsymbol{\epsilon}}^{\mathrm{e}} + \dot{\boldsymbol{\epsilon}}^{\mathrm{p}}$ applies and $\dot{\boldsymbol{\epsilon}}^{\mathrm{e}} \approx \boldsymbol{0}$, implying $\dot{\boldsymbol{\epsilon}} \approx \dot{\boldsymbol{\epsilon}}^{\mathrm{p}}$. Adding elastic deformations is standard and will be done in the examples section.

6.2.1. Yield surface and plastic potential

Consider the two stress invariants of the stress tensor $\boldsymbol{\sigma}$ such that

$$p = \frac{1}{3}\operatorname{tr}\boldsymbol{\sigma} \qquad \text{and} \qquad q = \sqrt{\frac{3}{2}}\|\boldsymbol{s}\| \tag{6.1}$$

with $\boldsymbol{s} = \operatorname{dev}\boldsymbol{\sigma}$ as the deviatoric projection of the stress tensor. Frictional materials, obey Coulomb-type relationships, where, at yielding, the mean normal stress is related to the deviatoric stress via frictional resistance, i.e.,

$$F(p, q) = q + \mu p = 0 \tag{6.2}$$

where μ is typically called the frictional resistance or friction coefficient and is related to the friction angle in granular materials. The frictional resistance can be either assumed constant or a function of the deviatoric strains. Typically, the latter is assumed and a phenomenological model to govern the evolution of μ is postulated.

Now, consider the two invariants of the strain rate tensor $\dot{\boldsymbol{\epsilon}}$, i.e.,

$$\dot{\epsilon}_{\mathrm{v}} = \operatorname{tr}\dot{\boldsymbol{\epsilon}} \qquad \text{and} \qquad \dot{\epsilon}_{\mathrm{s}} = \sqrt{\frac{2}{3}}\|\dot{\boldsymbol{e}}\| \tag{6.3}$$

with $\dot{\boldsymbol{e}} = \operatorname{dev}\dot{\boldsymbol{\epsilon}}$ as the deviatoric projection of the strain tensor. In granular materials, Reynolds [79] first realized the important role of the so-called dilatancy, which effectively couples deviatoric and volumetric components of deformation. This feature distinctly separates granular materials from other materials such as metals, which are non-dilative. It is important to note that dilatancy plays a central role in the mechanical behavior of granular matter. For instance, dilatancy contributes to strength and depending on

the relative packing density of the material, it can allow for macroscopic contraction or dilation. Consider the plastic potential

$$Q(p, q) = q + \beta p - c = 0 \tag{6.4}$$

where β is defined as the dilatancy and c is a free parameter to ensure that the stresses in F and Q coincide.

In classic plasticity, the plastic volumetric stain rate is obtained from the plastic potential such that

$$\dot{\boldsymbol{\epsilon}} = \dot{\lambda}\frac{\partial Q}{\partial \boldsymbol{\sigma}} = \dot{\lambda}\left(\frac{1}{3}\beta\mathbf{1} + \sqrt{\frac{3}{2}}\hat{\boldsymbol{n}}\right) \tag{6.5}$$

where $\hat{\boldsymbol{n}} := \boldsymbol{s}/\|\boldsymbol{s}\|$ is the unit deviatoric tensor and $\mathbf{1}$ is the second-order identity tensor. From this equation, we can conclude that $\dot{\boldsymbol{e}} := \operatorname{dev}\dot{\boldsymbol{\epsilon}} = \dot{\lambda}\sqrt{3/2}\hat{\boldsymbol{n}}$ and that $\dot{\boldsymbol{e}}$ and $\boldsymbol{s}$ are coaxial. From these realizations it follows that dilatancy is defined such that

$$\dot{\epsilon}_{\mathrm{v}} = \beta\dot{\epsilon}_{\mathrm{s}} \tag{6.6}$$

Note that dilatancy, as the frictional resistance, can be considered either a constant or a function of the deformation. Associative plastic flow would require $\beta = \mu$. Furthermore, a direct constitutive relation is obtained between the deviatoric stress and the deviatoric strain rate, i.e.,

$$\boldsymbol{s} = \eta\dot{\boldsymbol{e}} \qquad \text{with} \qquad \eta = -\frac{3}{2}\frac{\mu p}{\dot{\epsilon}_{\mathrm{s}}} \tag{6.7}$$

Equation (6.7) is reminiscent of constitutive relations for non-Newtonean fluids where the deviatoric stress depends on the deviatoric strain rate via a viscosity term η [147, 144].

The constitutive picture is completed by postulating the evolution of the frictional resistance and dilatancy. We propose a classical stress-dilatancy relation, where the frictional resistance is a function of the dilatancy and some residual resistance such that [81]

$$\mu = \beta + \bar{\mu} \tag{6.8}$$

In classic soil mechanics, $\bar{\mu}$ is the residual resistance of the material and is considered constant. However, flow experiments in granular materials at different deformation rates and at steady-state have shown that the frictional resistance is a function of the deviatoric strain rate [142, 144]. When at steady-state, the granular material must have mobilized all the dilatancy and must be at critical state so that $\beta = 0$ and $\mu = \bar{\mu}$. Figure 6.1 shows typically observed evolution of the residual resistance as a function of the deviatoric strain rate. The figure helps reconcile the apparent rate-independence observed in quasi-static experiments in granular materials: they are conducted at very low shear strain rates. As shear strain rates are increased, the material's residual frictional resistance increases. This phenomenological observation will be a key feature of the proposed model and will afford it capturing solid and fluid features accurately.

Remark 14. As Reynolds [79] pointed out, it is the dilatancy β what separates granular matter from other materials, say, non-Newtonean fluids. At the same time, pressure p also plays a fundamental role in the mechanical behavior of granular matter.

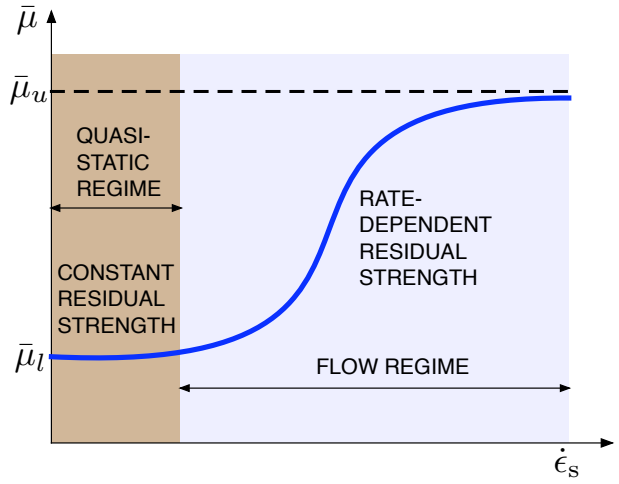

Figure 6.1. Observed evolution of the residual frictional resistance in granular material flow at steady-state.

The consequence of dilatancy is that the deviatoric and volumetic strain rate components are coupled (see equation (6.6)) and that frictional strength is enhanced by the dilatancy (see equation (6.8) and Figure 6.2). Once dilatancy is fully spent or critical state is achieved ($\beta = 0$), flow becomes incompressible. At this point, the formulation reduces to pressure-dependent incompressible non-Newtonian flow. As shown in Figure 6.2, dilative strength is what separates the solid-like state from the fluid-like state. Consequently, in this model, the critical state marks the transition between solid-like and fluid-like states.

Remark 15. Classical plasticity has considered $\bar{\mu} = \bar{\mu}_l$ constant since, for most applications, quasi-static conditions ($\dot{\epsilon}_s \approx 0$) apply. However, it can be seen from the above constitutive framework that the residual strength $\bar{\mu}$ is rate dependent and can be included in the formulation relatively easily. Numerical experiments under triaxial compression at different strain rates and infinite slope show this important feature in the following sections.

Remark 16. Figure 6.2 shows interpretations of the proposed strain-dependent simple model. The figure implies that at $\epsilon_s = 0$ we have $\beta = 0$. This is assumed for simplicity and clarity but it is an approximation as it neglects the initial compression in the material. Adding elastic compressibility would eliminate this approximation. The explicit form of the model should be considered as an approximation, our objective is not to postulate a specific model form or evolution, but rather a combined framework that allows the co-existence of classic frameworks such as critical state and Bingham flow, affording enhanced accuracy.

6.2.2. Evolution equations

In the present model, the governing material plastic internal variables are the frictional resistance μ and the dilatancy β. As mentioned before, in traditional rate-independent plasticity models (which have dominated in granular materials literature), the residual strength $\bar{\mu}$ is considered constant and, therefore, in order to complete the constitutive picture, it suffices to postulate an evolution law for the dilatancy. Experiments suggest that, at quasi-static rates, the dilatancy might be dependent on pressure and deviatoric shear strain. Therefore, a general form of dilatancy could be written as $\beta = \beta(p, \epsilon_s)$, as has been used to model the dilatancy evolution of granular soils under quasi-static conditions using constant parameters [71, 2]. However, for simplicity of presentation—and lack of thorough experiments, we will consider the only deviatoric shear strain dependence, and postulate a simple function for the dilatancy evolution as

$$\beta(\epsilon_s) = \beta^* \frac{\epsilon_s}{\epsilon_s^*} \exp\left(1 - \frac{\epsilon_s}{\epsilon_s^*}\right) \tag{6.9}$$

where β^* is the maximum dilatancy and ϵ_s^* is the corresponding shear strain. It should be noted that the evolution equation for β in Figure 6.2 allows for shear rate-dependence, if necessary. In equation 6.9 this feature has been turned off. The rate-dependence of dilatancy has not been observed in the numerical experiments conducted herein, but cannot be discarded at this point.

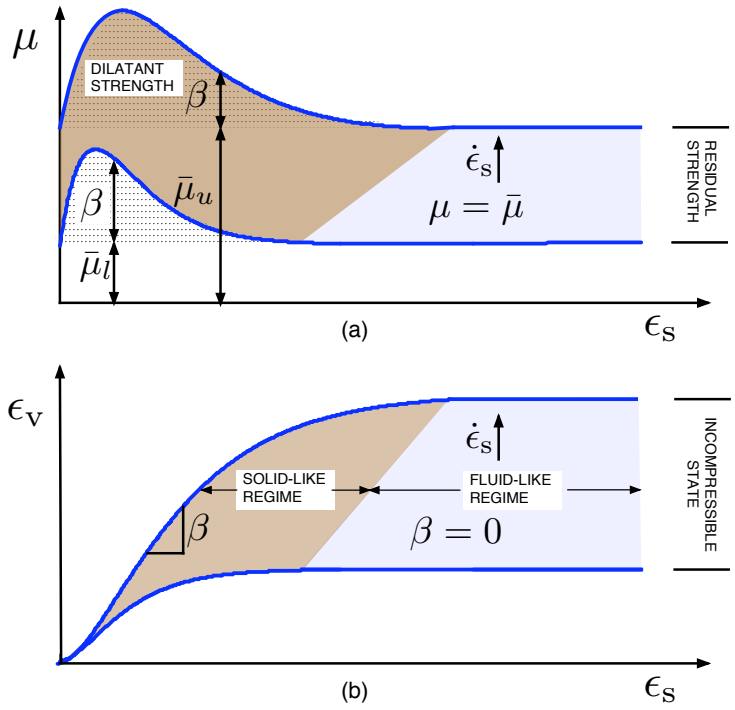

Figure 6.2. Interpretation of proposed constitutive model under constant shear strain rates $\dot{\epsilon}_s$ based on axisymmetric compression simulations. (a) Frictional strength μ and (b) volumetric strain ϵ_v vs. shear strain ϵ_s. Both strength μ and dilatancy β (alternatively, ϵ_v) are shown to increase with the increasing shear strain rate $\dot{\epsilon}_s$.

By the same token, numerical and experimental results on steady-state flow of granular materials have shown a clear rate dependence of $\bar{\mu}$, similar to that shown in Figure 6.1. The rate dependence for the residual strength has been proposed to take the simple form [144]

$$\bar{\mu} = \bar{\mu}_l + \frac{\bar{\mu}_u - \bar{\mu}_l}{1 + \dot{\epsilon}_s^*/\dot{\epsilon}_s} \tag{6.10}$$

where $\bar{\mu}_l$ is the lower bound for the residual resistance when $\dot{\epsilon}_s \to 0$. This is often called the quasi-static range. On the other hand, $\bar{\mu}_u$ is the upper bound achieved as $\dot{\epsilon}_s \to \infty$. The upper bound would mark the end of the flow regime and transition into the gaseous regime [126] (where this model no longer applies). Furthermore, $\dot{\epsilon}_s^*$ signifies the shear strain rate at which the residual friction $\bar{\mu} = 1/2(\bar{\mu}_l + \bar{\mu}_u)$.

The resulting evolution for the friction resistance can be written as a function of the dilatancy and residual resistance and is given as a function of the cumulative shear strain and the shear strain rate so that

$$\mu\left(\epsilon_s, \dot{\epsilon}_s\right) = \beta\left(\epsilon_s\right) + \bar{\mu}\left(\dot{\epsilon}_s\right) \tag{6.11}$$

This expression is an enhancement of the classic rate-independent plasticity models to account for the rate effects observed in the residual resistance. Also, this framework incorporates basic plasticity axioms for granular materials such as the critical state [129, 81]. In fact, achievement of the critical state (i.e., $\beta = 0$) signifies the transition into incompressible rate-dependent flow, as we will see in the examples below.

Remark 17. The evolution laws introduced above are by no means complete or universal. They are simply introduced to account for the most salient features of granular matter in the simplest way. As more experiments become available, better calibration of the above evolution laws can be achieved or new evolution laws can be proposed all together. Nevertheless, the next sections will show that this simple framework can capture several important features in the material behavior and the transition between the solid-like and fluid-like states, even though very simple evolution laws have been used.

6.3. Model calibration and verification

In this section, the model is calibrated using data from numerical experiments performed by discrete element method (DEM) and verified through a series of triaxial compression tests under different loading rates. Of particular interest is that the model is able to capture desired features of granular materials, which cannot be obtained by using conventional rate-independent plasticity models or granular flow models alone. Also, computational efficiency is demonstrated by implementing the plasticity model within the return mapping framework [13].

6.3.1. Model calibration with discrete element simulation

The numerical experiments used to calibrate the model are performed using DEM. Initial configuration and loading conditions for the DEM simulation are shown in Figure 6.3. The sample size is $(48 \times D_{50})^3$, where D_{50} is the mean particle diameter. Lateral confining stresses of 25 kPa are applied and the top of the sample is compressed under strain controlled boundary conditions. Two strain rates are applied: a low rate of 0.002/s and

a high rate of 0.04/s. Parameters used in the DEM simulation are summarized in Table 6.1.

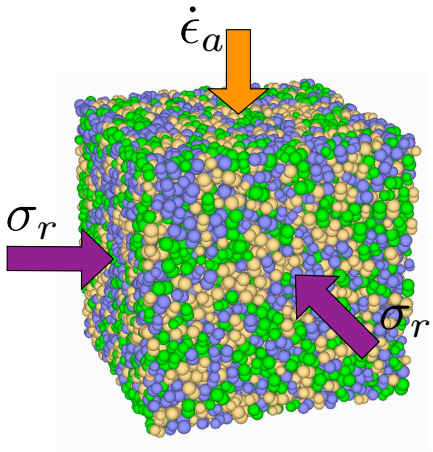

Figure 6.3. Initial configuration and loading conditions for polydispersed granular assembly in DEM computation. Different colors correspond to different particle diameters.

Symbol	Parameter	Value
N	Number of particles	9092
D_{50}	Mean particle diameter	0.125m
k_n	Normal contact stiffness	$1e8$ N/m
k_t	Tangential contact stiffness	$1e7$ N/m
μ_p	Interparticle friction coefficient	0.31
c_n	Local damping coefficient	0.7

Table 6.1. Parameters used in DEM triaxial simulations for calibrating model.

The stress ratio versus shear strain for both low and high strain rate tests are shown in Figure 6.4(a). As typically seen in dense granular materials, for both cases, the stress ratio increases to a peak value and then gradually decreases (softening behavior) to a constant value, i.e., the residual resistance $\bar{\mu}$. For high loading rate, $\bar{\mu} = 1.5$ and for low loading rate, $\bar{\mu} = 1.05$.

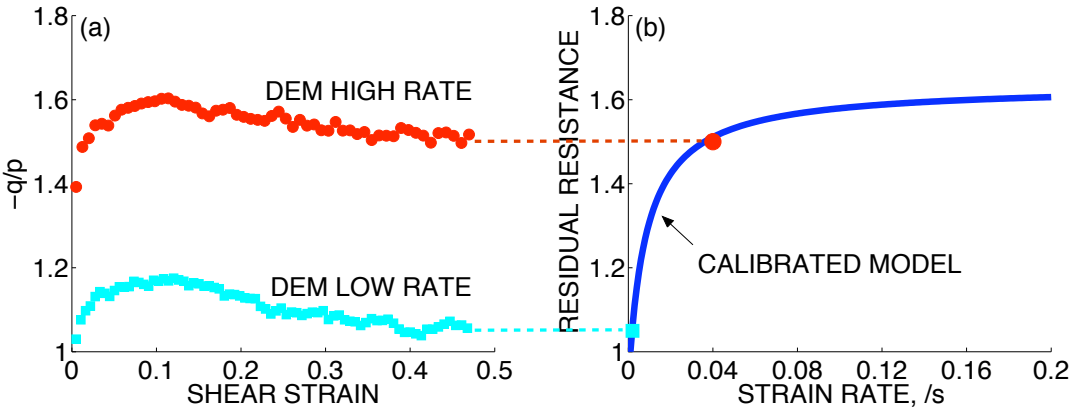

Figure 6.4. Triaxial compression numerical experiments using DEM: (a) Evolution of stress ratio under two different loading rates; (b) Calibrated evolution of residual strength for the proposed model, cf., equation (6.10).

The lower and upper bound of the residual strength and the corresponding shear strain rate are determined such that the calibrated evolution as proposed in equation (6.10) passes the two known points given by DEM simulations. Figure 6.4(b) shows the calibrated evolution of residual strength $\bar{\mu}$, as well as the two DEM data points. Parameters corresponding to this evolution are $\bar{\mu}_l = 0.9$, $\bar{\mu}_u = 1.6$, and $\dot{\epsilon}_s = 0.0085$.

To calibrate the dilatancy parameter β, the evolution of the volumetric strain vs. deviatoric strain curves for the two different strain rates in the DEM simulations are computed and shown in Figure 6.5(a). Using equation (6.6), dilatancy can be computed using a simple finite difference scheme. The results are shown in Figure 6.5(b), from which we obtain the maximum dilatancy $\beta^* \approx 0.2$ and the corresponding shear strain $\epsilon_s^* = 0.05$. The calibrated evolution of diltancy (cf., equation (6.9)) is shown as the solid line in Figure 6.5(b).

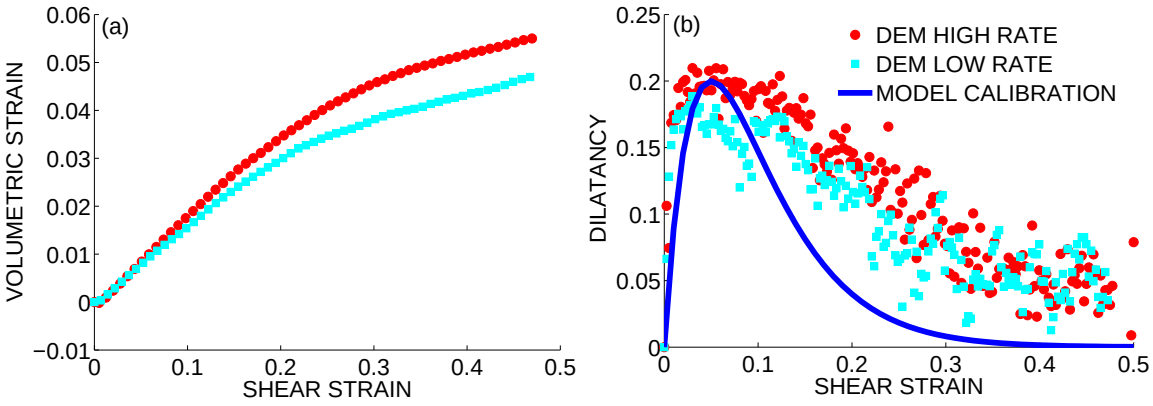

Figure 6.5. Dilatancy calibration: (a) Volumetric strain vs. deviatoric strain in the triaxial compression tests by DEM; (b) computed dilatancy from DEM as well as calibrated dilatancy evolution for the proposed model.

Remark 18. It can be seen from the above DEM triaxial compression numerical experiments that the volumetric strains and hence dilatancy do not seem to strongly depend of deviatoric strain rates. This is the reason why this dependence has been ignored in this work. Hoewever, in general, and as shown in Figure 6.2(b), dilatancy can be a function of strain rates.

6.3.2. Model verification: triaxial compression test at various loading rates

To verify the proposed constitutive model, we implemented it in a finite element (FE) code to simulate boundary value problems. For comparison, we impose in the FE analysis the same boundary conditions as those in the DEM numerical experiments, but with a wider range of loading rates. The loading rates range from a quasi-static loading, where the residual strength of the material is given by the lower bound $\bar{\mu}_l$, up to 'very' fast

loading rate, where the upper bound of the residual strength is approached at critical state.

Figure 6.6(a) shows the resulting stress ratio $-q/p$ versus shear strain at different loading rates. The two dashed lines represent the lower and upper stress bounds, corresponding to quasi-static and infinitely-fast loading, respectively. Solid lines are from FE simulations using the plasticity model with the parameters calibrated from before. The data from two DEM experiments are also plotted in the same figure. The model is able to capture some key features, including the softening behavior and rate-effects. On Figure 6.6(b), triangles represent the residual strengths from the FE simulation at different rates. Solid line is the model input, i.e., the calibrated evolution. It is clear that the model is correctly taken into account the rate effects on residual strength as expected.

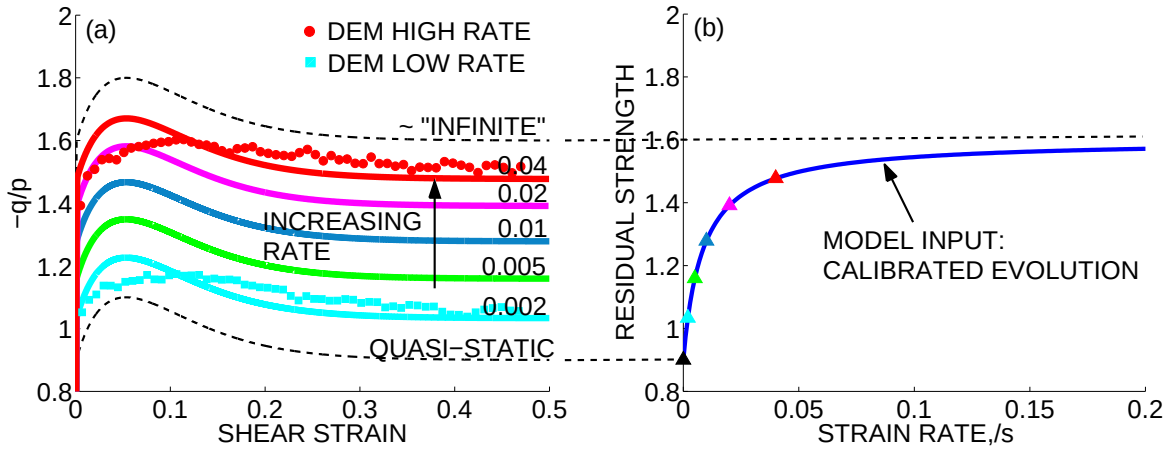

Figure 6.6. (a) Stress ratio versus shear strain at different loading rate of the triaxial compression tests (numbers on the right correspond to loading rate,/s); (b) Corresponding residual strength on the model calibrated evolution curve.

If classical granular flow models or rate-independent plasticity models were to be used independently, the aforementioned features, such as softening and rate-effects, could not be captured. This is because the classical granular flow models usually ignores dilatancy and the material strength is given by residual resistance only, which is constant for a given strain rate. While in the rate-independent plasticity models, the rate effects on residual strength are neglected, so material strength does not evolve with loading rate. To illustrate this, we perform FE simulations neglecting either dilatancy or rate effects, respectively. Figure 6.7 shows comparisons between the proposed model with (a) if dilatancy is neglected; and (b) if rate effect on residual strength is neglected. Clearly, neither simplification would yield the desired features as observed in the numerical experiments. Nevertheless, these are the current paradigms used to model granular materials.

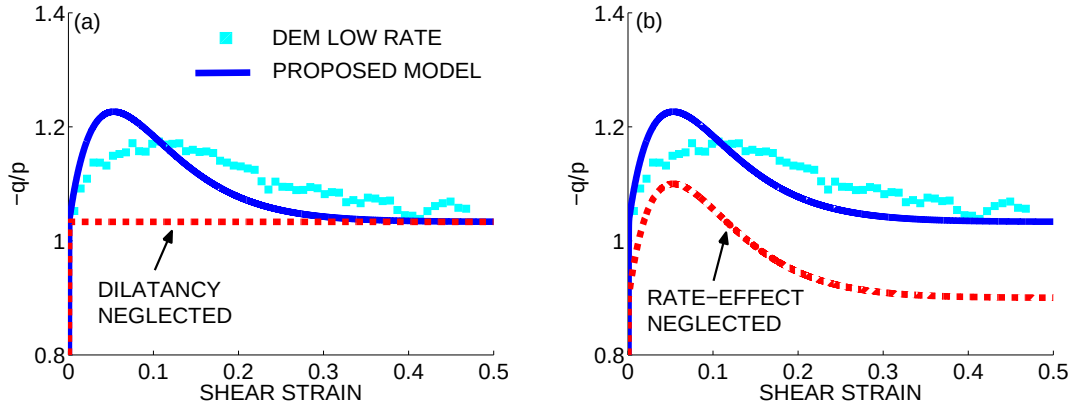

Figure 6.7. Triaxial compression test at loading rate $\dot{\epsilon}_a = 0.002/s$: proposed model compared with (a) dilatancy effect neglected; (b) rate-dependence of residual strength neglected.

As far as verification is concerned, the final aspect we look at is the computational efficiency. Figure 6.8 shows the reported global and local residual profiles at different

strain levels. It is clear to see that all iterations converge below a tolerance (in this example, 10^{-13}) within 5 steps. Asymptotic quadratic convergence rates are obtained for both global and local cases. This effitientcy will prove crucial as the model can be implemented using explicit or implicit FE or finite difference codes and obtain solutions of boundary value problems (BVP) in seconds. This is to be contrasted with simulations using DEM, which can take up to days to run, for the same BVP.

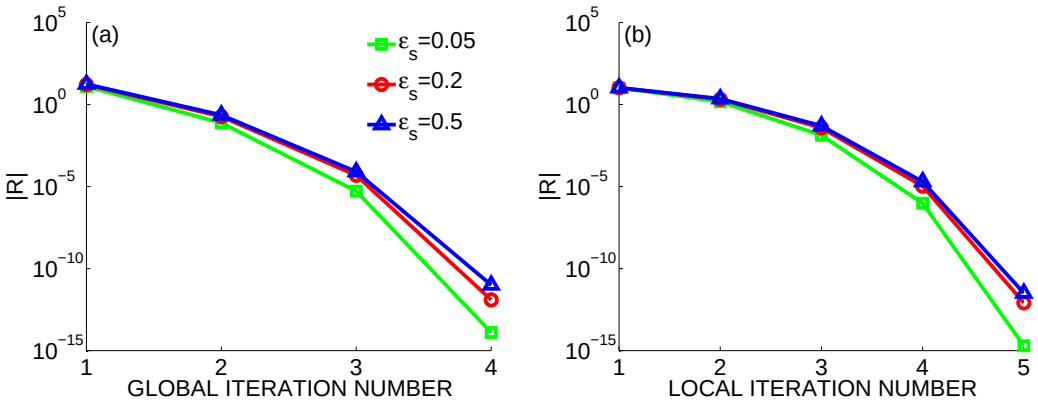

Figure 6.8. Convergence profile at different strain level, for (a) global level; (b) local (material point) level. R is the residual.

So far, the model has been calibrated using results from numerical experiments done by discrete element simulations, and verified through some boundary value problems. In the next section, we will show two applications of the proposed model towards a classical granular flow problem and a shear banding problem in soil mechanics. These examples will further highlight the efficiency of the method and its accuracy.

6.4. Numerical examples: application to granular flow and classical shear banding problem

In this section, the proposed constitutive model is utilized to simulate a granular flow problem and a plane strain shear banding problem. These two examples represent classical problems studied in physics community for understanding fluid-like behavior in granular flow, and in the soil mechanics community for understanding solid-like behavior of granular materials under quasi-static macroscopic loading. In the first example, DEM simulations are used as bench marks that the continuum model will be compared to. The intention is to show that the simple proposed constitutive model is able to seamlessly capture the transition from solid-like to fluid like behavior, as well as steady-state flow. In the second example, a physical plane strain compression experiment will be analyzed, showing the improved residual strength given by the proposed model. The plane strain compression example postulates the importance of rate effects once shear bands form within otherwise homogeneously deforming samples.

6.4.1. Granular flow along an inclined infinite slope

In this section, numerical experiments of granular flow along an inclined infinite slope are compared against simulations performed using the proposed model. The numerical experiments are carried out using discrete element simulations, with dimensions of the simulation box shown in Figure 6.9. Periodic boundary conditions are enforced in the flow direction, as well as in the y direction so that the sidewall effects on the flow are neglected. The surface of the inclined slope is glued with one layer of particles of same diameters. The granular assembly consists of monodispersed spheres with radius $r = 1.2$ mm. In

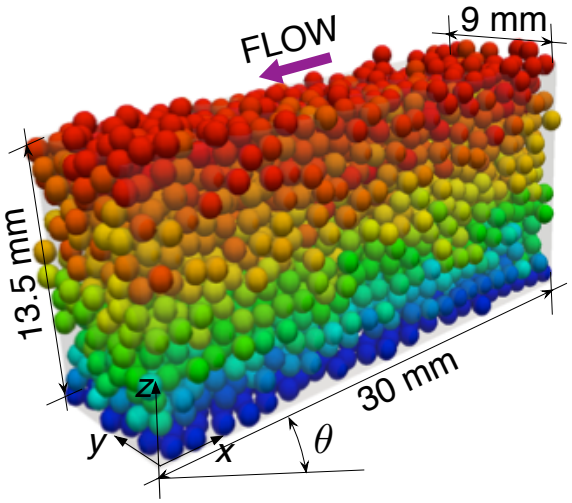

Figure 6.9. Assembly of monodispersed granular particles with radius of 1.2 mm on a slope inclined at angle θ from the horizontal plane.

the numerical experiments, the simulation box is initially horizontal and the granular assembly is in a solid-like state. Then, the simulation box is instantaneously tilted to an angle θ from the horizontal direction to induce granular flow. Some (intermmitent) particle movements are observed when the inclination angle $\theta = 19°$, but it is not until $\theta = 22°$ that steady-state granular flow can be achieved. If $\theta > 25°$, flow will keep accelerating without bound, i.e., no steady-state flow can be reached. These DEM results allow us to obtain bounds for our continuum model, as $\theta = 19°$ seems to correspond to the angle of repose and $\theta = 25°$ introduces an upper bound for the residual strength. Further, since the problem is essentially one-dimensional, only velocity profiles along the depth z direction and surface velocities are reported.

To simulate the granular flow problem using the continuum model, we have to solve the momentum balance equation written as

$$\nabla \cdot \boldsymbol{\sigma} + \rho \boldsymbol{g} = \rho \frac{\mathrm{d}\boldsymbol{v}}{\mathrm{dt}} \tag{6.12}$$

where $\boldsymbol{\sigma}$ is the Cauchy stress tensor, ρ is the particle density, $\boldsymbol{g}$ is gravitational acceleration vector and $\boldsymbol{v}$ is the velocity. Also, the boundary conditions are: traction free on the top surface, zero displacement/velocity at the bottom of the assembly. It should be noted that once sidewall effects and surface roughness are taken into account [**156**, **143**, **157**], different boundary conditions have to be chosen.

Finite difference method is implemented to solve equation (6.12). Time and spatial discretizations are carefully chosen such that the Courant-Friedrichs-Lewy stability criterion is satisfied [**158**]. The proposed rate-dependent constitutive model is used to describe material behavior and the resulting finite difference governing equation reads,

$$\Delta v = \frac{1}{1+\mu\beta}\Delta t g \cos\theta\,(\tan\theta - \mu) \tag{6.13}$$

where v is the velocity in the flow direction at a given space finite difference node and $\Delta v = v_{n+1} - v_n$ and $\Delta t = t_{n+1} - t_n$, representing time discretization. Equation (6.13) is the discrete version of equation (6.12) plus constitutive assumptions. Also, we have exploited the infinite character of the problem and hence quantities only vary in the z-direction. Also implied in equation (6.13) is the relationship between internal strength furnished by μ and external forces furnished by $\tan\theta$ (gravity). As long as the material can produce enough internal strength to balance external forces, equilibrium or steady state conditions will be achieved. Otherwise, the external loads will drive the system into continuous acceleration.

The frictional resistance μ is given by equation (6.11). Material parameters corresponding to the infinite slope problem are calibrated as follows. As noted before, the angle of repose is defined as the angle at which intermitent flow begins, which is observed

form DEM simulations to be 19°, hence, $\bar{\mu}_l = \tan 19°$. By the same token, continuous flow is achieved in DEM simulations at 22°. In our model, we interpret this 3° difference as a result of the peak dilation, hence, we assume $\beta^* = \tan 3°$ with a corresponding (assumed) $\dot{\epsilon}_s^* = 3.5$. Finally, since the DEM simulations grow unbounded when $\theta > 25°$ we assume $\bar{\mu}_l = \tan 25°$.

Figure 6.10 shows velocity profiles for various angle inclinations as a function of depth at selected time stations. Dots correspond to DEM simulations while solid lines are results from our continuum model. Colors represent specific time stations in the simulation. It can be seen that the velocity increases gradually, eventually reaching a steady-state profile. The continuum model is able to reproduce the velocity profiles observed in DEM well and is able to capture the transition from solid-like behavior (close to zero velocity) to fluid-like behavior, eventually resulting in steady state conditions.

Surface velocity is also of particular interest. Figure 6.11 shows the evolution of surface velocity for different inclination angles where steady state flows can be reached. The steady state surface flow velocity increases with inclination angles. Again, the simple proposed model is able to reproduce this key feature, and matches well with numerical DEM experiments. Also, this figure displays the clear rate dependent behavior of the material. At steady-state, and as shown in equation (6.13), accelerations are zero and the material strength $\mu = \tan\theta$. Hence, by looking at the steady-state velocities, one can obtain steady-state strain rates that correspond to residual strengths as shown in Figure 6.11. This means that the material is increasing in strength since it is able to equilibrate at higher inclination angles, at the expense of higher steady-state velocities

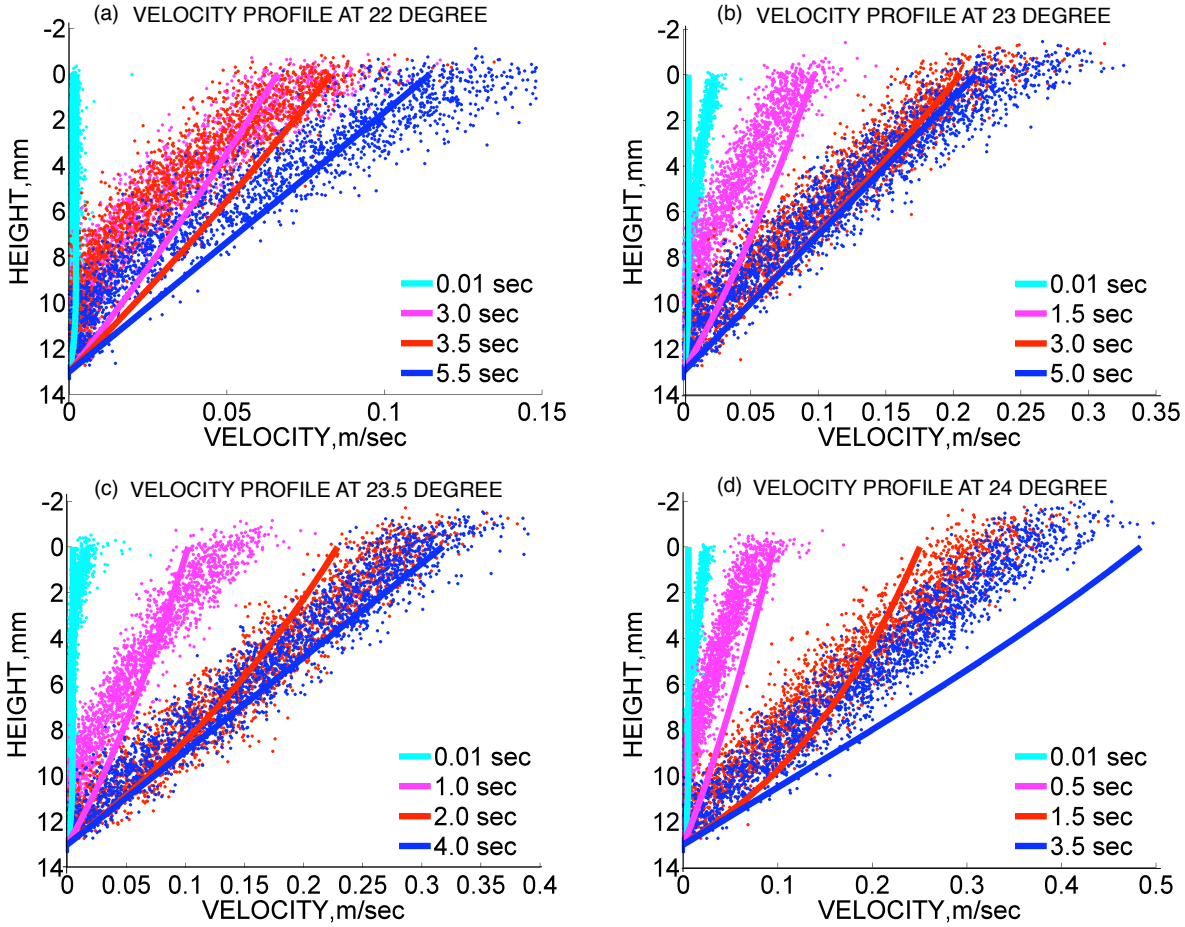

Figure 6.10. Velocity (along the flow direction) profiles for different inclination angles (a) $\theta = 22°$; (b) $\theta = 23°$; (c) $\theta = 23.5°$; (d) $\theta = 24°$. (dots: numerical experiments; solid lines: model calculation)

(higher strain rates). This feature can only be fully captured by the proposed rate-dependent continuum model.

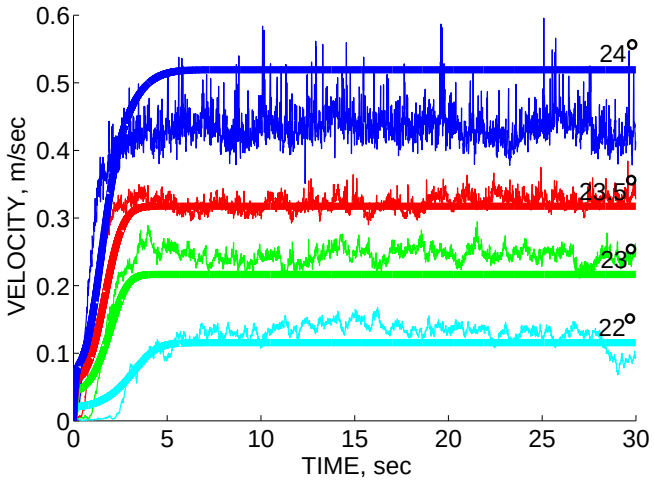

Figure 6.11. Evolution of surface velocity (flow direction) for different inclination angles. (nonsmooth lines: DEM numerical experiments; smooth lines: continuum model calculation)

To show the limitations of using classic modeling paradigms we perform simulations with either rate-independent plastic model and Bingham fluid model. To capture the first classical model, we simply turn off the rate dependence in the residual strength and make $\bar{\mu} = \tan 19^\circ$ constant. For the Bingham flow model, we turn off the dilatancy contribution and make $\beta = 0$. Figure 6.12 shows results for inclination angle $\theta = 22^\circ$. If dilatancy is neglected, as shown in Figure 6.12(a), the granular flow reaches steady-state almost right at the beginning. No transition from solid to fluid state is observed. If the residual strength remains constant, i.e., no rate effect, the flow will keep accelerating and never reaches steady state, as shown in Figure 6.12(b). This highlights the importance of the combined model as being the only one to capture all the salient features: dilatancy dominated plasticity at early stages of deformation (solid-like regime), transition marked

by full use of dilatancy, and residual strength rate dependent response (fluid-like regime) where deformations are purely isochoric.

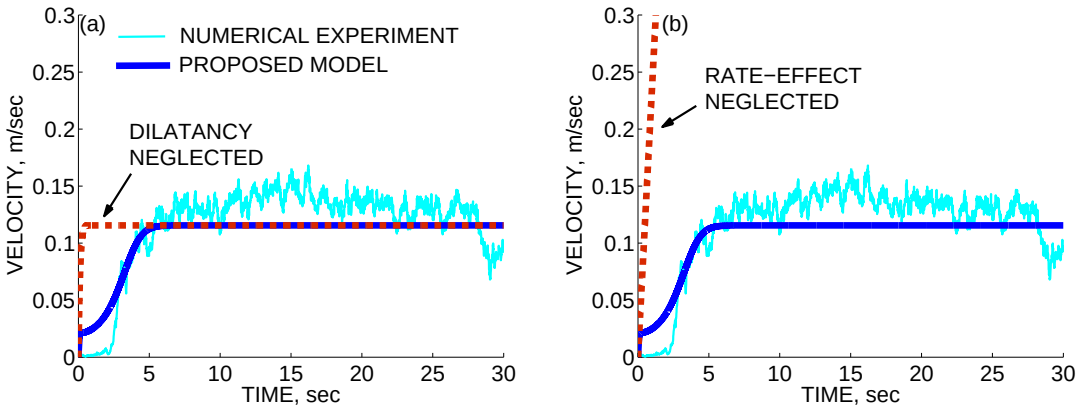

Figure 6.12. Granular flow along inclined surface $\theta = 22°$: the proposed model compared with (a) dilatancy effect neglected; (b) rate-dependence of residual strength neglected.

6.4.2. Plane strain shear banding problem

In this section, the proposed continuum model is applied to analyze the behavior of a physical experiment on dense sand under plane strain condition. This is a revisit of the analysis done by [12], where the rate effect on the residual strength $\bar{\mu}$ was neglected. While the previous analysis in [12] captured the behavior of the materials well for most part of the loading, disparity between simulation and experiment at the critical state was clearly observed. It is believed that the rate-independent model may have missed some important feature of the material behavior, i.e., different strain rates inside and outside the shear band after localization. The objective of the current analysis is to show that, by adopting the proposed rate-dependent constitutive model, the effects of strain rate on

material behavior is taken into account, and material residual strength could be more realistically captured.

The physical experiment was performed by [15] on a masonry sand sample of 140 × 80 × 40 mm in dimensions. Plane strain was enforced by two rigid (smooth) walls, in the 80 mm direction. The sample was initially consolidated anisotropically with axial stress $\sigma_a = -210$ kPa, and lateral stress $\sigma_r = -105$ kPa. After consolidation, the lateral stress was kept constant while the top plate was moved down with a loading rate of $\dot{\epsilon}_a \approx 1.4\%/\text{hr}$. A dominant shear band inclined 63° from the horizontal axis was observed when the global axial strain reached about 3%. Evolution of dilation angle ψ was extracted using stereophotogrammetry, and was related to dilatancy parameter β through

$$\beta = \tan\psi \tag{6.14}$$

Figure 6.13 shows the evolution of dilatancy angle obtained in the experiment (red circles). This phenomenological evolution of dilation will be used in this example instead of the equation proposed in (6.9). This concept of using dilation evolution from local strains has been used before in the context of multiscale simulations which details can be found in [12, 2]. In Figure 6.13 the solid line corresponds to the idealized evolution of dilation angle for materials inside the band, while the dotted line is for materials outside the band. The assumption of a constant dilation angle after localization outside the band is immaterial, since all plastic deformations are concentrated within the shear band and the material outside undergoes elastic unloading.

In the numerical simulations, the proposed rate-dependent constitutive model is used to describe material behavior, with the Drucker-Prager type yield surface and non-associative

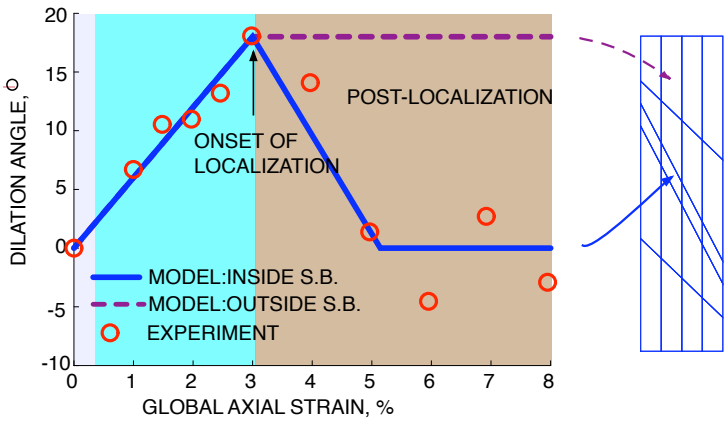

Figure 6.13. Evolution of dilation angle observed in the experiment and input into the finite element model.

flow rule as presented before. The frictional resistance μ is related to dilatancy parameter β and residual resistance $\bar{\mu}$ through equation (6.11), and therefore depends on shear strain rate. Instead of using equation (6.9) for β, the measurements from the experiment shown in Figure 6.13 are directly incorporated into the model. Calibrated parameters used in the model are two elastic constants $E = 40$ MPa, $\nu = 0.2$; and $\bar{\mu}_l = 1.15$, $\bar{\mu}_u = 1.5$, $\dot{\epsilon}^*_s = 1.0$.

It has been shown that the characteristic length of shear bands in granular materials is in the order of 10-20 mean particle diameters. Since most samples have characteristic macroscopic dimensions in the order of thousands of grains, strain rates inside the shear band are bound to jump by orders of magnitude once a band forms. If the material is rate-dependent, this could measurably change the behavior of the material post bifurcation. This is the idea pursued on this example. The proposed rate-dependent model is able to take into account this effect. Shown in Figure 6.14 is the evolution of the residual strength inside and outside the shear band throughout the simulation. There is a significant increase of the residual strength for materials inside the shear band right at the point of

localization due to the increase of strain-rate. For materials outside, the residual strength remains close to the constant value $\bar{\mu}_l = 1.15$. If a rate-independent model is used, there would be no difference in the residual strength for materials inside and outside the band.

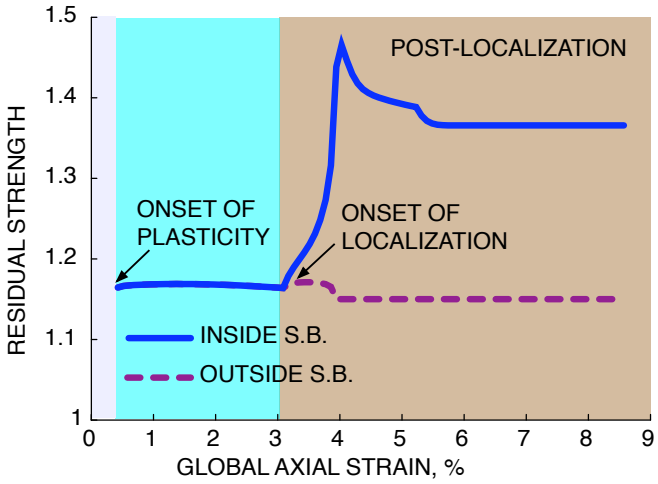

Figure 6.14. Evolution of the residual strength $\bar{\mu}$ inside and outside the shear band.

The evolution of the global stress ratio with global axial strain is shown in Figure 6.15. There is some disparity between the rate-independent model and experiment results, especially post bifurcation and at critical state. As mentioned before, it is hypothesized that the significantly higher strain rate, could trigger rate effects inside the shear band. In this particular case, there is a slight increase in strength, which seems to improve the results significantly, as shown by the solid line in Figure 6.15. Similarly, if a simulation is conducted using only a rate-dependent fluid model (by turning off the dilatancy effect), the model completely misses the transient effect and produces a constant stress ratio corresponding to the final residual strength in the continuum model. This is clearly undesirable. The continuum model proposed here is able to obtain better results than the classic counterparts.

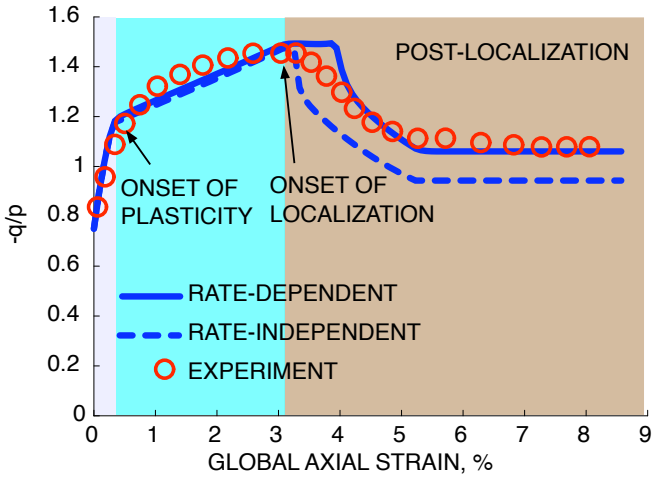

Figure 6.15. Evolution of stress ratio with global axial strain.

Finally, the deviatoric stress and strain contours of the sample at the end of the simulation are shown in Figure 6.16 and Figure 6.17. There are clear concentrations of shear stress and strain inside the band as expected. Also, it can be seen that the shear strain contours are virtually the same for the rate-independent and rate-dependent models, as expected. On the other hand, because rate-dendence of material strength is taken into account, the proposed rate-depedent model displays higher shear stresses inside the band. This of course, results in an apparent increase in global sample strength.

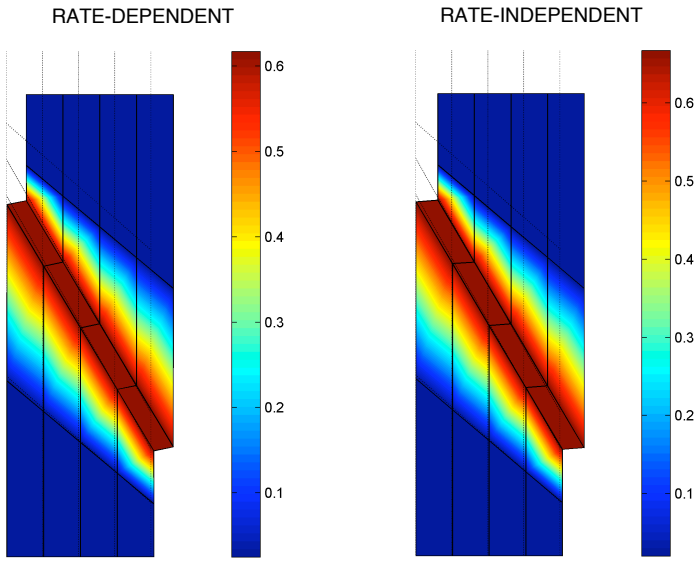

Figure 6.16. Shear strain contour at the end of the simulation ($\epsilon_a \approx 8.5\%$) for both rate-dependent and rate-independent models.

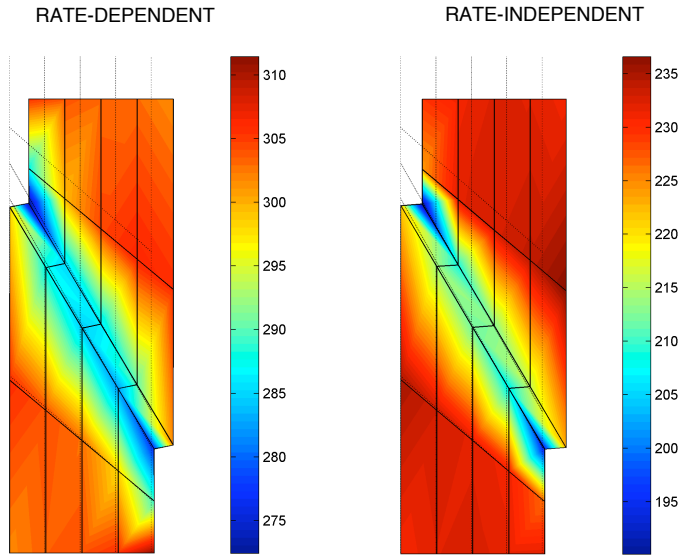

Figure 6.17. Shear stress contour at the end of the simulation ($\epsilon_a \approx 8.5\%$) for both rate-dependent and rate-independent models.

6.5. Conclusions

We have presented a rate-dependent plasticity model for dilative granular media aiming to bridge the solid- and fluid-like state of such materials. The model emanates from classical plasticity model in soil mechanics where material strength is composed of a dilatancy strength and a residual resistance. The model accommodates the material behavior transition by proposing the evolution of dilatancy, which plays a key role in the solid-like state but vanishes towards the fluid-like state. The residual strength is proposed to be rate-dependent, affording it key features of fluid-like state in granular materials. The model is calibrated using numerical experiments by discrete element method simulations and verified by boundary value problems. Though simple in form, the capability of the model to reconcile classical plasticity and rheology camps has been shown through the successful applications to a classical granular flow problem, where key features such as solid-fluid transition, velocity profiles and free-surface velocity evolutions are captured. Neither classical rate-independent plasticity theory nor steady-state granular flow model alone would be able to capture these features at the same time. Finally, the model is applied to a shear banding problem, where the rate-effect on material strength inside and outside shear band has been considered and results from the model match well with experiment observations. It is anticipated that the proposed model will spur the development of more accurate models able to transit classic plasticity and non-Newtonian fluid models, and as a result capture the observed physics with higher accuracy.

Acknowledgments

Support for this work is provided by AFOSR grant number FA9550-08-1-1092. This support is gratefully acknowledged.

CHAPTER 7

Concluding remarks and future work

7.1. Summary of conclusions

In this dissertation, we have presented multiscale approaches for modeling of failure in granular materials, where continuum scale constitutive descriptions were enhanced by extracting information from finer scales. Representative failure phenomena, i.e., localized failure (Chapters 3 and 5) and state transition (Chapter 6), were studied, covering from continuum scales to granular scale. Special attentions were paid to what appropriate information needs to be passed and how the constitutive models can be enhanced. Two methodologies were discussed: (1) within the continuum regime, the constitutive responses at the coarse scale were obtained directly by homogenized stresses and constitutive tangents from finer scales through a concurrent multiscale framework; (2) from continuum scale to granular scale, evolutions of key material parameters, such as friction and dilatancy, were extracted from granular scale micromechanics and passed to continuum model through a hierarchical framework. Numerical examples have shown the improved performance of the enhanced models compared to classical continuum models.

The key features and findings for the main chapters (Chapters 3 to 6) are summarized as following:

Chapter 3. Bridging continuum scales: multiscale random fields in geomechanics

- Scales of interest in this study are within the continuum regime and the failure phenomenon is the localized type. This study features a novel method for characterizing random fields for material properties, and a framework for coupling finite element method with random fields at multiple scales. The framework allows selective refinement of material properties at coarse scale in key areas of interest. The coarse scale constitutive response is provided by homogenized finer scale responses through a concurrent information passing scheme. The coarse scale and fine scale finite element computations communicate 'on the fly' throughout the simulation.
- It is found from this study that material property fluctuations, in general, will result in lower bearing capacities, unsymmetrical failure surfaces, and larger settlements. More importantly, in critical areas, multiscale framework allows higher levels of resolution in material properties to be taken into account, which results in lower bearing capacities and larger settlements. In contrast, if only single scale random fields are used, results are generally less conservative, i.e., predicting higher bearing capacities or smaller settlements.

Chapter 4: From continuum scales to granular scale: a semi-implicit integration algorithm for multiscale plasticity

- This chapter proposes a semi-implicit return mapping algorithm that will be used as the backbone for the multiscale framework linking continuum scales to granular scale in Chapters 5 and 6. This algorithm features freezing of plastic internal variables, followed by implicitly integrating the stresses and plastic mltiplier, and a posteriori update of plastic internal variables upon convergence.

- Through numerical examples, it is shown that the proposed semi-implicit algorithm demonstrates some crucial qualities such as good accuracy, stability, and quadratic convergence. More importantly, the semi-implicit algorithm is able to handle nonsmooth (C_0) and micromechanically-based evolution laws of critical variables, which could be particular useful in the multiscale framework.

Chapter 5: Multiscale localization modeling in granular media

- Scales of interest in this study are from continuum (specimen) scale to granular scale and the failure phenomenon is strain localization. A finite element enhancement technique, i.e., the assumed enhanced strain (AES) method, is used to accommodate discontinuous kinematic fields after localization. A key feature for this study is that evolutions of key material properties, e.g., friction and dilatancy, are extracted from granular scale computations or experimental data and are used to enhance the continuum model. Phenomenological softening modulus, typically required in standard AES formulations, is bypassed.
- It is shown that the proposed model is able to capture the localization behavior very well, matching results from discrete particle simulations and physical experiments. Mesh objectivity and numerical efficiency are also shown through numerical examples. It is shown that, two material parameters with clear physical meanings, i.e., friction and dilatancy, are the key information to extract from granular scale.

Chapter 6: Bridging solid-like and fluid-like behavior in dry dilative granular media

- Scales of interest in this chapter are from continuum scale to granular scale and the state transition as well as localized failure phenomena are analyzed. This study proposes an enhanced rate-dependent continuum model for dry dilative granular media aiming to bridge solid-like and fluid-like state. Material strength is decomposed into a dilatancy part and a rate-dependent residual strength. The state transition is accommodated by evolutions of dilatancy, which plays a key role in the solid-like state but vanishes towards the fluid-like state. Unlike the classical rate-independent plasticity models, the residual strength is proposed to be strain-rate-dependent, able to capture key features of fluid-like state of granular media.
- The proposed enhanced continuum constitutive description is implemented into a finite difference scheme to simulate granular flow along inclined surface. Results from continuum model are compared with numerical experiments by discrete particle simulations. It is shown that key features, such as solid-fluid transition, velocity profiles and free-surface velocity evolutions, are successfully captured by the proposed model. Moreover, the model is also applied to simulate a shear banding problem. The rate-effect on material strength inside and outside shear band has been taken into account. Comparisons of the proposed model with classical rate-independent model show that the enhanced material description provides a more accurate match with physical experiments.

7.2. Discussions and future work

There are several possible improvements to the studies presented in this dissertation. For the multiscale random fields study in Chapter 3, the first possible direction is to implement the proposed framework in three dimensions. To the knowledge of the author, even for single scale, there are very few studies on three dimensional random fields. The major challenge would be to generate random fields that would preserve desired spatial correlation across scales in three dimensions. The coupling of finite element with random fields would be similar to 2D, except that it is necessary to implement three dimensional elements, such as brick elements, able to split and match the resolutions of generated random fields. The other direction is to incorporate real experiment data when generating random fields. The experiment data can be utilized for two purposes: to determine an appropriate probability distribution and spatial correlation function for the material properties [**159**], or to incorporate measured data values into simulations of a specimen that includes some unmeasured locations. A few attempts in this direction has been carried out for single scale random fields, see, e.g., [**160**]

Regarding the semi-implicit return mapping algorithm in Chapter 4, one shortcoming of the method will be potential lack of accuracy because of the frozen plasticity. The accuracy can be improved using smaller time steps. Also, the formulation presented are for infinitesimal elastoplasticity only, but extension to finite deformation regime is straightforward.

Extensions of the localization modeling in granular media (Chapter 5) may include, within the multiscale framework, implementing three-dimensional finite elements with embedded discontinuities, implementing a tracing algorithm for propagating localization

band, and formulating the framework in finite deformation regime (see, e.g., [**161**, **111**, **103**, **121**] for work in these directions at single scale). Also, for making predictive simulation, a concurrent coupling between continuum scale and granular scale model is desired. This requires constant communications between continuum scale finite elements and granular scale computations, the work in presented in Chapter 4 and [**12**] show examples using concurrent information passing scheme. A major drawback for using concurrent framework, however, is the high computational cost. To this end, a parallel finite element program is desired. Finally, the size of a representative volume at the granular scale is not yet discussed in this dissertation and this requires further work.

The rate-depednent plasticity model in Chapter 6 has utilized the role of dilatancy to capture transition between solid-like state and fluid-like state. However, there are not yet sufficient numerical or physical experiments on how dilatancy evolves during the transition. Availability of physical experiment data is beyond the scope of the author's work, however, extensive numerical experiments using discrete particle simulations can be carried out to carefully examine the evolutions of dilatancy during the transition phase. As more experiments become available, better calibration of the proposed evolution laws can be achieved or new evolution laws can be proposed all together.

Bibliography

[1] J.E. Andrade, J.W. Baker, and K.C. Ellison. Random porosity fields and their influence on the stability of granular media. *International Journal for Numerical and Analytical Methods in Geomechanics*, 32:1147–1172, 2008.

[2] J.E. Andrade X. Tu and Q. Chen. Return mapping for nonsmooth and multiscale elastoplasticity. *Computer Methods in Applied Mechanics and Engineering*, 198:2286–2296, 2009.

[3] I. F. Collins. Plane strain characteristics theory for soils and granular materials with density dependent yield criteria. *Journal of the Mechanics and Physics of Solids*, 38:1–25, 1990.

[4] D. C. Drucker and W. Prager. Soil mechanics and plastic analysis or limit design. *Quarterly of Applied Mathematics*, 10:157–165, 1952.

[5] D. Harris. Plasticity models for soil, granular and jointed rock materials. *Journal of the Mechanics and Physics of Solids*, 40:273–290, 1992.

[6] P. A. Vermeer and R. de Borst. Non-associated plasticity for soils, concrete and rock. *Heron*, 29:1–62, 1984.

[7] Y. F. Dafalias and E. P. Popov. A model of nonlinearly hardening materials for complex loadings. *Acta Mechanica*, 21:173–192, 1975.

[8] M. R. Kingston and A. J. M. Spencer. General yield conditions in plane deformations of granular media. *Journal of the Mechanics and Physics of Solids*, 18:233–243, 1970.

[9] F. L. DiMaggio and I. S. Sandler. Material model for granular soils. *Journal of the Engineering Mechanics Division-ASCE*, 97:935–950, 1971.

[10] J. W. Rudnicki and J. R. Rice. Conditions for localization of deformation in pressure-sensitive dilatant materials. *Journal of the Mechanics and Physics of Solids*, 23:371–394, 1975.

[11] R. I. Borja. Bifurcation of elastoplastic solids to shear band mode at finite strains. *Computer Methods in Applied Mechanics and Engineering*, 191:5287–5314, 2002.

[12] J.E. Andrade and X. Tu. Multiscale framework for behavior prediction in granular media. *Mechanics of Materials*, 41(6):652–669, 2009.

[13] J. C. Simo and T. J. R. Hughes. *Computational Inelasticity*. Prentice-Hall, New York, 1998.

[14] P.A. Cundall and O.D.L. Strack. A discrete numerical model for granular assemblies. *Géotechnique*, 29:47–65, 1979.

[15] M. A. Mooney, R. J. Finno, and M. G. Viggiani. A unique critical state for sand? *Journal of Geotechnical and Geoenvironmental Engineering*, 124:1100–1108, 1998.

[16] M. Xu. *Multiscale Methods: Bridging the Scales in Science and Engineering*, chapter Concurrent Coupling of Atomistic and Continuum Models. Oxford University Press, 2009.

[17] J.C. Simo, J. Oliver, and F.Armero. An analysis of strong discontinuities induced by strain-softening in rate-independent inelastic solids. *Computational Mechanics*, 12:277–296, 1993.

[18] J. Oliver. Modelling strong discontinuities in solid mechanics via strain softening constitutive equations. part 1: Fundamentals, part 2: Numerical simulations. *International Journal for Numerical Methods in Engineering*, 39:3575–3623, 1996.

[19] T. J. R. Hughes. *The Finite Element Method*. Prentice-Hall, Englewood Cliffs, NJ, 1987.

[20] J.C. Simo and J. Oliver. A new approach to the analysis and simulation of strain softening in solids. In Z.P. Bazant, Z. Bittnar, M. Jirasek, and J. Mazars, editors, *Fracture and Damage in Quasibrittle Structures*, pages 25–39. E & FN Spon, London, 1994.

[21] J.C. Simo and M.S. Rifai. A class of mixed assumed strain methods and the method of incompatible modes. *International Journal for Numerical Methods in Engineering*, 29:1595–1638, 1990.

[22] Ronaldo I. Borja. A finite element model for strain localization analysis of strongly discontinuous fields based on standard galerkin approximation. *Computer Methods in Applied Mechanics and Engineering*, 190:1529–1549, 2000.

[23] Ronaldo I. Borja. Assumed enhanced strain and the extended finite element methods: A unification of concepts. *Computer Methods in Applied Mechanics and Engineering*, 197:2789–2803, 2008.

[24] J. Mosler. A novel algorithmic framework for the numerical implementation of locally embedded strong discontinuities. *Computer Methods in Applied Mechanics and Engineering*, 194:4731–4757, 2005.

[25] J. Mosler. Modeling strong discontinuities at finite strains – a novel numerical implementation. *Computer Methods in Applied Mechanics and Engineering*, 195:4396–4419, 2006.

[26] D.V. Griffiths and G.A. Fenton. Bearing capacity of spatially random soil: the undrained clay prandtl problem revisited. *Géotechnique*, 51(4):351–359, 2001.

[27] D.V. Griffiths, G.A. Fenton, and N. Manoharan. Bearing capacity of rough rigid strip footing on cohesive soil: probabilistic study. *Journal of Geotechnical and Geoenvironmental Engineering*, 128(9):743–755, 2002.

[28] R. Popescu, G. Deodatis, and A. Nobahar. Effects of random heterogeneity of soil properties on bearing capacity. *Probabilistic Engineering Mechanics*, 20:324–341, 2005.

[29] L. Shen and X.F. Xu. Multiscale stochastic finite element modeling of random elastic heterogeneous materials. *Computational Mechanics*, 45:607–621, 2010.

[30] X. Chen X.F. Xu and L. Shen. A green-function-based multiscale method for uncertainty quantification of finite body random heterogeneous materials. *Computers and Structures*, 87:1416–1426, 2009.

[31] X.F. Xu. A multiscale stochastic finite element method on elliptic problems involving uncertainties. *Computer Methods in Applied Mechanics and Engineering*, 196:2723–2736, 2007.

[32] F. Feyel and J.L. Chaboche. FE^2 multiscale approach for modelling of the elastoviscoplastic behaviour of long fibre SiC/Ti composite materials. *Computer Methods in Applied Mechanics and Engineering*, 183:309–330, 2000.

[33] F. Feyel. A multilevel finite element method (FE^2) to describe the response of highly non-linear structures using generalized continua. *Computer Methods in Applied Mechanics and Engineering*, 192:3233–3244, 2003.

[34] A. Ibrahimbegović and D. Markovič. Strong coupling methods in multi-phase and multi-scale modeling of inelastic behavior of heterogeneous structures. *Computer Methods in Applied Mechanics and Engineering*, 192:3089–3107, 2003.

[35] D. Markovič and A. Ibrahimbegović. On micro-macro interface conditions for micro scale based fem for inelastic behavior of heterogeneous materials. *Computer Methods in Applied Mechanics and Engineering*, 193:5503–5523, 2004.

[36] D. Markovič, R. Niekamp, A. Ibrahimbegović, H. G. Matthies, and R. L. Taylor. Multi-scale modeling of heterogeneous structures with inelastic constitutive behaviour part i - physical and mathematical aspects. *Engineering Computations*, 22:664–683, 2005.

[37] P. Ladevèze, O. Loiseau, and D. Dureisseix. A micro-macro and parallel computational strategy for highly heterogeneous structures. *International Journal for Numerical Methods in Engineering*, 52:121–138, 2001.

[38] S. Nemat-Nasser and M. Hori. *Micromechanics: overall properties of heterogeneous materials*. Elsevier, Amsterdam, The Netherlands, 1999.

[39] I.M. Gitman, H. Askes, and L.J. Sluys. Coupled-volume multi-scale modelling of quasi-brittle material. *European Journal of Mechanics A/Solids*, 27:302–327, 2008.

[40] P. Goovaerts. *Geostatistics for natural resources evaluation*. Oxford University Press, New York, 1997.

[41] P. Liu and A. Der Kiureghian. Multivariate distribution models with prescribed marginals and covariances. *Probabilistic Engineering Mechanics*, 1(2):105–112, 1986.

[42] E. Vanmarcke. *Random Fields: Analysis and Synthesis*. MIT Press, Cambridge, MA, 1983.

[43] E A de Souza Neto and R A Feijóo. Variational foundations of multi-scale constitutive models of solids: Small and large strain kinematical formulation. Technical report, National Laboratory for Scientific Computing (LNCC), Brazil, 2006.

[44] T. I. Zohdi and P. Wriggers. *Introduction to Computational Micromechanics*. Springer Press, New York, 2005.

[45] G.A. Fenton and D.V. Griffiths. *Probabilistic methods in geotechnical engineering*, chapter The random finite element method (RFEM) in bearing capacity analysis. SpringerWienNewYork, 2007.

[46] S.C. Baxter and L.L. Graham. Characterization of random composites using moving-window technique. *Journal of Engineering Mechanics*, 126:389–397, 2000.

[47] R. Hill. *The Mathematical Theory of Plasticity*. Oxford University Press, New York, NY, 1950.

[48] W. T. Koiter. General theorems for elastic-plastic solids. In I. N. Sneddon and R. Hill, editors, *Progress in Solid Mechanics*, pages 165–221, Amsterdam, 1960. North-Holland.

[49] P. V. Lade. Elastoplastic stress-strain theory for cohesionless soil with curved yield surfaces. *International Journal of Solids and Structures*, 13:1019–1035, 1977.

[50] T. Schanz, P. A. Vermeer, and P. G. Boninier. The hardening soil model: Formulation and verification. In R. B. J. Brinkgreve, editor, *Beyond 2000 in computational geotechnics -10 years of Plaxis international*, pages 281–296, Rotterdam, 1999. Balkema.

[51] P. V. Lade and M. K. Kim. Single hardening constitutive model for frictional materials II. Yield criterion and plastic work contours. *Computers and Geotechnics*, 6:13–29, 1988.

[52] P. V. Lade and K. P. Jakobsen. Incrementalization of a single hardening constitutive model for frictional materials. *International Journal for Numerical and Analytical Methods in Geomechanics*, 26:647–659, 2002.

[53] I. M. Smith and D. V. Griffith. *Programming the Finite Element Method*. John Wiley & Sons Ltd., Chichester, UK, 1982.

[54] H. Matsuoka and T. Nakai. A new failure criterion for soils in three-dimensional stresses. In *Conference on Deformation and Failure of Granular Materials*, pages 253–263. IUTAM, 1982.

[55] A. J. Whittle and M. J. Kavvadas. Formulation of MIT-E3 constitutive model for overconsolidated clays. *Journal of Geotechnical Engineering - ASCE*, 120:173–198, 1994.

[56] R. I. Borja and A. Aydin. Computational modeling of deformation bands in granular media. I. Geological and mathematical framework. *Computer Methods in Applied Mechanics and Engineering*, 193:2667–2698, 2004.

[57] J. E. Andrade and R. I. Borja. Capturing strain localization in dense sands with random density. *International Journal for Numerical Methods in Engineering*, 67:1531–1564, 2006.

[58] C. D. Foster, R. A. Regueiro, A. F. Fossum, and R. I. Borja. Implicit numerical integration of a three-invariant, isotropic/kinematic hardening cap plasticity model for geomaterials. *Computer Methods in Applied Mechanics and Engineering*, 194(50-52):5109–5138, 2005.

[59] E. Tadmor, M. Ortiz, and R. Phillips. Quasicontinuum analysis of defects in solids. *Philosophical Magazine A*, 73:1529–1563, 1996.

[60] W. K. Liu, E. G. Karpov, and H. S. Park. *Nano Mechanics and Materials*. John Wiley & Sons Ltd., Chichester, West Sussex, UK, 2006.

[61] T. Belytschko, S. Loehnert, and J. H. Song. Multiscale aggregating discontinuities: a method for circumventing loss of material stability. *International Journal for Numerical Methods in Engineering*, In press, 2008.

[62] R. I. Borja and J. R. Wren. Micromechanics of granular media, Part I: Generation of overall constitutive equation for assemblies of circular disks. *Computer Methods in Applied Mechanics and Engineering*, 127:13–36, 1995.

[63] C. Wellmann, C. Lillie, and P. Wriggers. Homogenization of granular material modeled by a three-dimensional discrete element method. *Computers and Geotechnics*, 35:394–405, 2008.

[64] X. Tu and J. E. Andrade. Criteria for static equilibrium in particulate mechanics computations. *International Journal for Numerical Methods in Engineering*, 2008. In press.

[65] P. W. Christensen. A nonsmooth newton method for elastoplastic problems. *Computer Methods in Applied Mechanics and Engineering*, 191:1189–1219, 2002.

[66] B. Moran, M. Ortiz, and C. F. Shih. Formulation of implicit finite element methods for multiplicative finite deformation plasticity. *International Journal for Numerical Methods in Engineering*, 29:483–514, 1990.

[67] T. Belytschko, W. K. Liu, and B. Moran. *Nonlinear Finite Elements for Continua and Structures*. John Wiley & Sons Ltd., West Sussex, UK, 2000.

[68] S. W. Sloan, A. J. Abbo, and D. Sheng. Refined explicit integration of elastoplastic models with automatic error control. *Engineering Computations*, 18:121–154, 2001.

[69] J. Zhao, D. Sheng, M. Rouainia, and S. W. Sloan. Explicit stress integration of complex soil models. *International Journal for Numerical and Analytical Methods in Geomechanics*, 29:1209–1229, 2005.

[70] C. Tamagnini, R. Castellanza, and R. Nova. A generalized backward euler algorithm for the numerical integration of an isotropic hardening elastoplastic model for mechanical and chemical degradation of bonded geomaterials. *International Journal for Numerical and Analytical Methods in Geomechanics*, 26:963–1004, 2002.

[71] R. I. Borja, K. M. Sama, and P. F. Sanz. On the numerical integration of three-invariant elastoplastic constitutive models. *Computer Methods in Applied Mechanics and Engineering*, 192:1227–1258, 2003.

[72] C. Miehe. Numerical computation of algorithmic (consistent) tangent moduli in large-strain computational inelasticity. *Computer Methods in Applied Mechanics and Engineering*, 134:223–240, 1996.

[73] M. Ortiz and J. B. Martin. Symmetry-preserving return mapping algorithms and incrementally extremal paths - a unification of concepts. *International Journal for Numerical Methods in Engineering*, 8:1839–1853, 1989.

[74] R.I. Borja and J.E. Andrade. Critical state plasticity, part vi: Meso-scale finite element simulation of strain localization in discrete granular materials. *Computer Methods in Applied Mechanics and Engineering*, 195:5115–5140, 2006.

[75] S. W. Sloan. Substepping schemes for the numerical integration of elasto-plastic stress-strain relations. *International Journal for Numerical Methods in Engineering*, 24:893–911, 1987.

[76] K. P. Jakobsen and P. V. Lade. Implementation algorithm for a single hardening constitutive model for frictional materials. *International Journal for Numerical and Analytical Methods in Geomechanics*, 26:661–681, 2002.

[77] A. Pérez-Foguet, A. Rodríguez-Ferran, and A. Huerta. Consistent tangent matrices for substepping schemes. *Computer Methods in Applied Mechanics and Engineering*, 190:4627–4647, 2001.

[78] A. Pérez-Foguet, A. Rodríguez-Ferran, and A. Huerta. Numerical differentiation for local and global tangent operators in computational plasticity. *Computer Methods in Applied Mechanics and Engineering*, 189:277–296, 2000.

[79] O. Reynolds. On the dilatancy of media composed of rigid particles in contact. *Philosophical Magazine and Journal of Science*, 20:468–481, 1885.

[80] P. W. Rowe. The stress-dilatancy relation for static equilibrium of an assembly of particles in contact. *Proceedings of the Royal Society of London, Series A*, 269:500–527, 1962.

[81] D. Muir-Wood. *Soil Behaviour and Critical State Soil Mechanics*. Cambridge University Press, Cambridge, UK, 1990.

[82] P. A. Cundall. A discontinuous future for numerical modelling in geomechanics? *Geotechnical Engineering, ICE*, 149:41–47, 2001.

[83] Z. Hashin. Analysis of composite materials - a survey. *Journal of Applied Mechanics*, 50:481–505, 1983.

[84] J. Christoffersen, M. M. Mehrabadi, and S. Nemat-Nasser. A micromechanical description of granular material behavior. *Journal of Applied Mechanics*, 48:339–344, 1981.

[85] M. Satake. A discrete-mechanical approach to granular materials. *International Journal of Engineering Science*, 30:1525–1533, 1992.

[86] K. Bagi. Stress and strain in granular assemblies. *Mechanics of Materials*, 22:165–177, 1996.

[87] M. R. Kuhn. Structured deformation in granular materials. *Mechanics of Materials*, 31:407–429, 1999.

[88] J. C. Simo. Algorithms for static and dynamic multiplicative plasticity that preserve the classical return mapping schemes of the infinitesimal theory. *Computer Methods in Applied Mechanics and Engineering*, 99:61–112, 1992.

[89] A. Tordesillas and J. Shi. Micromechanical analysis of failure propagation in frictional granular materials. *International Journal for Numerical and Analytical Methods in Geomechanics*, 33:1737–1768, 2009.

[90] R. Wan, P. Guo, and M. Al-Mamun. Behavior of granular materials in relation to their fabric dependencies. *Soils and Foundations*, 45:77–86, 2005.

[91] F. Darve, L. Sibille, A. Daouadji, and F. Nicot. Bifurcations in granular media: macro- and micro-mechanics approaches. *C.R. Mecanique*, 335:496–515, 2007.

[92] F. Nicot, L. Sibille, and F. Darve. Bifurcation in granular materials: An attempt for a unified framework. *International Journal of Solids and Structures*, 46:3938–3947, 2009.

[93] K. Runesson, N. S. Ottosen, and D. Peric. Discontinuous bifurcations of elastic-plastic solutions at plane stress and plane strain. *International Journal of Plasticity*, 7:99–121, 1991.

[94] D. Bigoni and T. Hueckel. Uniqueness and localization, i: associative and non-associative elasto-plasticity. *International Journal of Solids and Structures*, 28:197–213, 1991.

[95] J.E. Andrade and R.I. Borja. Modeling deformation banding in dense and loose fluid-saturated sands. *Finite Element in Analysis and Design*, 43:361–383, 2007.

[96] Z. P. Bažant, T. Belytschko, and T. P. Chang. Continuum theory for strain-softening. *Journal of Engineering Mechanics, ASCE*, 110:1666–1692, 1984.

[97] T. Belytschko, J. Fish, and B. E. Engelmann. A finite element with embedded localization zones. *International Journal for Numerical Methods in Engineering*, 70:59–89, 1988.

[98] E. Samaniego and T. Belytschko. Continuum-discontinuum modelling of shear bands. *International Journal for Numerical Methods in Engineering*, 62:1857–1872, 2005.

[99] T. Rabczuk and E. Samaniego. Discontinuous modelling of shear bands using adaptive meshfree methods. *Computer Methods in Applied Mechanics and Engineering*, 197:641–658, 2008.

[100] J. Oliver, A.E. Huespe, E. Samaniego, and E.W.V. Chaves. Continuum approach to the numerical simulation of material failure in concrete. *International Journal for Numerical and Analytical Methods in Geomechanics*, 28:609–632, 2004.

[101] N. Moës, J. Bolbow, and T. Belytschko. A finite element method for crack growth without remeshing. *International Journal for Numerical Methods in Engineering*, 46:131–150, 1999.

[102] J.M. Melenk and I. Babuška. The partition of unity finite element method: Basic theory and applications. *Computer Methods in Applied Mechanics and Engineering*, 139:289–314, 1996.

[103] F. Armero and K. Garikipati. An analysis of strong discontinuities in multiplicative finite strain plasticity and their relation with the numerical simulation of strain localization in solids. *International Journal of Solids and Structures*, 33:2863–2885, 1996.

[104] C. Callari and F. Armero. Finite element methods for the analysis of strong discontinuities in coupled poro-plastic media. *Computer Methods in Applied Mechanics and Engineering*, 191:4371–4400, 2002.

[105] M. Jirásek. Comparative study on finite elements with embedded discontinuities. *Computer Methods in Applied Mechanics and Engineering*, 188:307–330, 2000.

[106] J. Oliver, A.E. Huespe, and E. Samaniego. A study on finite elements for capturing strong discontinuities. *International Journal for Numerical Methods in Engineering*, 56:2134–2161, 2003.

[107] J. Oliver. A comparative study on finite elements for capturing strong discontinuities e-fem vs x-fem. *Computer Methods in Applied Mechanics and Engineering*, 195:4732–4752, 2006.

[108] Richard A. Regueiro and Ronaldo I. Borja. A finite element model of localized deformation in frictional materials taking a strong discontinuity approach. *Finite Element in Analysis and Design*, 33:283–315, 1999.

[109] Richard A. Regueiro and Ronaldo I. Borja. Plane strain finite element analysis of pressure sensitive plasticity with strong discontinuity. *International Journal of Solids and Structures*, 38:3647–3672, 2001.

[110] Ronaldo I. Borja and Richard A. Regueiro. Strain localization in frictional materials exhibiting displacement jumps. *Computer Methods in Applied Mechanics and Engineering*, 190:2555–2580, 2001.

[111] J. Mosler and G. Meschke. 3d modelling of strong discontinuities in elastoplastic solids: fixed and rotating localization formulations. *International Journal for Numerical Methods in Engineering*, 57:1553–1576, 2003.

[112] C.D. Foster, R.I. Borja, and R.A. Regueiro. Embedded strong discontinuity finite elements for fractured geomaterials with variable friction. *International Journal for Numerical Methods in Engineering*, 72:549–581, 2007.

[113] Q. Chen, A.E. Seifried, J.E. Andrade, and J.W. Baker. Characterization of random fields and their impact on the mechanics of geosystems at multiple scales. *International Journal for Numerical and Analytical Methods in Geomechanics*, doi:10.1002/nag.999, 2010.

[114] J.P. Bardet and J. Proubet. A numerical investigation of the structure of persistent shear bands in granular media. *Géotechnique*, 41:599–613, 1991.

[115] J.P. Bardet and J. Proubet. Shear-band analysis in idealized granular material. *Journal of Engineering Mechanics*, 118:397–415, 1992.

[116] K. Iwashita and M. Oda. Rolling resistance at contacts in simulation of shear band development by dem. *Journal of Engineering Mechanics*, 124:285–292, 1998.

[117] K. Iwashita and M. Oda. Micro-deformation mechanism of shear banding process based on modified distinct element method. *Powder Technology*, 109:192–205, 2000.

[118] N. Hu and J. F. Molinari. Shear bands in dense metallic granular materials. *Journal of the Mechanics and Physics of Solids*, 52:499–531, 2004.

[119] J.E. Andrade, C.F. Avila, S.A. Hall, N. Lenoir, and G. Viggiani. Multiscale modeling and characterization of granular matter: from grain kinematics to continuum mechanics. *Journal of the Mechanics and Physics of Solids*, 59:237–250, 2010.

[120] C. Linder and F. Armero. Finite elements with embedded strong discontinuities for the modeling of failure in solids. *International Journal for Numerical Methods in Engineering*, 72:1391–1433, 2007.

[121] F. Armero and C. Linder. New finite elements with embedded strong discontinuities in the finite deformation range. *Computer Methods in Applied Mechanics and Engineering*, 197:3138–3170, 2008.

[122] G.A. D'Addetta, E. Ramm, S. Diebels, and W. Ehlers. A particle center based homogenization strategy for granular assemblies. *Engineering Computations*, 21:360–383, 2004.

[123] S.A. Hall, M. Bornert, J. Desrues, Y. Pannier, N. Lenoir, G. Viggiani, and P. Bésuelle. Discrete and continuum analysis of localized deformation in sand using x-ray micro ct and volumetric digital image correlation. *Géotechnique*, 60:315–322, 2010.

[124] N. Lenoir, M. Bornert, J. Desrues, and G. Viggiani. 3d digital image correlation applied to x-ray microtomography images from triaxial compression tests on argillaceous rock. *Strain*, 43:193–205, 2007.

[125] I. Vardoulakis. Shear band inclination and shear modulus of sand in biaxial tests. *International Journal for Numerical and Analytical Methods in Geomechanics*, 4:103–119, 1980.

[126] H.M. Jaeger, S.R. Nagel, and R.P. Behringer. Granular solids, liquids, and gases. *Reviews of Modern Physics*, 68:1259–1273, 1996.

[127] M. T. Manzari and Y. F. Dafalias. A critical state two-surface plasticity model for sands. *Géotechnique*, 43:255–272, 1997.

[128] J. M. Pestana and A. J. Whittle. Formulation of a unified constitutive model for clays and sands. *International Journal for Numerical and Analytical Methods in Geomechanics*, 23:1215–1243, 1999.

[129] A. Schofield and P. Wroth. *Critical State Soil Mechanics*. McGraw-Hill, New York, 1968.

[130] J. E. Andrade and K. C. Ellison. Evaluation of a predictive constitutive model for sands. *Journal of Geotechnical and Geoenvironmental Engineering*, 134:1825–1828, 2008.

[131] C. S. Desai and H. J. Siriwardane. *Constitutive Laws for Engineering Materials*. Prentice-Hall, Inc., 1984.

[132] M.A. Stroud. *The behavior of sand at low stress levels in the simple shear apparatus*. PhD thesis, Cambridge University, Cambridge, UK, 1971.

[133] D. W. Taylor. *Fundamentals of Soil Mechanics*. John Wiley & Sons Ltd, New York, 1948.

[134] L.E. Silbert, D. Ertas, G.S. Grest, T.C. Halsey, D. Levine, and S.J. Plimpton. Granular flow down an inclined plane: Bagnold scaling and rheology. *Physical Review E*, 64:051302, 2001.

[135] L.E. Silbert, J.W. Landry, and G.S. Grest. Granular flow down a rough inclined plane: Transition between thin and thick piles. *Physics of Fluids*, 15:1, 2003.

[136] G. Berton, R. Delannay, P. Richard, N. Taberlet, and A. Valance. Two-dimensional inclined chute flows: Transverse motion and segregation. *Physical Review E*, 68:051303, 2003.

[137] P. Jop, Y. Forterre, and O. Pouliquen. Initiation of granular surface flows in a narrow channel. *Physics of Fluids*, 19:088102, 2007.

[138] J. Rajchenbach. Flow in powders: From discrete avalanches to continuous regime. *Physical Review Letters*, 65:2221–2224, 1990.

[139] S.C. du Pont, R. Fischer, P. Gondret, B. Perrin, and M. Rabaud. Instantaneous velocity profiles during granular avalanches. *Physical Review Letters*, 94:048003, 2005.

[140] P.A. Thompson and G.S. Grest. Granular flow: friction and dilatancy transition. *Physical Review Letters*, 67:1751–1754, 1991.

[141] Y. Zhang and C.S. Campbell. The interface between fluid-like and solid-like behavior in two-dimensional granular flows. *Journal of Fluid Mechanics*, 237:541–568, 1992.

[142] GDR MiDi. On dense granular flows. *The European Physical Journal E*, 14:341–365, 2004.

[143] R. Delannay, M. Louge, P. Richard, N. Taberlet, and A. Valance. Towards a theoretical picture of dense granular flows down inclines. *Nature Materials*, 6:99–108, 2007.

[144] P. Jop, Y. Forterre, and O. Pouliquen. A constitutive law for dense granular flows. *Nature*, 441:727–730, 2006.

[145] O. Pouliquen, C. Cassar, P. Jop, Y. Forterre, and M. Nicolas. Flow of dense granular material: towards simple constitutive laws. *Journal of Statistical Mechanics: Theory and Experiment*, page P07020, 2006.

[146] P. Jop, Y. Forterre, and O. Pouliquen. Crucial role of side walls for granular surface flows: consequences for the rheology. *Journal of Fluid Mechanics*, 541:167–192, 2005.

[147] Y. C. Fung. *A First Course in Continuum Mechanics*. Prentice-Hall, Inc., Englewood Cliffs, NJ, 1977.

[148] Y. Forterre and O. Pouliquen. Flows of dense granular media. *The Annual Review of Fluid Mechanics*, 40:1–24, 2008.

[149] F. da Cruz, S. Emam, M. Prochnow, J-N. Roux, and F. Chevoir. Pheophysics of dense granular materials: discrete simulation of plane shear flows. *Physical Review E*, 72:021309, 2005.

[150] G. Lois, A. Lemaitre, and J.M. Carlson. Numerical tests of constitutive laws for dense granular flows. *Physical Review E*, 72:051303, 2005.

[151] P. Mills, D. Loggia, and M. Tixier. Model for a stationary dense granular flow along an inclined wall. *Europhysics letter*, 45:733, 1999.

[152] S.B. Savage and K. Hutter. The motion of a finite mass of granular material down a rough incline. *Journal of Fluid Mechanics*, 199:177–215, 1989.

[153] R. Greve, T. Koch, and K. Hutter. Unconfined flow of granular avalanches along a partly curved surface: experiments and theoretical predictions. *Proceedings: Mathematical and Physical Sciences*, 445:415–435, 1994.

[154] M. Wieland, J.M.N.T. Gray, and K. Hutter. Channelized free-surface flow of cohesionless granular avalanches in a chute with shallow lateral curvature. *Journal of Fluid Mechanics*, 392:73–100, 1999.

[155] A.V. Orpe and D.V. Khakhar. Solid-fluid transition in a granular shear flow. *Physical Review Letters*, 93:068001, 2004.

[156] P. Mills, M. Tixier, and D. Loggia. Influence of roughness and dilatancy for dense granular flow along an inclined wall. *The European Physical Journal E*, 1:5–8, 2000.

[157] C. Goujon, N. Thomas, and B. Dalloz-Dubrujeaud. Monodisperse dry granular flows on inclined planes: Role of roughness. *The European Physical Journal E*, 11:147–157, 2003.

[158] R. Courant, K. Friedrichs, and H. Lewy. On the partial difference equations of mathematical physics. *IBM Journal of Research and Development*, 11:215–234, 1967.

[159] J. A. Rice. *Mathematical statistics and data analysis*. Duxbury Press, Belmont, CA, 1995.

[160] J. W. Baker and M. Faber. Liquefaction risk assessment using geostatistics to account for soil spatial variability. *Journal of Geotechnical and Geoenvironmental Engineering*, 134:14–23, 2007.

[161] Richard A. Regueiro. Embedded discontinuity finite element modeling of three-dimensional strong discontinuities in rocks. In *Golden Rocks 2006, Golden, CO.* ARMA/USRMS 06-1069, 2006.

Vita

QIUSHI CHEN

EDUCATION

Ph.D., Theoretical and Applied Mechanics, Northwestern University, Evanston, IL, USA. June 2011.

M.S., Theoretical and Applied Mechanics, Northwestern University, Evanston, IL, USA. December 2009.

B.S., Civil Engineering, Shanghai Jiaotong University, Shanghai, China. June 2006.

PUBLICATIONS

1 Q. Chen, A.E. Seifried, J.E. Andrade and J.W. Baker. Characterization of random fields and their impact on the mechanics of geosystems at multiple scales. *International Journal for Numerical and Analytical Methods in Geomechanics*, doi:10.1002/nag.999, 2010.

2 Q. Chen, J.E. Andrade and E. Samaniego. AES for multscale localization modeling in granular media. *Computer Methods in Applied Mechanics and Engineering*, doi:10.1016/j.cma.2011.04.022, 2011.

3 X. Tu, J.E. Andrade and Q. Chen. Return mapping for nonsmooth and multiscale plasticity. *Computer Methods in Applied Mechanics and Engineering*, 198:2286–2296, 2009.

4 J.E. Andrade, Q. Chen, P.B.H. Le, C.F. Avila and M.T. Evans. On the rheology of dilative granular media: bridging solid and fluid-like behavior. *Journal of the Mechanics and Physics of Solids*, in review, 2011.

5 X. Tu, Q. Chen and J.E. Andrade. A new strategy for implementing plasticity models for cohesive-frictional materials. In *Proceedings for the Inaugural International Conference of the Engineering Mechanics Institute*, Minnesota, MN, 2008.

6 Q. Chen and J.E. Andrade. Modeling post-localization behavior in granular materials using a multiscale strong discontinuity approach. In *Proceedings for the 16th US National Congress of Theoretical and Applied Mechanics*, State College, Pennsylvania, 2010.

7 J.W. Baker, A.E. Seifried, J.E. Andrade and Q. Chen. Characterization of random fields at multiple scales: an efficient conditional simulation procedure and applications in geomechanics. In *Proceedings for the 11th International Conference on Applications of Statistics and Probability in Civil Engineering*, Zurich, Switzerland, 2011.

8 J.E. Andrade, P.B.H. Le, Q. Chen and C.F. Avila. A rate-dependent plasticity model bridging solid- and fluid-like behaviors for dilative granular media. In *Proceedings for the 11th US National Congress on Computational Mechanics*, Minnesota, MN, 2011.